



universität
wien

DISSERTATION

Titel der Dissertation

„Molecular beam methods for quantum optics
experiments: sources, detection schemes
and coherent manipulation “

Verfasser

Dott. Mag. Michele Sclafani

angestrebter akademischer Grad

Doktor der Naturwissenschaften (Dr. rer. nat.)

Wien, Juli 2013

Studienkennzahl lt. Studienblatt: A 791 411

Dissertationsgebiet lt. Studienblatt: Physik

Betreuerin / Betreuer: Univ.-Prof. Dr. Markus Arndt

Contents

List of symbols	7
Abstract	9
Zusammenfassung	11
Introduction	13
The matter-wave mystery	13
Molecular interferometry	14
Contents	17
 I From molecular beam production to superconducting nano-wire detectors	 21
1 Molecular beam production	23
1.1 Introduction	23
1.2 Theoretical outlook	25
1.2.1 Fundamentals of kinetic gas theory	25
1.2.1.1 Velocity distribution	26
1.2.1.2 Mean free path	26
1.2.1.3 Rotational and vibrational states distribution	27
1.2.1.4 Effusive source - Knudsen cell	28
1.2.2 Fundamental principles of gas dynamics	29
1.2.2.1 One-dimensional flow	29
1.3 Experimental outlook	33
1.3.1 Generation of pulsed beams	33
1.3.1.1 A brief overview	33

1.3.1.2	Experimental realization of a laser desorption source	35
1.3.1.3	Principles of photo-ionization	36
1.3.1.4	Experimental realization of TOF-MS	39
1.3.2	Effusive beams generation	41
1.3.2.1	Experimental realization of a hyperthermal-beam	41
1.4	Conclusions	45

II Superconducting single particle detector 47

2	Superconducting nano-wire detector 49
2.1	Introduction 49
2.2	Historical review 50
2.2.1	Cryogenic detectors to mass spectrometry 50
2.2.2	SSPDs as particles detectors 53
2.3	Superconducting nano-wires 55
2.3.1	Theory 55
2.3.2	An experimental approach 58
2.4	SSPD figure of merit 61
2.5	SSPDs realization 62
2.6	Neutral particle detection 63
2.6.1	Experimental setup 63
2.6.2	Device readout 64
2.6.3	First demonstration of neutral particle detection . . . 65
2.6.4	Comparison with TOF-MS 67
2.6.5	Open questions 69
2.7	Detection of single ions at low kinetic energy 72
2.7.1	Experimental setup 72
2.7.2	Single particle sensitivity 74
2.7.3	Energy sensitivity 75
2.7.4	Hot-spot radius 76
2.7.5	Role of the surface adsorbates 79
2.7.6	Future perspectives 80

III Molecular single-grating diffraction in the far-field 83

3 Matter-wave fields 85

3.1	Introduction	85
3.2	Theory	86
3.3	Kirchhoff's diffraction theory	87
3.3.1	Interference from a diffraction grating	89
3.4	Some considerations about coherence	91

4 Far field interferometry 95

4.1	Introduction	95
4.2	Molecular source	97
4.2.1	Laser evaporation	97
4.2.2	Coherence preparation	98
4.3	Interferometer stage	100
4.3.1	Diffraction gratings	100
4.3.2	Velocity selection	102
4.4	Detection stage	103
4.4.1	Single molecule fluorescence microscopy	104
4.4.1.1	Jablonsky diagram	104
4.4.1.2	Absorption related parameters	105
4.4.1.3	Emission related parameters	105
4.4.1.4	Single molecule sensitivity	107
4.4.2	Phthalocyanine	108
4.4.3	Single molecule epi-fluorescence microscopy	108
4.5	Evaluation of van der Waals interactions	113
4.5.1	Interaction with a material grating	113
4.5.2	Experimental specifications	114
4.5.3	Data analysis	115
4.6	Coherent propagation through a biological sample	119
4.6.1	Marine <i>diatoms</i>	120
4.6.2	Sample preparation	122
4.6.3	Results	122

Conclusions 127

Superconducting single particle detector	127
Far-field matter-wave interferometry	128

Acknowledgements	129
Bibliography	131
Curriculum Vitae	145

List of symbols

Λ	Mean free path - [cm]
λ_{dB}	de Broglie wavelength - [pm]
σ	Scattering cross section - [nm ²]
ϑ	Diffraction angle - [μ rad]
c	Speed of light - [$c \simeq 3 \times 10^8$ m/s]
d	Periodicity of the diffraction grating - [nm]
$h(\hbar)$	Planck's constant - [$h=6.626 \times 10^{-34}$ J s; $\hbar=h/2\pi$]
k_B	Boltzmann's constant - [$k_B = 1.38 \times 10^{-23}$ J K ⁻¹]
M	Molecular mass expressed in atomic mass units - [u]
m	Rest mass of a particle - [Kg]
N	Number of particles
N_A	Avogadro constant- [$N_A \simeq 6.022 \times 10^{23}$ mol ⁻¹]
P	Pressure - [mbar - 1 mbar = 100 Pa = 0.75 Torr = 9.87×10^{-4} atm]
R	Universal gas constant per mole - [$R \simeq 8.314$ J K ⁻¹ mol ⁻¹]
T	Temperature - [K]
u	Unified atomic mass unit - [$1u \simeq 1.66 \times 10^{-27}$ Kg]
V	Volume - [m ³]
v	Velocity of a mass particle - [m/s]

Abstract

Molecular matter-wave interferometry has become a broad research field, spanning experiments from the foundations of quantum mechanics to advanced quantum-assisted metrology. The experimental demonstration of the particle-wave dualism with particles with increasing mass and complexity requires the exploration of novel beam methods for the production of neutral slow molecules as well as the investigation of new detection schemes with single particle sensitivity.

The first part of my PhD focused on the characterization of a novel superconducting nano-wire detector which was originally developed for the detection of single photons and therefore often referred to as a Superconducting Single Photon Detector (SSPD). I provide a proof-of-principle for the detection of neutral massive particles together with a comprehensive characterization of the SSPD sensitivity for ions. The detection efficiency of SSPDs is studied with a beam of low energetic He^+ (0.2-1 keV) and their potential applications to mass spectroscopy are discussed.

The second part of my thesis is dedicated to the investigation of the role of van der Waals potentials in single-grating diffraction in the far-field with molecular matter-waves. The interaction between polarizable molecules (PcH_2 - 514 u) and SiN surfaces is explored by evaluating the interference patterns collected behind different diffraction gratings (100 nm periodicity, thickness 10 - 90 nm). The validity of the existing theoretical models is discussed. Finally, I illustrate the coherent propagation of PcH_2 through a biologically grown nano-structure, namely the SiO_2 frustule of the alga *Amphipleura pellucida*. The results corroborate the role of van der Waals interaction in matter-wave single-grating diffraction and demonstrate the feasibility of the realization in the near future of coherent control schemes, e.g. holography, with complex molecules.

Zusammenfassung

Die Moleklinterferometrie ist inzwischen ein weites Forschungsfeld. Sie bietet einerseits die Mglichkeit, an grundlegende Fragen der Quantenmechanik zu forschen und andererseits die Option molekulare Eigenschaften zu bestimmen. Fr die Realisierung des Welle-Teilchen Dualismus mit sehr massiven Teilchen mssen neuartige Methoden entwickelt werden um neutrale, langsame Molekle in einen Strahl zu bringen. Darber hinaus bentigt man neue Detektionsmechanismen, um einzelne Molekle nachweisen zu knnen.

Der erste Teil meiner Dissertation beinhaltet die Charakterisierung eines neuartigen supraleitenden Nanodrahtdetektors. Dieser wurde ursprnglich zum Nachweis von einzelnen Photonen entworfen und wird daher hufig auch als supraleitender Einzelphotondetektor bezeichnet. Ich konnte mit diesem Detektor neutrale, massive Teilchen grundstzlich detektieren und die Detektionsempfindlichkeit fr Ionen im Detail charakterisieren. Dazu wird in ein niederenergetischer He^+ -Strahl (0.2-1 keV) verwendet. Abschlieend diskutiere ich potentielle Anwendungen dieses neuartigen Detektors fr die Massenspektroskopie.

Im zweiten Teil meiner Arbeit widme ich mich der Untersuchung der Rolle von van der Waals Potentialen bei der Beugung von Moleklen am einzelnen Gitter. Um die Wechselwirkung zwischen polarisierbaren Moleklen (PcH_2 - 514 u) und SiN Oberflchen zu untersuchen, werden Interferogramme hinter verschiedenen Beugungsgittern (100 nm Periodizitt und Dicken zwischen 10 - 90 nm) gemessen und ausgewertet. Die Vorhersagen theoretischer Modelle werden dabei getestet und die Ergebnisse diskutiert. Abschlieend untersuche ich die Beugung von Phthaloncyaninen (PcH_2) an einer biologisch gewachsenen Nanostruktur, nmlich dem aus SiO_2 bestehenden Skelett der Alge *Amphipleura pellucida*. Die Ergebnisse untermauern die Rolle der van der Waals Wechselwirkungen in der

Materiewellenbeugung an einzelnen Gittern. Sie zeigen, dass Experimente zur kohärenten Kontrolle von Molekülstrahlen, z.B. bei der Holographie mit komplexen Molekülen, in naher Zukunft durchgeführt werden können.

Introduction

Il est vrai à la fois que le monde est "ce que nous voyons" et que, pourtant, il nous faut apprendre à le voir.

- M. Merleau-Ponty - Le visible et l'invisible

The matter-wave dualism

According to our daily-based perception of reality, the observation of many physical phenomena can be essentially classified according to two different, antithetic categories: wave phenomena and particle-like pictures.

As a matter of fact, if we stick to the description of physical reality proposed by classical physics, the ideas of particles and waves are intrinsically conflicting. Given a Cartesian reference frame, the position of a particle at each time t is specified by a set of coordinates (x, y, z) and therefore a particle comes with the concept of *localization*. In addition, if we accept that we can not handle "a fractional amount of a particle", we can associate a particle to the concept of *discontinuity*.

On the contrary, a wave is defined as a physical quantity that extends over a wide region of space-time with an amplitude that can be arbitrarily tuned. Therefore the concept of wave comes with the idea of *delocalization* and *continuity*.

The price we have to pay in order to access the quantum description of physical reality is intriguing, since we are not allowed to ask certain questions anymore and we have to accept the fact that the word "*quantum*" implies that an object is *both* a particle *and* a wave.

According to the de Broglie hypothesis [dB23], the state of motion of the center of mass of a particle with rest mass m propagating with velocity

v is determined by a "phase wave" whose wavelength λ_{dB} is given by

$$\lambda_{dB} = \frac{h}{mv},$$

with h the Planck's constant.

If we want to describe how nature behaves on the microscopic scale, we have to give up the idea of a classical particle and we have to suppose that the time evolution of the physical state of a particle will be described by a set of equations that have a rigorous mathematical analog to the ones describing the physics of electromagnetic waves.

According to R. Feynmann, the matter-wave dualism "*has in it the heart of quantum mechanics. In reality it contains the only mystery*" [Fey65]. As a matter of fact, the "mystery" is even more intriguing if we consider that no mass limit is predicted by the de Broglie hypothesis. Therefore, we are allowed to ask ourself whether the reality we experience on an everyday basis is intrinsically classic or, as pointed out by the epigraph opening this chapter, we simply have to learn how to watch it in the right way.

After its formulation, the "mystery" of matter-waves has been the object of an intense experimental investigation, leading to the demonstration of the wave-like behavior of objects with increasing mass and complexity. While the quantum nature of small objects like electrons, light atoms, diatomic molecules and neutrons has been confirmed a few years after the introduction of de Broglie hypothesis [DG27, ES30, HP36], molecular quantum optics can still be regarded as a relative young field of research [CSP09].

Molecular interferometry

The first experimental demonstration of the wave behavior of a molecule (SF_6) dates back to 1981 [BAVL⁺81], whereas in 1999 Arndt and co-workers reported the quantum diffraction of a beam of fullerenes C_{60} (720 u) [ANVA⁺99]. Later on, molecular matter-wave interferometry has grown into a powerful and fruitful experimental field allowing the investigation of mechanisms related to the foundation of quantum physics as well as the performance of quantum assisted metrology measurements [HUB⁺03, HHB⁺04, GGU⁺08].

If a matter-wave interferometer represents the most natural experimental choice for the investigation of the quantum behavior of a particle, single-grating diffraction in the far-field is probably the simplest and most direct way of realizing it. Under the appropriate experimental conditions, the coherent illumination of a diffraction grating with periodicity d with a collimated beam of particles leads to the formation of an interference pattern whose n -th interference maxima can be found at a diffraction angle ϑ according to the well known relation

$$\vartheta_n = n \cdot \frac{\lambda_{dB}}{d}.$$

The most fascinating aspect of far-field interferometry is perhaps represented by the fact that no classical equivalent is able to account for the effect. The delocalization of the position state of a single particle over a space range exceeding by several orders of magnitudes its chemical linear dimensions is a genuine fingerprint of its quantum wave-like behavior. Recently, the combination of far-field interferometry with single molecule fluorescence imaging has enabled to see the real-time build-up of the interference fringes resulting from the diffraction of a thermal beam of phthalocyanine (514 u) with a 100 nm diffraction grating in a beautiful, pedagogic way [JMM⁺12].

Due to its simplicity, far-field interferometry has been frequently exploited for the successful investigation of quantum mechanics and for the application of coherent control schemes to nano-technology. To name just a few, the diffraction pattern of a supersonic beam of cold helium has lead to the discovery of helium dimers and trimers [ST96, STSS98], while the coherent evolution of electrons and atoms has paved the way for applications in lithography and microscopy [FMK⁺96, SF02, CSS⁺91, DGR⁺99, ERG⁺12].

At the same time, grating diffraction has been used for studying the interaction of polarizable particles with conducting surfaces probing the subtle but fundamental role of van der Waals (vdW) interactions in matter-wave interferometry with material gratings [GST⁺99, LKHC10, BFG⁺02].

As a matter of fact, the van der Waals interactions between a particle and a grating wall has been often reported as one of the possible limiting factors for atomic and molecular interferometry both for quantum assisted metrology experiments - as they rely on the phase sensitivity of matter waves - and for the exploration of the quantum nature of complex parti-

cles with material gratings - as vdW interactions might lead to undesired absorption or dispersion effects - [BSDA07, NKUA08, CWP].

Furthermore, the fact that the periodicity of the diffracting element scales linearly with the wavelength associated to the state of motion of the particle has been recognized as a limit for the investigation of the quantum wave nature of objects beyond several thousands atomic mass units. Therefore, alternative interferometer schemes in the near field regime with optical diffraction elements have been successfully proposed and realized [GHH⁺07, HDG⁺13]. While the realization of a Kapitza-Dirac-Talbot-Lau interferometer has allowed the extension of the mass record of quantum diffraction up to compounds with $m = 10,123$ u [GET⁺11, EGA⁺13], an interferometer in the time domain might represent the most promising experimental choice for the exploration of quantum mechanics with nano-sized particles [NHHA11, HDG⁺13].

By giving a "critical" look to an ideal time line of matter-wave interferometry, we may notice how, in spite of the astonishing number of successful results achieved, if compared to the C₆₀ (720 u) diffraction experiment, the mass range of the diffracted object has increased so far "only" by a factor fourteen. Like any young research field, matter-wave interferometry presents a wide class of experimental challenges and difficulties. One has to bear in mind that *"interference experiments are only as good as their beam sources and detectors"* [HGH⁺12].

A matter-wave interferometer can be schematically pictured as composed of three different experimental stages. Molecules have to be promoted as neutral particles into the gas phase, diffracted at the interference stage and finally detected for the retrieval of the diffracted intensity populations.

The generation of a stable, intense beam of slow neutral particles as well as the access to truly, high sensitive single molecule detection schemes both represent a key feature for any successful quantum optics experiment with large molecules. In particular, the neutral requirement is necessary to avoid any dephasing resulting from the interaction of the matter-wave with stray electromagnetic fields, whereas a slow velocity is desirable to match the dimensions of the de Broglie wavelength of massive particles with the available interferometers.

The two requirements are often intimately related. Indeed, while the promotion into the gas phase of molecules with a mass exceeding 10,000 u is

rather challenging, at the same time the efficiency of conventional detection schemes based on post-ionization mechanisms is limited for molecules in this mass range [SGL92].

So far, the detection schemes used in matter-wave interferometry have mainly relied on post ionization in combination with mass spectrometry. Effusive beams of thermo-resistant molecules are typically ionized via electron bombardment and mass discriminated in a quadrupole mass spectrometer. Alternatively, supersonic expanding pulsed beams are usually detected with single or multiple photo-ionization process and further mass selected according to their time of flight.

While electron impact at 60 eV often yields to the undesired occurrence of molecular fragments, the photoionization is often regarded as "soft" as the energy for the promotion of an electron into the ionization continuum can be provided by the absorption of a single photon in the UV frequency range with photon energies around 5-8 eV [HZ09]. Both schemes are normally combined with mass filters whose final detection stages rely on secondary electron emission. The efficiency of the detection process scales a power law of the velocity of the selected ion and, as mentioned before, it is dramatically reduced for molecules with a mass beyond 10,000 u [BCDN⁺97]. The total detection efficiency of ionization detectors in this range can be as low as 10^{-4} [GS00].

Alternative detection schemes based on imaging processes of surface deposited molecules, e.g. fluorescence microscopy and scanning tunneling microscopy (STM), have been successfully explored by our research group [JTG⁺09, JMM⁺12]. Nevertheless, STM appears to be restricted by its characteristic long acquisition time and small repetition rate. On the contrary, fluorescence microscopy has been shown to be highly efficient, although naturally limited to fluorescent molecular species.

Therefore, the need for novel detection schemes is highly attractive, especially for future tests of matter-wave interferometry with nano-sized particles.

Contents

The thesis is mainly divided into two parts.

In the first part, I will introduce the reader to the idea of a novel super-

conducting detector for the registration of particle beams. It relies on the local suppression of superconductivity in a nanometer-sized NbN wire which was originally developed for the detection of single IR photons [SGK01, VZS⁺02]. Here, the nano-wire detector is tested in combination with different molecular beam sources. A proof-of-principle test for the detection of jet-cooled supersonic beams of biological molecules is presented and the feasibility of neutral nano-particles detection is discussed. Moreover, I will provide a comprehensive characterization of the detection process with a beam of ionized helium in the low kinetic energy range (0.2-1 keV) and discuss its potential applications to molecular spectroscopy.

- In **chapter 1**, I will shortly review the main concepts of the kinetic gas theory and list some relevant statistical mechanics properties. These concepts will be useful for the theoretical understanding of the different beam production methods used for the characterization of the superconducting detector. The experimental realization of a laser desorption source for small organic compounds is presented together with an effusive-supersonic oven for the realization of C₆₀ beams with a kinetic energy up to 20 eV.
- In **chapter 2**, I will present a short historical review about the applications of cryogenic detectors in mass spectrometry. Then, I will sketch the theoretical framework for the understanding of the working principle of our superconducting nano-wire detector. Finally, the experimental results achieved will be shown and discussed.

In the second part of the thesis, I will focus on the role of van der Waals interactions in matter wave interferometry with material diffraction objects. The far-field diffraction pattern of a thermal beam of phthalocyanine (514 u) is deposited onto a quartz surface and imaged *in situ* with an self-built epi-fluorescence microscope. The role of the grating geometry in vdW interactions will be discussed by analyzing the diffraction patterns collected with different silicon nitride (SiN) and carbon (C) gratings. A qualitative interpretation of the data is provided and we discuss the limits of the theoretical models used for the evaluation of the experimental results. Finally, I will present the first demonstration of the quantum delocalization of a complex molecule over a biologically grown nano-structure, namely the skeleton of the diatom alga *Amphipleura pellucida*. The results

achieved confirm the robustness of our experimental setup and provide a proof-of-principle demonstration of the feasibility of future holography experiments.

- In **chapter 3**, I will review the main theoretical concepts related to matter-wave fields, demonstrating the mathematical analogy between matter-waves and electromagnetic waves and introducing the concept of transversal coherence.
- In **chapter 4**, I will provide a detailed description of the experimental setup, introducing the working principle of a micro-focus laser evaporation and reviewing the main theoretical aspects of single molecule fluorescence imaging. I will focus on the particular case of the interference from a diffraction grating and illustrate the eikonal approximation for the evaluation of van der Waals interactions. The main experimental results will be illustrated and discussed.

Part I

From molecular beam production to superconducting nano-wire detectors

Chapter 1

Molecular beam production

1.1 Introduction

Molecular beams are among the most fruitful research tools of 20th century physics and chemistry. Just to name a few examples, gas-phase molecular beams have allowed the first experimental verification of the kinetic theory of gas [Ste20], the demonstration of the spatial quantization of the intrinsic angular momentum of atoms [GS22], or the first experimental confirmation of the de Broglie hypothesis for the wave behavior of heavy particles [ES30].

The production of an intense beam of particles represents a basic requirement for many quantum optics experiments and the choice of the right source is defined by the research aim. Our investigation was originally motivated by the desire to investigate the limits of quantum mechanics by exploring the wave behavior of particles with increasing mass and complexity through matter-wave interferometry. In particular, we were interested in the production of intense beams of neutral particles.

Because of its low realization costs, its simplicity and above all its flux to stability ratio, an effusive source is probably the easiest way to achieve a molecular beam: particles are simply heated within an oven and further evaporated into the gas phase. On the other hand, a simple thermal source presents a considerable experimental limiting factor: particles exceeding few thousands atomic mass units are often characterized by a low vapor pressure and thermo-lability. As a result, they either hardly access the gas phase or they tend to fragment before the evaporation process takes place. A possible solution to this problem is provided by the synthesis of tailor-made molecules. Effusive beams of thermo-resistant molecules

with mass up to 10,000 u were successfully used for proving the quantum delocalization of compounds as large as 60 Å in a near-field matter-wave interferometer [GET⁺11, EGA⁺13].

A further possibility is represented by the exploration of alternative production techniques, especially if we would like to profit from the unique "zoo" of species offered by biological molecules, such as nucleotides, amino acids, proteins or even objects like viroids or viruses. Laser desorption techniques (LD), have been recently discussed as a potential source for matter-wave interferometry [Mar10].

Once neutral molecules are promoted into the gas phase, they need to be detected with a suitable detection scheme. Within our experimental setups, a detection stage consists usually of three different elements:

- *an ion source*: for the ionization of the neutral molecules,
- *a mass filter*: for the selection of the ions as a function of their mass-to-charge ratio m/q . A quadrupole mass spectrometer (QMS) or a time-of-flight mass spectrometer (TOF-MS) are routinely used for mass filtering.
- *an ion detector*: for the conversion of a detection event into a measurable signal. Nowadays, neutral beams are conventionally detected with post-ionization techniques, surface ionizers or electron impact ion sources.

Photo-ionization of laser desorbed molecules in combination with TOF-MS has been broadly investigated by our research group leading to the comparison of different photo-ionization schemes and the investigation of the production of large organic clusters [MHU⁺08, MHS⁺09]. At the same time, a major experimental drawback of laser desorption is represented by the fact that the post-ionization process tends to fail for organic particles whose mass exceeds a few thousands atomic mass units [SGL92, HEC⁺06, SL92]. The functionalization of molecular complexes for which the photo-ionization efficiency still holds beyond the 10 kDa¹ has been recently proposed as a potential solution to this problem for future applications in matter-wave interferometry [SSA⁺13].

¹A Dalton is the mass unit preferred by chemists: 1 Da = 1 u.

In this thesis, LD in combination with photo-ionization TOF-MS is mainly exploited for testing the feasibility of the detection of neutral particles with a novel superconducting nano-wire device (see Section 2.6). As a consequence, in this chapter I will focus on the theoretical and experimental background of two different neutral particles sources.

1.2 Theoretical outlook

1.2.1 Fundamentals of kinetic gas theory

Our description of the different techniques used for the production of molecular beams will move from a short inspection of the principal results of the kinetic theory of gases together with a review of some main concepts of statistical mechanics. The derivation of the formula will be omitted since it can be found in numerous textbooks. In the following, I will mainly refer to the treatises by H. Pauly and G. Scoles [Pau00, Sco88].

Let us begin with the following *working hypothesis*: we define a gas as a thermodynamic system consisting of a large number of particles N with a mass m and which is kept in a volume V at pressure P . Particles are in permanent motion and they generally do not interact with each others but they are allowed to exchange energy or linear momentum through collision processes. Finally, we will assume that the total energy ε_i of a particle in the given i -th quantum state can be written as the sum of a translational contribute ε_{tr} , a vibrational term ε_{vib} and a rotational term ε_{rot} according to the relation

$$\varepsilon_i = \varepsilon_{tr} + \varepsilon_{vib} + \varepsilon_{rot}.$$

Under these assumptions, the number of particles N_i in the i -th state with energy ε_i is given by the equilibrium distribution

$$N_i = \frac{N}{Z} g_i \exp(-\varepsilon_i/k_B T), \quad (1.1)$$

where g_i represents the statistical weight of the i -th state while Z is the *partition function* which is defined as

$$Z = \sum_i g_i \exp(-\varepsilon_i/k_B T). \quad (1.2)$$

1.2.1.1 Velocity distribution

The number of particle whose absolute velocity lays between v and $v + dv$ is given by the *Maxwell distribution*

$$f(v) = \frac{4}{\sqrt{\pi}} \left(\frac{m}{2k_B T} \right)^{3/2} v^2 \exp \left(-\frac{mv^2}{2k_B T} \right). \quad (1.3)$$

The most probable velocity v_w , i.e. the speed at which the distribution has its maximum is given by [Pau00]

$$v_w = \sqrt{\frac{2k_B T}{m}} \simeq 1.3 \times 10^4 \sqrt{\frac{T}{M}} \text{ [cm/s]}, \quad (1.4)$$

whereas the average molecular velocity \bar{v} is given by

$$\bar{v} = \int_0^\infty v f(v) dv = \sqrt{\frac{8k_B T}{\pi m}} \simeq 1.5 \times 10^4 \sqrt{\frac{T}{M}} \text{ [cm/s]}. \quad (1.5)$$

Here, T is expressed in Kelvin and the mass of the particle M is expressed in atomic mass units.

1.2.1.2 Mean free path

As a molecular beam can be essentially defined as a set of particles propagating without any interaction along a well defined direction in an evacuated chamber, it is interesting to estimate the average length traveled by a particle between the occurring of two consecutive collision events. This distance is defined as the *mean free path*. Let us consider a gas species propagating with velocity v through a chamber at temperature T , pressure P . If we assume the chamber to be filled with a second gas species with density n and a most probable velocity \tilde{v}_g , the mean free path can be expressed as [Pau00]

$$\Lambda = \frac{1}{n\sigma\sqrt{2}} = 5.5 \times 10^{-6} \frac{T}{P\sigma} \text{ [cm]}. \quad (1.6)$$

Here, σ represents the scattering cross section and it is expressed as [HUB⁺03]

$$\sigma = \left(\frac{C_6}{\hbar} \right)^{2/5} \frac{\tilde{v}_g^{3/5}}{v} \left[8.5 + 1.7 \left(\frac{v}{\tilde{v}_g} \right)^2 \right], \quad (1.7)$$

where the parameter C_6 takes into account the effects of the London dispersion interaction and depends on the composition of the particle through its polarizability².

1.2.1.3 Rotational and vibrational states distribution

Solving the rotational and vibrational energy levels distribution of a polyatomic molecule is far from being trivial. Let us then focus on the simplest case of a heteronuclear diatomic molecule.

The rotation state of a diatomic molecule will be labeled by j whereas we will refer to its degeneracy as $g_j = 2j + 1$. The rotational energy is defined as

$$\varepsilon_{rot}(j) = hcBj(j+1) \quad \text{with} \quad B = \frac{h}{8\pi^2 Ic}, \quad (1.8)$$

with c the speed of light and with I the moment of inertia of the molecule.

The number of molecules N_j in the given j -th rotational state is given by [Pau00]

$$N_j = \frac{N}{Z_{rot}}(2j+1) \exp(-\Theta_{rot}j(j+1)/T) \quad \text{with} \quad \Theta_{rot} = hcB/k_B. \quad (1.9)$$

For low temperatures, i.e. for $\Theta_{rot}/T \geq 1$, the rotational contribution to the internal energy of the system can be written as

$$E_{rot} = 6Nk_B\Theta_{rot} \exp(-2\Theta_{rot}/T). \quad (1.10)$$

If we approximate a diatomic molecule with a harmonic oscillator, the energy of the n -th vibrational state is then given by

$$\varepsilon_{vib}(n) = \hbar\omega\left(n + \frac{1}{2}\right), \quad (1.11)$$

where ω is a molecular constant providing an indication of the "stiffness" of the molecule. The vibrational contribution to the total energy can be expressed as [Pau00]

$$E_{vib} = Nk_B\Theta_{vib} \exp\left(\frac{1}{2} + \frac{1}{\exp(\Theta_{vib}/T) - 1}\right) \quad \text{with} \quad \Theta_{vib} = \hbar\omega/k_B. \quad (1.12)$$

²For example, a molecule of fullerene C_{70} (840 u) propagating with $v=120$ m/s in a pressure of N_2 ($C_6 = 2.1$ meV nm⁶) at room temperature is characterized by a scattering cross section $\sigma \simeq 75$ nm² [HUB⁺03].

The characteristic temperatures Θ_{rot} and Θ_{vib} have been introduced because they have a very well defined physical interpretation. They both represent an estimation of the temperature at which the thermal energy $k_b T$ is comparable with the energy spacings of the rotational or vibrational levels. In other words, at these temperatures, the population of the excited levels becomes significant. Since the ratio $\Theta_{vib}/\Theta_{rot} = \omega/B > 1$, temperatures that are normally considered vibrationally low qualify already as rotational high. At room temperature for example, the rotational states distribution is generally full developed while almost all molecules still linger in the lower vibrational states.

1.2.1.4 Effusive source - Knudsen cell

An effusive source can be essentially pictured as a volume V filled with a molecular gas at temperature T . The reservoir has a small opening which connects the system to a low pressure region and through which molecules can effuse. If we assume the area of the aperture to be smaller than the total area of the recipient walls, the thermal equilibrium properties of the gas inside the cell will not be affected by the effusing particles. The previous statement can be rephrased in a more physical way by saying that the mean free path of the particles inside the cell is larger than the diameter of the aperture or, in case of a rectangular slit, than the slit width. The fact that the system is kept at thermal equilibrium yields a well defined equilibrium distribution of the internal states, a requirement achieved not so often in many molecular sources.

The flux of particles propagating into the solid angle element $\Delta\Omega$ can be written as [Pau00]

$$\frac{I(0)}{\Delta\Omega} = 1.118 \times 10^{22} \frac{P_0}{\sqrt{MT}} A \quad [\text{particles sr}^{-1}\text{s}^{-1}], \quad (1.13)$$

where P_0 is the pressure inside the source expressed in Torr, A is the area of the source aperture in cm^2 .

From equation 1.13, we find that the maximum flux is achieved when the linear dimension of the slit is of the same order of the mean free path Λ , i.e. when $A = \pi\Lambda^2$ for a circular aperture or $A = h\Lambda$ for a slit with width h .

1.2.2 Fundamental principles of gas dynamics

One of the most striking experimental limit of an effusive source is represented by its relative low beam intensity. We might naively think to overcome this problem by increasing the pressure of the source up to the limit given by the mean free path, but the opposite result would be actually observed: the number of collisions inside the reservoir becomes so dominant that the formation of a cloud in front of the source exit results in an undesired attenuation of the beam intensity.

The idea of making use of the gas dynamic expansion through nozzles rather than of effusive sources led to the realization of supersonic beams [KG51]. As we will see, the properties of molecular jets differ significantly from beams emitted by Knudsen cells. The differences are mainly related to the large number of collisions. The gas dynamic process results in an improvement of the velocity selection, in a shift of the mean velocity towards higher values as well as in a fair reduction of the internal states distribution.

1.2.2.1 One-dimensional flow

For the sake of clarity, let us focus on the steady flow of a homogenous gas. We will assume the process to be isentropic, i.e. we will neglect any energy variation related to the interaction of the gas with its surrounding. Moreover, we will limit our investigation to the properties of one dimensional flows, i.e. we will consider the flow velocity w , the gas density ρ , the pressure P and the temperature T of the gas to be uniform over any cross section A taken along the propagation direction of the beam. The one dimensional flow approximation is experimentally justified if the cross section of the nozzle varies in a slow way along the flow direction.

Under these assumptions, the equations governing the gas dynamics processes can be expressed as [Pau00]

$$\text{Continuity equation} \quad \frac{dw}{w} + \frac{d\rho}{\rho} + \frac{dA}{A} = 0, \quad (1.14)$$

$$\text{Momentum conservation} \quad w dw + \frac{dp}{\rho} = 0, \quad (1.15)$$

$$\text{Energy conservation} \quad w dw + dH = 0, \quad (1.16)$$

where H indicates the enthalpy of the system.

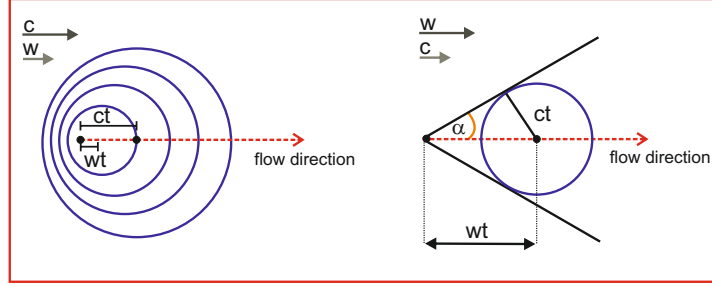


Figure 1.1: Illustration of the propagation of a sound wave with velocity c in a medium flowing with velocity w . Left: $w < c$. In the lab reference frame, the sound wave emitted from a point x_0 moving with velocity w will propagate with velocity $w + c$. Right: $w > c$. In the supersonic flow, the sound wave propagation is confined within the wave front defined by the Mach cone α . Illustration adapted from [Pau00].

The speed of sound c of an ideal gas, i.e. the propagation velocity of a sound wave in a continuous medium is given by the relation

$$c = \sqrt{\kappa \frac{P}{\rho}} = \sqrt{\kappa \frac{RT}{M}}, \quad (1.17)$$

with $\kappa = c_p/c_v$ the specific heats ratio and R the universal gas constant per mole.

A perturbation is said to propagate *supersonically* if $w > c$. The physical situation is schematically pictured in figure 1.1, which illustrates a pressure disturbance propagating with velocity c in a medium flowing with velocity w . In the medium reference frame, the sound wave propagates with velocity c . Alternatively, in the lab frame the wave will propagate with a relative velocity $c + w$. As illustrated on the left part of figure 1.1, if $w < c$ the disturbance will propagate upstream with velocity $c - w$ while it will move downstream with velocity $c + w$. For a supersonic flow where $w > c$, the sound wave will propagate in the downstream direction only and all front waves appear to be confined within a wave front which defines the *Mach cone*

$$\sin \alpha = \frac{c}{w} = \frac{1}{M_a}. \quad (1.18)$$

Here, M_a represents the *Mach number* and is defined as the ratio between the flow velocity and the local speed of sound. The Mach number enters directly in the equation governing the change of the flow velocity w through

a cross-sectional area A according to the differential equation

$$\frac{dA}{A} + \frac{dw}{w} (1 - M_a^2) = 0. \quad (1.19)$$

According to equation 1.19, for a gas propagating in a subsonic way ($M_a < 1$), the flow velocity decreases with increasing area. On the contrary, if $M_a > 1$ the flow velocity increases/decreases with increasing/decreasing area. As a consequence, convergent-divergent nozzles (*Laval nozzle*) are normally used for the production of supersonic expanding beams.

Integration of equation 1.16 yields the expression for the isentropic velocity of a gas expanding from a reservoir at (T_0, P_0) to a system at (T, P) [Pau00]:

$$w = \sqrt{2 \frac{\kappa}{\kappa - 1} \frac{RT_0}{M} \left(1 - \frac{T}{T_0}\right)} = \sqrt{2 \frac{\kappa}{\kappa - 1} \frac{RT_0}{M} \left[\left(1 - \frac{P}{P_0}\right)^{(\kappa-1)/\kappa}\right]}, \quad (1.20)$$

whereas its most probable value is given by

$$w_{max} = \sqrt{2 \frac{\kappa}{\kappa - 1} \frac{RT_0}{M}} = v_w \sqrt{\frac{\kappa}{\kappa - 1}}. \quad (1.21)$$

By combining equation 1.17 with equation 1.20, we can re-formulate the expression of the Mach number as

$$M_a = \frac{w}{c} = \sqrt{\frac{2}{\kappa - 1} \left(\frac{T_0}{T} - 1\right)} = \sqrt{\frac{2}{\kappa - 1} \left[\left(\frac{P_0}{P}\right)^{(\kappa-1)/\kappa} - 1\right]}. \quad (1.22)$$

If $M_a = 1$, equation 1.22 returns the critical value of the pressure ratio for the realization of a sonic flow from a nozzle, i.e.

$$\frac{P_0}{P} \geq \left(\frac{\kappa + 1}{2}\right)^{\kappa/(\kappa-1)} \quad (1.23)$$

whose typical value is as small as 2.1 for all gases. For noble gases, $\kappa = 5/3$ yields $P_0 \geq 2P$ and the maximal velocity is on average a factor 1.6 faster than the one associated to an effusive beam with the same boundary conditions.

The characteristic features of a free-jet expansion are illustrated in figure 1.2. The gas in the reservoir is kept at rest at (T_0, P_0) and is accessing the vacuum region ($P_a < P_0$) through a Laval nozzle with an orifice diameter d . Due to the imposed pressure difference, the gas is accelerated towards the

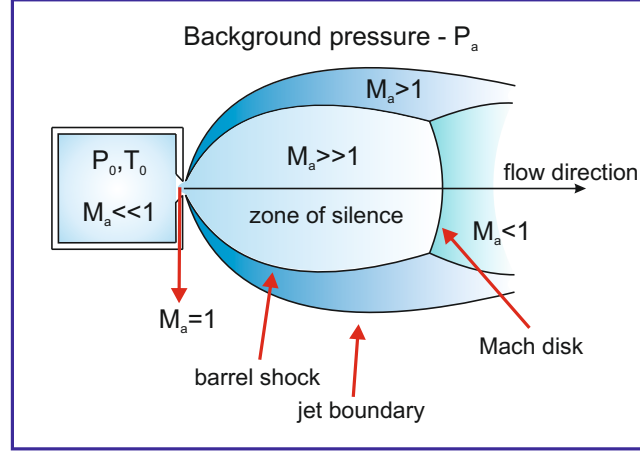


Figure 1.2: Illustration of a free jet expansion from a reservoir at P_0 into a vacuum system at P_a . Illustration adapted from [Pau00].

decreasing cross-section of the nozzle. The solid lines represent the free jet beam boundaries, i.e. the region where the expanding waves are reflected and define the shape of the supersonic beam. Since the supersonic flow is unable to sense the boundary conditions downstream, the central zone of the beam is often referred as the *zone of silence*. The *Mach disk* represents the spatial region where the pressure of the free jet adjusts itself to the boundaries and further collapses to its initial value. Its position x_M along the direction of flow can be expressed as a function of the orifice diameter d according to the relation

$$\frac{x_M}{d} = 0.67 \sqrt{\frac{P_0}{P_a}}. \quad (1.24)$$

The velocity distribution for a supersonic expanding gas can be written as [Sco88]

$$f(v) \propto \left(\sqrt{\frac{M}{2k_B T}} \right)^\nu v^\nu \exp\left(-\frac{M(v-w)^2}{2k_B T} \right) \quad (1.25)$$

where ν is defined by the detection scheme used and amounts to $\nu = 2$ for a density detector or $\nu = 3$ for a flux detector.

Finally, during the expansion process a single molecule experiences a total number of binary collisions which is typically of the order 10^2 to 10^4 . As the vibrations of polyatomic molecules and the rotation of most diatomic molecules require on average only 10 to 100 binary collisions

to thermalize with the translational degrees of freedom, these modes are frozen out during the expansion mechanism.

1.3 Experimental outlook

1.3.1 Generation of pulsed beams

1.3.1.1 A brief overview

The principles of supersonic expanding gases will be exploited here in combination with laser desorption techniques for the production of beams of thermo-labile samples. Molecules introduced into the gas phase after the desorption process are embedded in a supersonic expanding beam of helium, resulting in the production of an intense jet of cooled neutral particles.

As previously mentioned, the introduction of molecules into the gas phase with a mass exceeding few thousands atomic mass units is experimentally challenging and rather inefficient. The general idea is thus to "borrow" some of the experimental procedures used in mass spectrometry. The production of beams of ionized particles up to the MDa range is nowadays conventionally achieved through electro-spray ionization (ESI) [FMM⁺89] and matrix assisted laser desorption/ionization (MALDI) [KBH85, TWI⁺88, KH88]. In particular, with MALDI techniques the promotion into the gas phase of both neutral and ionized species is achieved by embedding single analyte molecules in a solid matrix. A large amount of energy is then pumped into the system by photon absorption leading to the onset of the desorption process. The basic idea of our laser desorption source will be to simply avoid the matrix and to look at the macromolecules as their own matrix itself.

In spite of the large attention received by the mass spectrometry society, the physical mechanism of the desorption mechanism is still poorly understood. Although an extensive literature could be provided, only few consistent experimental observations can be found. The most relevant experimental aspects of MALDI relevant will be here shortly discussed following the work of *Dreisewerd et al.* where a comprehensive bibliography is also provided [Dre03].

MALDI is often regarded as a "soft" technique since the role of the

solid matrix is to prevent the aggregation of analyte molecules, to be responsible for the energy absorption of the laser pulse via electronic (UV) or vibrational (IR) excitations and primarily to prevent an excessive heating of the embedded analyte molecules. Cooling of the hot desorbed plume is further achieved by *jet-cooling*, i.e. by embedding the ablated molecular plume into a supersonic expanding gas pulse [MdVHW90].

The influence of the laser wavelength on the desorption process has been largely investigated. N₂ lasers at 337 nm or the third harmonic of a Nd:Yag laser at 355 nm are generally used with a pulse duration selected in a time scale ranging from 0.5 to 10 ns. Kinsel *et al.* compared the effects of resonant (266 -355 nm) vs non-resonant (532-1024 nm) laser desorption of neutral organic molecules, reporting a significantly higher efficiency for the production of intact molecular species when the pulse energy was directly pumped in the sample species (resonant mode) [KLG91]. They concluded that both the desorption and the multi-photons ionization of neutral intact molecules was significantly less efficient when the sample was illuminated with a non-resonant laser pulse.

A large number of experiments have focused on the estimation of an energy threshold of the desorption mechanism, on the role of the laser beam profile, on the size of the irradiated area or on the duration of the laser pulse. A large variation of these values can be found in literature and generally speaking, we might paraphrase what was reported by Horneffer *et al.* about the proper choice of a matrix in a MALDI experiment and the right choice of the experimental parameter suitable for a successful LD experiment: "*no general scheme has evolved so far that would allow an a priori prediction of the performance of a particular technique*" [HDL⁺99].

Finally, molecular dynamics simulations tend to generally corroborate the experimental observations, supporting the idea that both the physical-chemical properties of the analyte molecule and the specifications of the laser used for the desorption mechanism play a relevant role for the efficiency of the process. In particular, a key role is often attributed to the heating rate $\beta = dT/dt$, i.e. to the time scale involved in the photon absorption process. In laser desorption this parameter can be as high as $10^{10\pm2}$ K/s [Lev94]. According to the "*breathing sphere model*" developed by Zhigilei *et al.* [ZKG97], if the heating of the system takes place on a time scale smaller than its mechanical relaxation (≈ 10 ns), a large amount of energy is stored in a constant volume before thermal expansion occurs. The overall mech-

anism can thus be pictured as an increasing gradient of pressure in the heated volume, giving rise to an explosive force that is able to drive the acceleration of the ablated molecules in a direction normal to the surface layers. As soon as this force overcomes the surface tension of the external layers, ablation is set up and molecules are ejected.

1.3.1.2 Experimental realization of a laser desorption source

The experimental setup of our LD source is schematically illustrated in figure 1.3. The production of the molecular beam takes place in a vacuum chamber whose pressure is kept in the range 10^{-5} - 10^{-3} mbar. The main body of the source consists of a stainless steel mixing channel where the molecular target is mechanically screwed to one end whereas a fast valve³ is connected on the other. The valve is connected to an helium reservoir whose stagnation pressure is typically maintained at 2 bar. Helium pulses are released through a 500 μm diameter opening with a duration time set between 500 and 700 μsec . Helium pulses expand in the closed channel and reach the molecular sample position where the laser ablation process takes place. The time delay between the valve opening and the laser pulse is optimized while monitoring the molecular beam intensity. Single molecules embedded in a cold helium jet finally expand in a supersonic way through a 0.5 mm radius orifice into the vacuum.

Neutral molecules are first introduced into the gas phase through laser ablation. The third harmonic of a Nd:Yag laser⁴ at 355 nm is focused on the surface of the molecular sample with a spot that can be arbitrary adjusted by simply varying the position of the focusing lens and which is usually optimized while monitoring the molecular beam intensity. The laser pulse has a duration of 5 ns and its power is optimized while looking at the shot to shot stability of the intensity profile and is typically set to 10 mJ. The "zigzag" geometry of the mixing channel guarantees that the small window through which the laser pulse reaches the molecular sample is constantly purged by the helium pulse. In this way, desorbed molecules are unable to stick on its surface leaving the transmission of the ablation laser unaffected.

A typical sample used with our LD source consists of a commercially

³Parker-General valve 99.

⁴Quantel, Brilliant - 355 nm, $\tau=5$ ns, $E_{\text{max}}=100$ mJ at 10 Hz repetition rate.

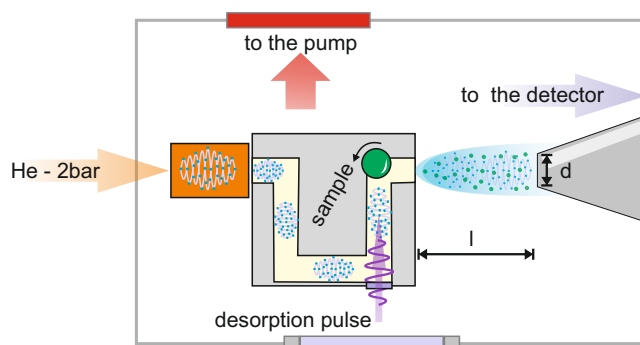


Figure 1.3: Illustration of the laser desorption source. A 355 nm laser pulse (5 ns - 10 mJ) is focused onto a molecular target. Desorbed molecules are embedded in a helium pulse (2 bar - 500 μ s) and expand through a 0.5 mm orifice into a vacuum of 10^{-5} - 10^{-3} mbar. The beam enters the detection chamber through a skimmer opening with a diameter $d=1$ mm placed at a distance $l=1-2$ cm downstream.

available powder⁵ of different molecular species mechanically pressed onto a stainless steel fine-threaded rod. The sample is gently rotated by a piezo driven motor in order to constantly expose fresh molecular portions to the laser pulse. The powder is generally mixed in a weight ratio 1:1 with cellulose powder⁶ for a better mechanical stabilization on the metallic surface.

Finally, the molecular beam enters the detection chamber through a 1 mm diameter opening skimmer placed approximately 1-2 cm downstream the mixing channel, i.e. well before the Mach disk zone (see equation 1.24).

1.3.1.3 Principles of photo-ionization

In our experimental setup, pulsed molecular beams are detected by photo-ionization in combination with a time-of-flight mass spectrometer. The photo-ionization process is often regarded as one of the "softest" detection schemes in the sense that the fragmentation of the incoming particle is considerably reduced when compared with other post-ionization processes e.g. electron bombardment or collision with beams of ionized species with a kinetic energy up to several keV [AMB94].

The energy needed to promote an electron from the ground state to the

⁵Generally purchased at Sigma-Aldrich.

⁶Fluka - Avicel PH 101.

ionization continuum is provided by photon absorption. As sketched in figure 1.4, the amount of energy for overcoming the ionization potential (IP) can be provided in a direct way with the absorption of a single photon (SPI), or in a "ladder-way" via multi-photon absorption (MUPI).

A particular advantage of single photon ionization lays in its simplicity: by exposing an atom or a molecule to deep UV radiation, the ionization process will take place if the ionization potential of the target is equal or less than ≈ 8 eV. In particular, this value represents the ionization energy of most organic molecules [HZ09]. Furthermore, since the ionization potential of the gases typically used in supersonic expansion exceeds the VUV energy range, single photon ionization guarantees optimal signal to noise ratio and undesired counts related to the ionization of the background gas can thus be neglected. A main experimental drawback is related to the commercial availability of VUV light sources, since VUV inlines are typically generated by excimer lasers or by synchrotron radiation.

Resonance-enhanced multiphoton ionization (REMPI) represents an interesting variation of MUPI. The ionization process takes place upon the absorption of two consecutive photons through the excitation of the molecule in an intermediate state. The main advantage of this scheme is represented by its high selectivity and sensitivity and it has been described to be particularly suitable for the detection of aromatic hydrocarbons. The influence of the intermediate state lifetime to the photo-ionization yield has been largely investigated by comparing the ionization efficiency with ns and fs laser pulses [AWG95, WAW⁺94].

A further ionization mechanism involving multi-photon absorption is represented by the thermionic effect where the absorption of many photons results in the ejection of one or several electrons. The ejection process is typically observed on a delayed time window with respect to the absorption of the laser. This mechanism has led to the observation of the photo-ionization of fullerenes C_{60} and C_{70} with weakly focused cw lasers [DHC⁺94, HE97] and has been exploited for the first demonstration of the quantum wave-like behavior of complex molecules [ANVA⁺99].

The major drawback of photo-ionization is represented by the fact that its efficiency drops tremendously for organic molecules exceeding a few thousands atomic mass units. The mass spectrometry community has largely speculated over the problem proposing several models and ideas. The work of *Becker et al.* suggested that no experimental data has been

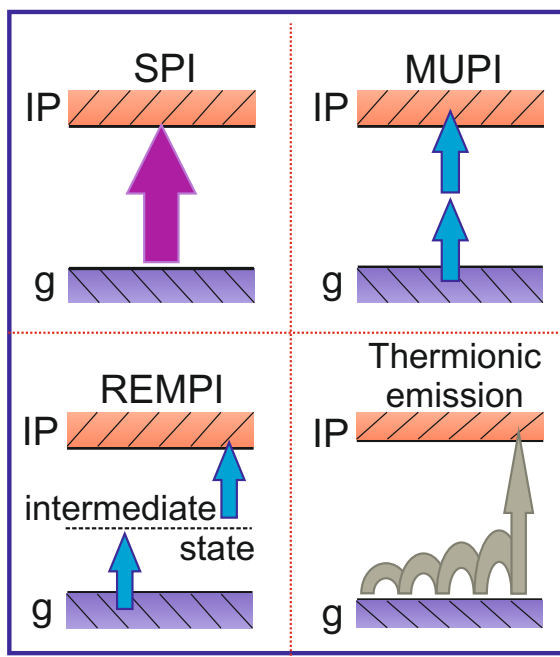


Figure 1.4: Illustration of the different photo-ionization mechanisms. An electron from the ground state g can overcome the ionization potential (IP) with: SPI: single photon ionization; MUPI: Multi-photon ionization; REMPI: Resonance-enhanced multiphoton ionization; thermionic emission. Illustration adapted from [Mar10].

provided so far in order to firmly support the theory that large molecules *do not* ionize and they indicated the enhanced fragmentation as the reason for the failure of the ionization process [BK95]. At the same time, Schlag *et al.* suggested that if we look at the molecule as its own solvent and we consider its chromophore group acting as a photo-donor, a molecule can easily redistribute the absorbed energy among its large number of degrees of freedom, populating different vibrational and rotational levels, thereby reducing the efficiency of the photo-ionization mechanism [SGL92].

The ion yield in single photon ionization can be expressed as [HKA⁺99]

$$\Upsilon = \sigma_{pi} I N_{neutral}, \quad (1.26)$$

where σ_{pi} represents the single photon absorption cross section, I is the radiation intensity and $N_{neutral}$ indicates the number of neutral molecules in the laser beam ionization area.

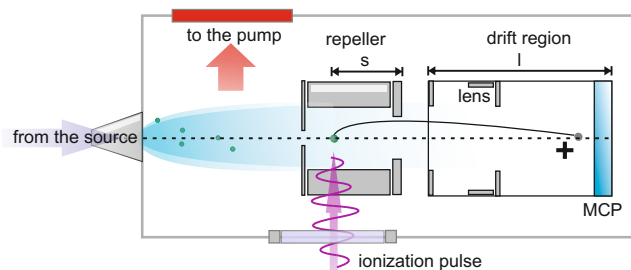


Figure 1.5: Schematic drawing of our TOF-MS. Molecules are photo-ionized by absorption of a single photon (157 nm, 5 ns - 3 mJ pulse) in the repeller. Ions (+) are mass selected according to their flight time through a drift region l and detected by an MCP. A linear TOF configuration is chosen to improve the collection intensity at the price of a loss in the mass resolution $m/\Delta m$.

1.3.1.4 Experimental realization of TOF-MS

We typically tested the efficiency of our laser desorption source in combination with single photon post-ionization detection with samples of tryptophan ($C_{11}H_{12}N_2O_2$), the most massive (204 u) among the standard 21 amino acids. Tryptophan is characterized by a melting point of 290°C but, like the majority of biologically relevant molecules, tends to fragment after evaporation. The distinguishing structural characteristic of tryptophan is that it contains an indole functional group which determines its optical absorption properties in the UV region.

Tryptophan is often considered a workbench molecule in gas phase mass spectroscopy since its mass spectrum and its fragmentation paths are well known. Furthermore, our attention to tryptophan was originally motivated by the fact that it has been often suggested that it might be exploited as an aromatic tag for bigger molecules [EMC⁺06, HEC⁺06]. According to this idea, each tryptophan could act as a single chromophore and could help by lowering the ionization potential of more complex, tagged molecules.

The ionization potential of tryptophan lies around 7.3 ± 0.2 eV [WJCN⁺06]. Molecular samples composed of β -carotene (536 u) and gramicidin A (1884 u) powders were also used for calibrating the TOF-MS⁷ setup.

The working principle of a time-of-flight mass spectrometer (TOF-MS) is rather simple: once molecules are ionized in a region of space (*repeller*)

⁷Kaesdorf, Munich - $m/\Delta m \simeq 100$.

with linear dimension s , a constant electric field E is applied so that an ionized molecule with charge Ze experiences the kinetic energy $ZeEs$. Ions then access a field-free drift region of length l where an electrostatic einzel lens additionally collimate and focus the ion beam onto a multi-channel plate detector (MCP). Molecules are discriminated by the flight time through the drift region according to the relation

$$\frac{1}{2}mv^2 = ZeEs \implies v = \sqrt{\frac{2ZeEs}{m}} \quad (1.27)$$

From the flight time $t = l/v$ we can thus express the mass-to-charge ratio as

$$\frac{m}{Z} = 2eEs \left(\frac{t}{l}\right)^2 \quad (1.28)$$

In our experimental setup, single photo-ionization of tryptophan is conventionally achieved by making use of the 157 nm (7.9 eV) wavelength of a F₂ excimer laser⁸ with a pulse time of 5 ns and beam energy up to 3 mJ per pulse. The laser is focused to a sub-millimeter spot in the center of the repeller.

A typical velocity distribution achieved with our laser desorption source is shown in figure 1.6 and it is obtained by varying the time delay between the ionization pulse and the desorption laser. A fit with a Maxwell-Boltzmann velocity distribution (equation 1.25) provides an average velocity of $v \simeq 620$ m/s and a translational temperature as low as 70 K, indicating the efficiency of the jet cooling process. On the other side, the center velocity of the beam is significantly smaller than the one predicted by equation 1.21, where a maximal velocity of $v \simeq 1700$ m/s is expected for the supersonic expanding beam of a 2 bar helium seed gas. Our experimental data thus suggest that the molecular beam produced by our particular mixing channel is not purely supersonic. We assume that the difference in velocity might be related to the time spent by the desorbed molecule in the closed channel before accessing the vacuum. We recently found this dwell time to be important for the formation of large bio-molecular complexes in our source [MHU⁺08, MHS⁺09].

⁸Coherent Inc, Excistar.

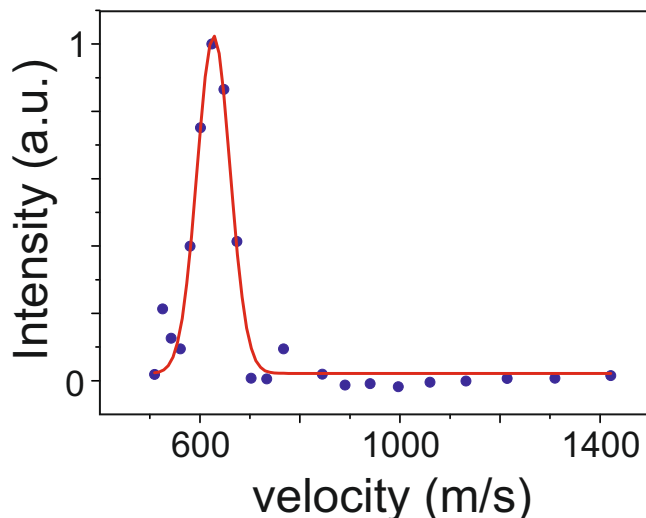


Figure 1.6: Velocity distribution of a laser desorbed (355 nm - 5 ns - 10 mJ) tryptophan beam embedded in a supersonic jet of helium (2 bar, 500 μ s). Neutral particles are detected by single photo-ionization (157 nm - 5 ns - 3 mJ) in combination with a linear TOF-MS. A most probable velocity centered around 620 m/s is observed.

1.3.2 Effusive beams generation

1.3.2.1 Experimental realization of a hyperthermal-beam

The operating principles of an effusive source and of supersonic expansions are here combined for the production of beams of C_{60} with a kinetic energy up to $\simeq 20$ eV.

As previously mentioned, our laser desorption source is able to produce intense beams of neutral particles but it causes molecular fragments as well as the generation of large mass complexes. While with a TOF-MS setup these effects can be easily taken into account, the exploration of alternative detection schemes for neutral particles - like the superconducting based detector that will be introduced in the next chapter - requires the generation of beams with a well defined mass distribution. Furthermore, in order to explore the energetic response of the detector, we want to be able to vary the kinetic energy of the incoming particles over a significant range.

Therefore, the idea is to combine the well understood beam properties of a Knudsen cell with the high intensity achieved with supersonic expansions.

The oven is schematically illustrated in figure 1.7 and it is essentially

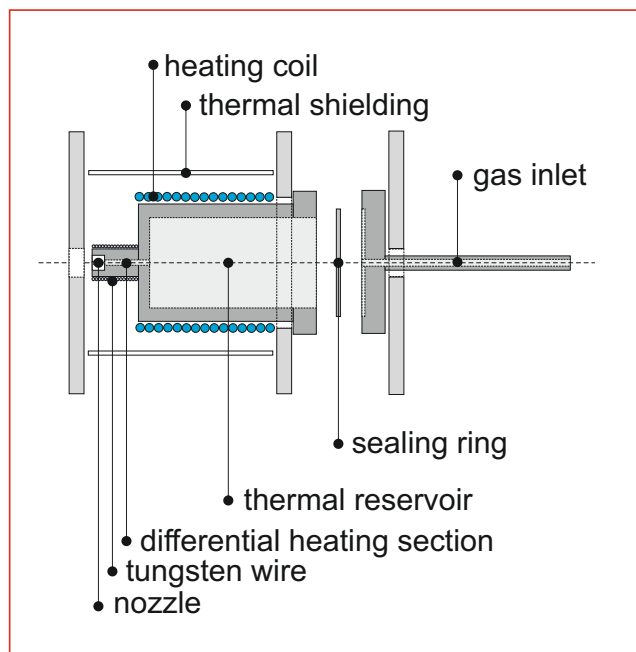


Figure 1.7: Schematic drawing of the hyperthermal-beam source assembly.

composed of two parts [KTB94]. The first part is a gas inlet where the seed gas pressure (helium - 2 bar) is applied. The gas inlet is screwed to the oven main body and the two parts are sealed by a silver ring. The oven body is entirely realized in molybdenum because of its high melting point ($\approx 2,600^{\circ}\text{C}$), its low thermal expansion coefficient and its relatively high thermal conductivity. The main body consists of a large thermal reservoir hosting the molecular sample and can be heated up to 800°C by a coaxial heating wire⁹ which is coiled around it. A $200\text{ }\mu\text{m}$ diameter boron nitride nozzle is fixed in the short extension of the oven. This small protrusion can be further heated by a 0.1 mm diameter tungsten filament. If the number of collisions experienced by a molecule during the expansion process through the small channel is high enough to guarantee the thermalization of the particle with the temperature of the wall, a suppletive amount of energy could in principle be pumped both in the translational and especially in the internal degrees of freedom of the molecule [BTK95]. The oven is finally shielded by a molybdenum foil in order to prevent any heat loss.

The source is able to operate both in an effusive and in a supersonic

⁹ISOMIL heating cable - type H - $76\text{ }\Omega/\text{m}$.

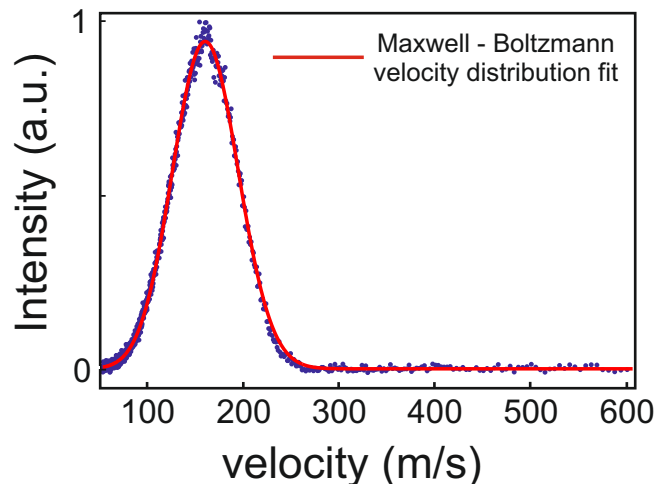


Figure 1.8: Velocity distribution of C_{60} achieved with the hyperthermal-beam source operating in effusive mode.

mode. By opening a manual valve we can easily switch from one mode to the other: while keeping the stagnation pressure of the seed gas fixed, we can regulate the amount of collisions in the cell by monitoring the pressure in the source chamber.

The molecular beam leaves the source chamber and enters a differential pumping stage chamber through a 1 mm opening skimmer. Here, the beam is first chopped by a mechanical rotating disk¹⁰ for the retrieval of its velocity distribution and later enters the detection chamber. Within this particular experimental setup, a continuous beam of single molecules is detected by a commercially available quadrupole mass spectrometer (QMS) whereas velocity distributions are collected by a computer time card whose acquisition starting time is triggered by the mechanical chopper. The overall distance flown by the molecules from the chopper to the detector is ≈ 1.35 m.

When operating in the effusive mode, the oven is functioning as a simple Knudsen cell, as illustrated by the velocity distribution shown in figure 1.8. The experimental data can be nicely fit by a shifted Maxwell-Boltzmann distribution (equation 1.25) centered at $v_0 \approx 140$ m/s and with a temperature $T \approx 110$ K. The velocity shift suggests the presence of an effective supersonic contribution as further illustrated by the fact that the

¹⁰10 cm diameter disk - 2 mm opening slit rotating at 25 Hz.

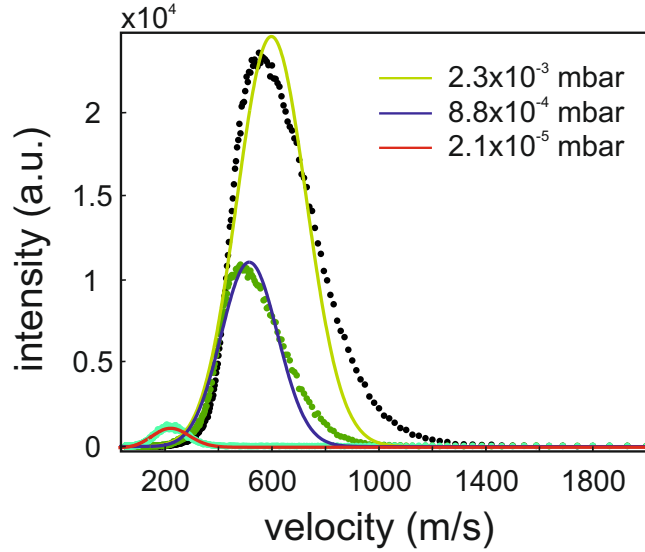


Figure 1.9: By increasing the seed gas pressure of the hyperthermal beam source, the intensity and the range of the velocity distribution can be varied. The number of collisions in the oven cartridge is regulated by monitoring the pressure of the source chamber. The transition from effusive to supersonic beam is illustrated. Data refer to fullerene C_{60} . **red**: $v_0 \approx 190$ m/s, $T \approx 320$ K; **blue**: $v_0 \approx 470$ m/s, $T \approx 1060$ K; **green**: $v \approx 550$ m/s, $T \approx 1600$ K.

translational temperature is actually lower than the typical evaporation temperature of 520°C . This effect might be related to the fact that the mean free path of the molecules in the small oven extension could be of the same order of the nozzle diameter and collisional processes are therefore occurring.

The supersonic contribution can be controlled by regulating the amount of seed gas flowing through the thermal reservoir, i.e. by regulating the number of collisions occurring in the oven cartridge and monitoring the pressure of the source chamber. The effect is illustrated in figure 1.9 where the velocity distribution of the incoming beam is collected for three different final pressure values of the source chamber.

Data show that the mean velocity can be controlled from $v = 200$ m/s (red line) to $v = 550$ m/s (green line) by increasing the number of collision events and that the intensity of the beam can be increased by four orders of magnitude when switching to the supersonic expansion mode. We may also notice that the fast tail of the velocity distribution tends to significantly

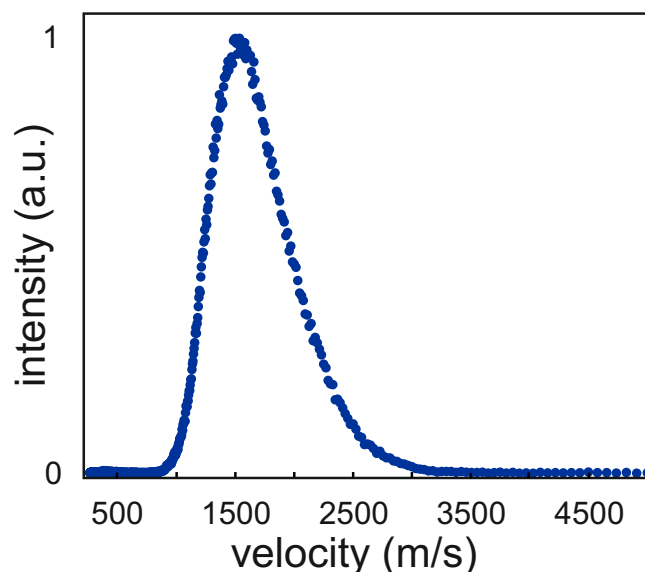


Figure 1.10: Fastest velocity distribution achieved for C_{60} with the hyperthermal-beam source operating in supersonic mode.

distance itself from a Maxwell-Boltzmann distribution for increasing pressures.

The highest velocity achieved so far is illustrated in figure 1.10 where a beam of fullerenes C_{60} with a velocity up to 2500 m/s is produced, corresponding to an equivalent kinetic energy of ≈ 25 eV.

1.4 Conclusions

The different beam sources described will be exploited in the next chapter for the characterization of a novel superconducting detector. For the sake of clarity, their main properties will be shortly listed.

- An **effusive source** allows the generation of beams of thermo-resistant molecules. The resulting beam is characterized by a thermal velocity distribution and a well defined mass distribution.
- **Laser desorption in combination with supersonic expanding gases** allows the introduction into the gas phase of thermo-labile species, e.g. organic molecules. This technique yields the production of an

intense beam of fast molecules, as well as the generation of molecular fragments or clusters.

- A **hyperthermal source** allows the production of both effusive and supersonic beams of single C_{60} particle with a kinetic energy up to $\simeq 25$ eV.

Part II

Superconducting single particle detector

Chapter 2

Superconducting nano-wire detector

2.1 Introduction

As previously stated in this thesis, the detection of single neutral molecules in the gas phase represents a basic requirement for matter-wave interferometry. A wide class of well established detection schemes for neutral molecules is nowadays available, including hyperthermal surface ionization, electron bombardment ionizers or photo-ionization processes [WDA03, Sco88]. However, all these detection methods rely on post-ionization mechanisms whose efficiency is often affected for particles beyond a few thousands atomic mass units. Moreover, post-ionization detection schemes often yield the activation of undesired fragmentation pathways if an excessive amount of energy is deposited into the target molecule.

Light induced photo-ionization counts among the softest ionization processes and its application to organic molecules has been recently extended up to 10,000 u [MHU⁺08, SSA⁺13]. Although no explicit mass limit is theoretically predicted, the ionization efficiency for particles beyond this mass range is dramatically reduced and the ionization process becomes rather challenging. It is often claimed that, due to the large number of rotational and vibrational degrees of freedom, the energy of an absorbed photon is either readily distributed or that the excited electron is not able to escape and simply recombines [BK95].

Alternative detection schemes have been recently proposed, such as the

microscope analysis of surface deposited samples [JTG⁺09] or the development of nano-mechanical cantilevers [NHH⁺09, CEM⁺12]. While these techniques represent promising solutions to the problem, they appear to be limited by striking experimental or technical difficulties such as a long acquisition time (of the order of some seconds for microscopy) or a low response time (of the order of tens of millisecond for the cantilevers).

In this chapter, I will present the experimental characterization of a superconducting nano-wire as a novel element for the detection of both neutral and ionized particles. The chapter is structured as follows: a brief history of cryogenic detectors is provided at the beginning in order to guide the reader to the idea of superconducting nano-wire detectors. Like most cryogenic detectors, our device was originally realized for the detection of single photons in the infrared band of the electromagnetic spectrum. Therefore, it was originally presented as a *superconducting single photon detector* or SSPD. A wide range of acronyms referring to the same experimental device can be found in literature. Here, I will stick to the acronym SSPD. In order to avoid any confusion, the reader will have to simply re-baptize the SSPD as a *superconducting single particle detector*. Finally, I will present the main experimental results achieved, i.e. the first proof-of-principle test for the detection of neutral nano-particles and a detailed characterization of the detector with low energy ions [MDS⁺09, SMMK⁺12].

2.2 Historical review

2.2.1 Cryogenic detectors to mass spectrometry

The development of MALDI and ESI techniques, i.e. the possibility of introducing into the gas phase an object with a mass up to a million atomic mass units, yielded the consequential need for increasing resolving power of mass analyzers [KH88, TWI⁺88, FMM⁺89]. Multi channel plates (MCP) are currently considered routine ion detectors for time-of-flight mass spectrometry experiments (TOF-MS) since they are large and easy to operate. At the same time, they are known to suffer from a considerable decrease in sensitivity when applied to the detection of large mass ionized species. MCPs rely on the collection of secondary electrons emitted upon the deposition of the kinetic energy of the incoming ion into its electronic system.

Since the number of emitted electrons scales with the amount of transferred energy, the process becomes inefficient as the molecular mass increases if the post-acceleration system stays identical.

Therefore, detectors relying on secondary ions emission have been suggested as a first potential alternative. Secondary ions are created by surface-induced dissociation or sputtering upon the impact of a primary ion onto a conversion electrode, further accelerated over a short distance and eventually detected with a conventional detector, such as a MCP. In this way *Berkenkamp et al.* managed to record the mass spectra of biological compounds up to 2 MDa [BMKH97].

Because of their high sensitivity, their low detection threshold and their energy resolving nature, cryogenic calorimetric detectors have been often tested in combination with TOF-MS experiments with bio-molecules with encouraging results. The main difference between cryogenic detectors and MCPs lies in the working principle: while MCPs rely on ionization or secondary electron emission, cryogenic detectors measure low energy solid state excitation, i.e. phonons. The phonon excitation energy in superconducting materials is as low as few meV and, for example, the deposition of 10 keV into the phonon system would result in a number of excitation as high as 10^5 . In addition, calorimetric detectors are intrinsically energetic resolving devices since the number of excitations created by a detection event scales proportionally to the deposited energy.

When applied to mass spectrometry, cryogenic devices appear to be characterized by three main, unique advantages [FLWB99]:

- As long as the deposited energy overcomes the detection threshold, cryogenic detectors are expected to detect large slow moving ions or neutral particles potentially with $\sim 100\%$ efficiency.
- Their intrinsic energy resolution may be used for charge-to-mass discrimination.
- The energy resolution could be exploited for the study of ion fragmentation mechanisms as well as for the characterization of the internal properties of a particle.

Probably, the easiest way to measure phonon excitations is to monitor the temperature rise of the detector. Therefore, the most elementary con-

ceivable cryogenic detector is a *bolometer*, i.e. an equilibrium¹ device which measures the heating power produced by a flux of particles impinging on its surface.

In the early 70's, *Cavallini* and co-workers retrieved the flux of a neutral molecular beam by making use of a commercially available semiconductor bolometer for IR radiation [CMSY71]. In their pioneering experiment, they reported the detection of a beam of noble gases with a doped germanium (Ge) bolometer operating at a temperature $T \sim 2$ K achieving a sensitivity of $\approx 10^7$ molecules per second. The bolometer was thus not sensitive to individual molecules, probably because the incoming energy of the molecules (~ 50 meV) was lower than the semi-conductor band gap (~ 1 eV).

Shortly afterwards, *Gallinaro et al.* explored the use of superconducting bolometers for the same purpose. By looking at the temperature-based change of the resistance of a superconducting tin (Sn) film, they achieved a detection limit for neutral particles in the thermal energy range down to 7×10^6 atoms per second with a microsecond acquisition time [GRT78]. In spite of the reported significant improvements, superconducting bolometers were essentially set aside since their operating temperature was severely limited by the sharp superconducting phase transition of the metal, requiring a thermal stabilization of the whole experimental setup.

A few years later *Bassi et al.* performed time-resolved laser spectroscopy of molecular beams with a superconducting tin bolometer. More exactly, they measured the kinetic energy distribution of the small molecule SF_6 while selecting its internal state with an infrared laser [BBSZ81].

The first MALDI-TOF-MS experiment with a cryogenic device was performed in 1996 only by *Twerenbold* and co-workers by replacing the sensitive element of their setup with a *superconducting tunnel junction* (STJ) [TVG⁺96]. STJs are non-equilibrium detectors whose detection mechanism relies on the measurement of a tunneling current and can be pictured as follows. A voltage is applied between two adjacent superconducting niobium (Nb) films which are divided by a thin Al_2O_3 layer acting as tunnel barrier. While the system is kept below its critical temperature T_c (9.2 K), the collision of an incoming ion results in the excitation of quasi-particles able to tunnel from a region to the other. Since the magnitude of the tunneling

¹Cryogenic detectors are classified as "equilibrium" ("non-equilibrium") devices if the phonon excitations are measured after (before) their thermal relaxation [FLWB99].

current pulse is proportional to the number of created quasi-particles, STJs qualify as energy sensitive detectors. They are typically characterized by a $200 \times 200 \mu\text{m}^2$ sensitive area, a millisecond repetition rate and a working temperature T as low as $0.1 \cdot T_c$.

2.2.2 SSPDs as particles detectors

For the sake of argument, let us shortly illustrate the working principle of SSPDs. A more rigorous theoretical description will be provided in section 2.3.1. A schematic picture of the process is provided in figure 2.4, where a photon is simply replaced by an impinging C_{60} molecule in order to make the reader more familiar with the idea that SSPDs will be used here as particle detectors.

The detector consists of a nanometer sized niobium nitride wire onto a sapphire surface. The wire is kept at a bath temperature T_b well below its critical temperature T_c and it is maintained in the *normal state* while biased with a current $I_b < I_c$. The absorption of a photon results in the creation of an excess of quasi-particles in a localized region referred to as the "*hot-spot*". Therefore, superconductivity is only locally suppressed while the nano-wire persists in its superconducting regime. As the region grows larger on a picosecond time scale due to electron-electron and electron-phonon interactions, the superconducting current is "expelled" from the hot spot and forced to flow on the external sides of the wire. As soon as the superconducting current density overcomes its critical value, superconductivity is suppressed and a resistive barrier is set over the whole cross section of the wire, driving the system in the *resistive state* and giving rise to a detectable voltage peak whose magnitude is related to the bias current. Due to thermalization processes, the quasi-particles concentration slowly decreases until the equilibrium value of Cooper pairs is reached and superconductivity is further restored.

Superconducting nano-wire detectors were first used in combination with mass spectrometry schemes by Suzuki *et al.* [SMS⁺08]. A 200 nm wide and 6.8 nm thick niobium nitride wire (NbN - $T_c=10\text{K}$) onto a MgO substrate with a $50 \times 50 \mu\text{m}^2$ sensitive area was used for the detection of a 17.5 kV ion beam of Angiotensin I and Bovine Serum Albumine (BSA). The detector showed a response time of low than 1 ns, suggesting its high potentiality as an ultra-fast ion detector for TOF-MS. The results confirmed

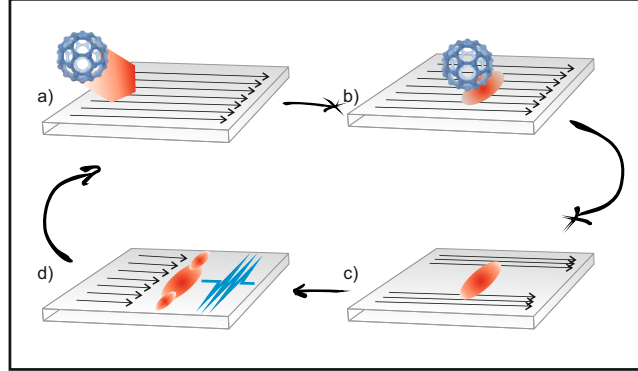


Figure 2.1: Representation of the hot spot formation: a) The film is kept at $T < T_c$ and biased with a current I_b ; b) The collision of a particle results in an energy transfer which creates a localized excess of quasi-particles (hot spot); c) Due to relaxation mechanisms, the hot spot tends to grow and the superconducting current is forced to flow on the side regions of the nano-wire; d) When the density of current overcomes its critical value, a resistive barrier is set throughout the wire and a voltage peak is measured as a detection event. Once Cooper pairs recombine on a ns time scale, the detector is brought back to its initial equilibrium state.

that this new class of detectors might actually be able to overcome at least two of the major drawbacks of conventional cryogenic detectors, namely the need for temperatures in the mK region and response times limited to few microseconds.

One year later, *Estey et al.* integrated for the first time a superconducting nano-wire with a commercial MALDI-TOF mass spectrometer and a closed cycle cryo-cooler, proving the efficiency of the detection mechanism with 25 keV ions up to 200 kDa [EBH⁺09]. In spite of the small detection area (ranging from 100 to 500 μm^2) the detector provided a spectral resolution comparable with a standard MCP. In 2010, *Rosticher et al.* implemented a 100 nm wide 500 μm long $\text{Nb}_{0.7}\text{Ti}_{0.3}\text{N}$ as a sensitive element for scanning electron microscopy, reporting the sensitivity of the device to single particles [RLM⁺10].

In recent years, the interest in this class of detectors has rapidly increased and the influence of different experimental parameters has been investigated such as the thickness of the film [CEZ⁺11]. Furthermore, experimental efforts have been made in the attempt to increase the detection area while keeping the response time of the detector down to the nanosecond time scale [CEE⁺12].

Nevertheless, no experimental effort had been made by the scientific community for testing the detection efficiency of SSPDs with neutral particle beams or ions at low kinetic energies (0.2-1 keV).

2.3 Superconducting nano-wires

2.3.1 Theory

The conceptual idea of the superconducting nano-wire detector dates back to the early 70's, when *Testardi* first observed that short laser pulses (514 nm - 6 μ sec at 5 W) were able to induce a resistive state in superconducting lead (Pb) films [Tes71]. The relevant aspect was that the transition to the normal conducting state was observed for thin samples only, i.e. for samples whose thickness ($d \sim 100$ Å) was comparable or smaller than the optical penetration depth of the metal and its superconducting coherence length. Moreover, the observed phenomenon could not be ascribed to thermal effects only since the response time of the system to the laser pulses was significantly shorter than the thermal time scale. The non-equilibrium nature of the process was corroborated and consequently attracted the attention of the solid state physics community.

Non-equilibrium phenomena in superconductivity are typically modeled by three components following the temporal dependence of the mutual interactions between Cooper pairs, quasi-particles² and phonons. Relaxation mechanisms towards equilibrium involve different processes that are usually described in terms of their characteristic time constants as follows:

τ_{e-e} : inelastic scattering of quasi-particles by electron-electron interactions,

τ_{e-p} : inelastic scattering of quasi-particles by electron-phonon interactions,

τ_B : phonon induced quasi-particles generation,

τ_R : Cooper pairs recombination mechanisms,

²A quasi-particle is a "broken" Cooper pair and it can be pictured as an electron and hole-like excitation [FLWB99].

τ_γ : phonon decay into the bulk system.

All these effects can be collectively monitored by following the temporal behavior of the superconducting order parameter³, the density of Cooper pairs and the quasi-particles' chemical potential. However, exact theoretical solutions are rather difficult and the problem is often approached by approximating the non-equilibrium state as a perturbation of the equilibrium, whereas large deviations from the equilibrium distributions are modeled by introducing effective chemical potentials and effective temperatures.

For example, the characteristic time constants of the photo-response can be extracted from a system of time-dependent differential equations where two different effective temperatures are associated to the non-equilibrium concentrations of phonons (T_p) and electrons (T_e) [SNG⁺95]:

$$c_e \frac{dT_e}{dt} = -\frac{c_e}{\tau_{e-p}}(T_e - T_p) + P(t), \quad (2.1)$$

$$c_p \frac{dT_p}{dt} = \frac{c_e}{\tau_{e-p}}(T_e - T_p) - \frac{c_p}{\tau_\gamma}(T_p - T_0). \quad (2.2)$$

Here, c_e and c_p indicate respectively the electron and phonon specific heat, T_0 is the temperature of the system and $P(t)$ represents the temporal profile of the power of the radiation absorbed. The normal conducting (resistive) region created after the radiation absorption is often referred to as the "hot spot".

In 1996 *Kadin et al.* illustrated the hot spot formation mechanism and suggested for the first time that the localized heating of an ultrathin superconducting film could be employed as the operating principle of a new class of single photon detectors [KJ96]. If we consider a film with thickness d , thermal conductivity κ , heat capacity c and if we indicate with α the thermal boundary conductance between the superconducting film and the bulk substrate, the two-temperatures model (equations 2.1-2.2) can be approximated by a simple heat flow equation

$$cd \frac{\partial T}{\partial t} = \kappa d \nabla^2 T + \alpha(T_0 - T). \quad (2.3)$$

³Within the Ginzburg-Landau theory, superconductivity is described in term of the order parameter ϕ , whose physical meaning is given by $|\phi|^2$. This quantity is proportional to the density of superconducting electrons [Poo07].

Since the solution of equation 2.3 predicts a hot spot region with a typical dimension on the nanometer scale, the realization of superconducting films with a width comparable to the dimensions of the induced hot spot could be exploited as a novel class of single photon detectors.

The hot spot formation process was further investigated by *Semenov* and co-workers [SGK01]. They considered a superconducting film with a normal state diffusivity D and they assumed the thickness d to be smaller than the thermalization length, i.e.

$$d \ll L_{th} = \sqrt{D\tau_{th}},$$

where τ_{th} represents the electron thermalization time. The equilibrium properties of the system are defined by the bath temperature T , which is specified well below the superconducting critical value T_c of the metal. The critical current density j_c , the energy gap δ and the equilibrium concentration of unpaired electron C_0 are thus univocally determined.

According to this model, equation 2.3 can be re-written as a function of the non-equilibrium quasi-particles concentration $C(r, t)$ as

$$\frac{\partial C}{\partial t} = D \frac{1}{r} \left(\frac{\partial C}{\partial r} + r \frac{\partial^2 C}{\partial r^2} \right) + \frac{C - C_0}{\tau}, \quad (2.4)$$

where r is the distance from the point where the detection event takes place (in this case the adsorption of a photon) whereas the quasi-particles decay rate $1/\tau$ is given by the sum of two different contributions

$$\tau = \tau_{e-p} + (c_e/c_p)\tau_\gamma.$$

If we assume the diffusion and the thermalization mechanisms to be two independent processes and if we let $t = 0$ be the time at which a photon is absorbed,

$$C(r, t) = \frac{M(t)}{4\pi Dd} \frac{1}{t} \exp\left(-\frac{r^2}{4Dt}\right) \exp\left(-\frac{t}{\tau}\right) + C_0 \quad (2.5)$$

represents a solution of the diffusion equation 2.4 [SGK01]. $M(t)$ represents the *quantum yield* of the system, i.e. the maximum number of quasi-particles produced by a single absorption event. Its precise expression is given by the equation

$$M(t) = \frac{2}{\Delta \sqrt{(h\nu/\Delta - 1)^2 - 1}} \times \int_{\Delta}^{h\nu-\Delta} \frac{E - \Delta - \xi}{\xi + 4\Delta} \times \frac{E}{\sqrt{E^2 - \Delta^2}} dE, \quad (2.6)$$

with

$$\xi = \frac{E - \Delta}{\sqrt{(t(E - \Delta)^2 / \tau_{th} \Delta^2) + 1}}, \quad (2.7)$$

$h\nu$ is the energy of the absorbed photon, τ_{th} is again the electron thermalization time while Δ indicates the superconducting energy gap of the metal.

These equations will be useful later on (see section 2.7.4), when an experimental estimation of the hot spot radius will be provided.

Finally, in their work *Semenov et al.* emphasized how a detection event results from a *collaborative effect* of the bias current and the growing normal domain, stressing the role of *phase slippage centers*⁴ (PSC) in the detection process [SGK01]. Therefore, they suggested that the rising mechanism of a normal conducting region could be depicted as the overall contribution of two different parts:

- a central part composed of a normal resisting spot,
- the resistance arising from the penetration of the electric field into the superconductor at the boundary with the normal spot.

These effects become significant for values of the bias current close to the superconducting critical value and the authors stressed that a voltage pulse generated as a consequence of a PSC event can not be distinguished from the one associated to a real detection event.

2.3.2 An experimental approach

An elegant experimental approach to the investigation of the non-equilibrium process leading to the formation of the hot spot in superconducting nanowires was suggested by Bluzer and co-workers [Blu92]. Since the temporal profile of the output voltage peak is related to the time derivative of the kinetic inductance L_k of the system, the investigation of the *transient photo-impedance response* in Nb and YBCO samples allowed the extrapolation of useful insights on the non-equilibrium lifetime of the Cooper-pairs density. As schematically illustrated in figure 2.2, a positive value of the voltage

⁴According to the *Ginzburg-Landau theory*, a PSC is defined as a point where the order parameter of a superconducting system vanishes and its phase undergoes a jump equal to a multiple of 2π .

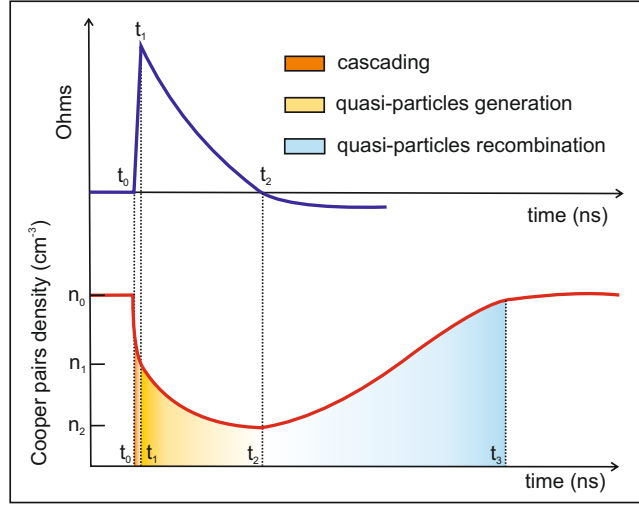


Figure 2.2: The temporal profile of a detection pulse provides qualitative information about the temporal evolution of the Cooper pairs density. The absorption of a photon at t_0 results in the generation of a quasi-particles concentration on a ps time scale (t_1). After t_1 , coupling to the electron subsystem leads to quasi-particles diffusion. Cooper pairs recombination takes place on a ns time scale (t_2). Illustration adapted from [Blu92].

output can be related to the generation of quasi-particles while a negative signal may be associated to the onset of recombination mechanisms.

The kinetic inductance⁵ is a physical property characterizing the mobility of charge carriers. In the superconductivity background, it provides a measurement of the inertial mass of the Cooper pairs and it is therefore related to the time needed for the perturbation of their state of motion. For a superconducting wire of length l and section A , the kinetic inductance can be expressed as

$$\frac{1}{2}(2mv^2)(n_s l A) = \frac{1}{2}L_k I^2$$

where n_s represents the Cooper pairs density, m the mass of a Cooper pair and v its average velocity. By inserting the expression for the superconducting current $I = 2en_s v A$, we obtain

$$L_k = \frac{m}{2n_s e^2} \frac{l}{A}.$$

The physical meaning of this relation can be understood as follows: since

⁵[http : //en.wikipedia.org/wiki/Kinetic – inductance](http://en.wikipedia.org/wiki/Kinetic_inductance) - last modified on 20 April 2013 at 12:38.

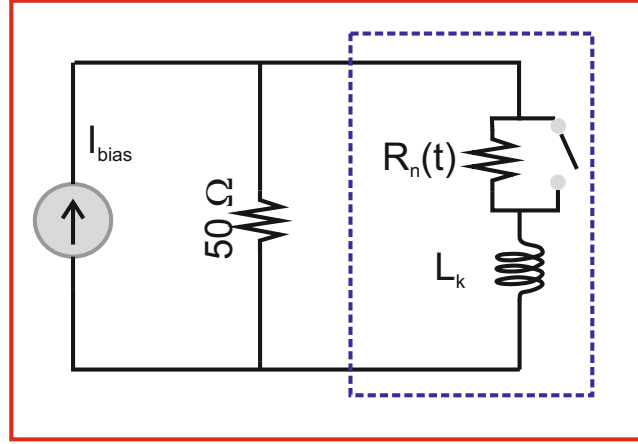


Figure 2.3: LR equivalent circuit for a superconducting nano-wire. The rise of a detection event can be pictured as the opening of a switch, setting a resistance through the whole wire. Illustration adapted from [NTH12].

the kinetic inductance of a superconducting system increases in inverse proportion to the density of Cooper pairs, the tribute we have to pay to the inertial state of the charge holders to bring them to the nominal bias current is higher when the number of particles is lower. In spite of its simplicity, this aspect is rather important when we want to answer some common technological questions related to the production of superconducting nano-wires, like what mechanisms limit the realization of thinner devices.

The behavior of a NbN nano-wire detector can be modeled in a simple way by an equivalent circuit, like the one illustrated in figure 2.3 [YKD⁺07]. A kinetic inductance L_k is connected in series with the parallel of a resistance R_n and a mechanical switch. The whole system is biased by a DC current and when the system lies in the superconducting equilibrium state the switch is closed. The rising of a detection event can be pictured as the opening of the switch, so that a resistance R_n is set through the whole wire. The current in the device decreases according to the time profile of a normal LR circuit, with a time constant $\tau_{fall} = L_k / (50 \Omega + R_n)$. Once thermalization takes place, the superconducting behavior of the wire is restored and the switch is closed letting the superconducting current increase up to the initial bias value with a rise time $\tau_{rise} = L_k / 50 \Omega$.

2.4 SSPD figure of merit

Since SSPDs were originally realized for the detection of IR photons, we will define the detection metric of our device starting from the one introduced in optics [NTH12]. This is a useful exercise since it gives us the opportunity to stress further the differences between photons and particles detection.

The most natural *figure of merit* for the characterization of the detection properties is represented by the detection efficiency η , viz. the probability that a signal is registered when a detectable event occurs.

The overall detection efficiency can be thought as the product of different contributes

$$\eta_{\text{tot}} = \eta_{\text{coupling}} \times \eta_{\text{absorption}} \times \eta_{\text{registering}}.$$

The term η_{coupling} represents a measurement of the goodness of the coupling between the experimental system and the detection stage. Perhaps, a simple misalignment of the source is the most obvious example contributing to this parameter. From now on, we will assume that this term will be optimized in all experimental sessions and we will therefore implicitly assume $\eta_{\text{coupling}} = 1$.

The detector materials and geometry, like for example its thickness, width or meandering ratio, defines the $\eta_{\text{absorption}}$ of the detector, i.e. the probability that a photon is absorbed and not reflected by the surface. An equivalent parameter for the detection of a particle should ideally take into consideration all possible dissipation pathways that might affect the efficiency of the detection mechanism. In comparison with a photon, a molecule impinging on the detector surface may bounce backward, undergo a fragmentation process or redistribute its kinetic energy among its large number of degrees of freedom. In section 2.7.5 for example, I will discuss how the condensation of noble gases on the surface of the detector is able to considerably affect the detection efficiency of our SSPD chip. Let us therefore replace the term $\eta_{\text{absorption}}$ with $\eta_{\text{deposition}}$

$$\eta_{\text{absorption}} \Rightarrow \eta_{\text{deposition}}.$$

Finally, $\eta_{\text{registering}}$ accounts for the fact that not all detectable events will be counted with unit probability, as several experimental parameters may contribute in a limitation of the detector performance. For example, stray light photons or electronic noise could be able to mimic the detection process and will therefore indicated as *dark counts*.

The product

$$\eta_{\text{deposition}} \times \eta_{\text{registering}} = \eta_{\text{dde}}$$

defines the device detection efficiency and it is often referred to as the detector *quantum efficiency*.

2.5 SSPDs realization

All superconductor nano-wire detectors used in my experimental work were produced by the group of Prof. G. Goltsman at the Pedagogical State University of Moscow. A detailed description of the fabrication process can be found in [GSK⁺03]. In summary, a 4 nm thick niobium nitride (NbN) film is deposited on a sapphire substrate by DC reactive magnetron sputtering in a N₂ and Ar mixture. Direct electron beam lithography and reactive ion etching are used for the definition of the detector final geometry, i.e. a 100 nm wide superconducting film meandered on a 20 × 20 μm² area with a 50% filling factor. Finally, gold contacts are deposited by photolithography and wet etching.

The properties of a NbN superconducting film, i.e. its critical temperature T_c , superconducting transition width ΔT_c and critical current density j_c are listed in table 2.1. An electron scanning micrograph of the superconducting nano-wire is provided in figure 2.4.

<i>Property</i>	<i>Value</i>
T_c	10 – 11 K
ΔT_c	0.3 K
j_c	7×10^6 A/cm ²
<i>Width</i>	100 nm
<i>Thickness</i>	4 nm
<i>Repetition rate</i>	≈ 25 MHz

Table 2.1: NbN superconducting detector properties.

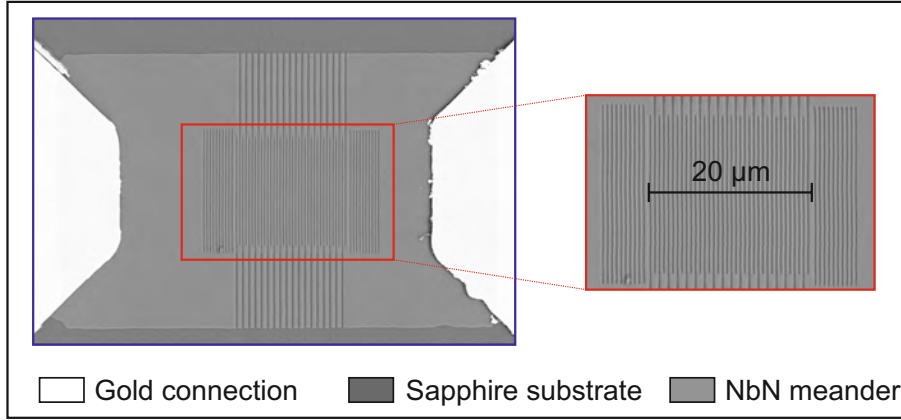


Figure 2.4: Scanning electron micrograph of our superconducting nanowire detector. A 100 nm wide, 4 nm thick NbN stripe is deposited onto a sapphire substrate with a 50 % filling factor covering a $20 \times 20 \mu\text{m}^2$ area.

2.6 Neutral particle detection

The experimental results presented in this section were already partially discussed in [Sc109] and published in [MDS⁺09].

2.6.1 Experimental setup

The experimental setup dedicated to the exploration of the superconducting nano-wire for the detection of neutral beams is schematically illustrated in figure 2.5. A beam of neutral particles is produced by a laser desorption source (for details see Chapter 1 - section 1.3.1.2). The light pulses of a Nd:Yag laser ($\lambda = 355 \text{ nm}$, $\tau = 5 \text{ ns}$, $E = 6\text{-}10 \text{ mJ}$) are focused onto a molecular target for the introduction into the gas phase of different organic compounds. Laser desorbed molecules are cooled by a supersonically expanding jet of helium and leave the mixing channel through a 1 mm opening into a vacuum pressure of $\sim 10^{-3} \text{ mbar}$. The molecular beam enters a differential pumping stage (10^{-6} mbar) through a 1 mm diameter skimmer and experiences a first filtering process. A $7.5 \mu\text{m}$ copper mesh hinders macroscopic dust grains that might be produced by the ablation process from reaching the detector chamber. The beam finally enters the detection chamber (10^{-7} mbar) through a 1 cm diameter opening. Here, the molecular beam is further filtered by a SiN grating with a periodicity of 266 nm and a 30% opening fraction. This second filtering stage further reduces

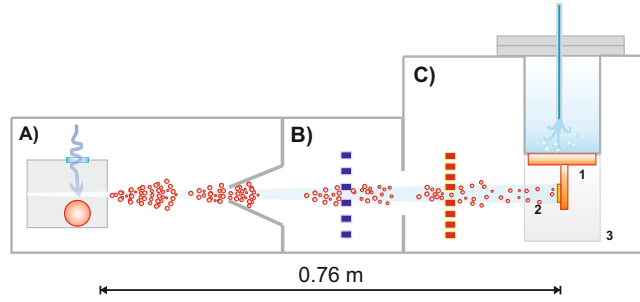


Figure 2.5: Schematic representation of the experimental setup for the detection of neutral particles. A: The source chamber (10^{-3} mbar) hosts the laser desorption source (see figure 1.3); B: A $7.5 \mu\text{m}$ opening copper mesh is placed in a differential pumping stage (10^{-6} mbar) for beam filtering; C: The molecular beam is further filtered in the detector chamber (10^{-7} mbar) by a 90 nm openings SiN grating. The SSPD detector (2) is mounted on a copper structure in close thermal contact with a liquid helium bath (1) and shielded from stray-light photons and thermal fluctuations (3).

the size of the transmitted particles to those of a genuine nano-particle and allows the extension of the lifetime of the detector which was otherwise strongly affected by the accumulation of molecular material. The average lifetime of a single chip was actually limited to few hours until we observed that the deposition of a thick molecular layer on the detector surface made it completely insensitive.

2.6.2 Device readout

The device readout system is illustrated in figure 2.6: a bias voltage is applied to the low frequency port of a bias tee, driving the superconducting nano-wire detector in the normal state. When the device switches to the resistive state, the signal is first sent through a RF output, amplified by 20 dB and finally monitored on an oscilloscope.

The output signal is coupled to a voltage discriminator followed by an analog to digital converter. TTL pulses are then sent to a personal computer, where a counting card registers the arrival time distribution of the detection events.

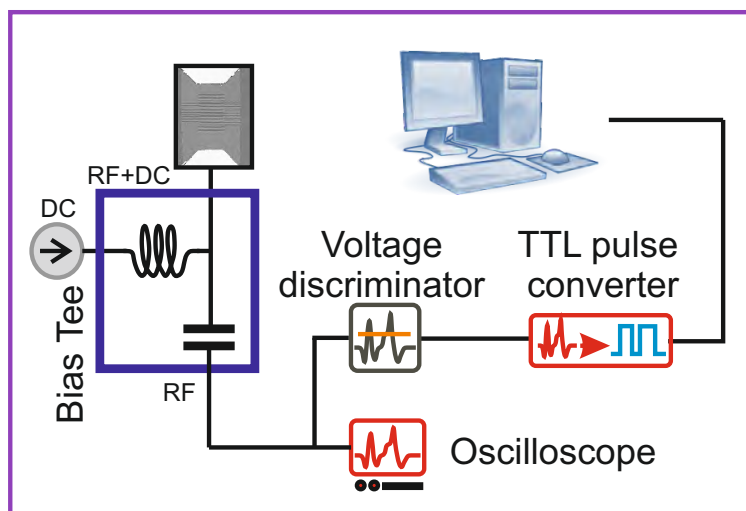


Figure 2.6: Schematic representation of the electronic read out.

2.6.3 First demonstration of neutral particle detection

Data shown in figure 2.7 represent the first experimental demonstration of the detection of neutral particles with a superconducting nano-wire device. The laser desorption pulse (orange line - upper panel) provides the trigger for the recording of the detection voltage pulses (blue line). The sample composition used for this first proof-of-principle test is listed in table 2.2. We admixed molecules over a large mass range in order to test the detector sensitivity. The same experimental setup was previously used in combination with a conventional superconducting bolometer that did not provide any detectable events and will therefore not be discussed. The signal is recorded while the device is biased with a DC current $I_b \sim 0.88 I_c$ with $I_c = 22 \mu\text{A}$. The bottom part of figure 2.7 provides a high resolution image of a voltage pulse associated to a single detection event. The pulse is characterized by a ~ 1 ns rising time and by a ~ 7 ns exponential decay.

In spite of their "roughness", the data shown in figure 2.7 allow us to support the hypothesis that single neutral particles can be detected:

First, we can exclude that the recorded signal might be attributed to ionized species: the experimental characterization of our laser desorption source confirms that no ionized particles are produced, as no signal has been ever registered when the ionization laser was switched off.

Second, the influence of the co-expanding seed gas can be easily tested

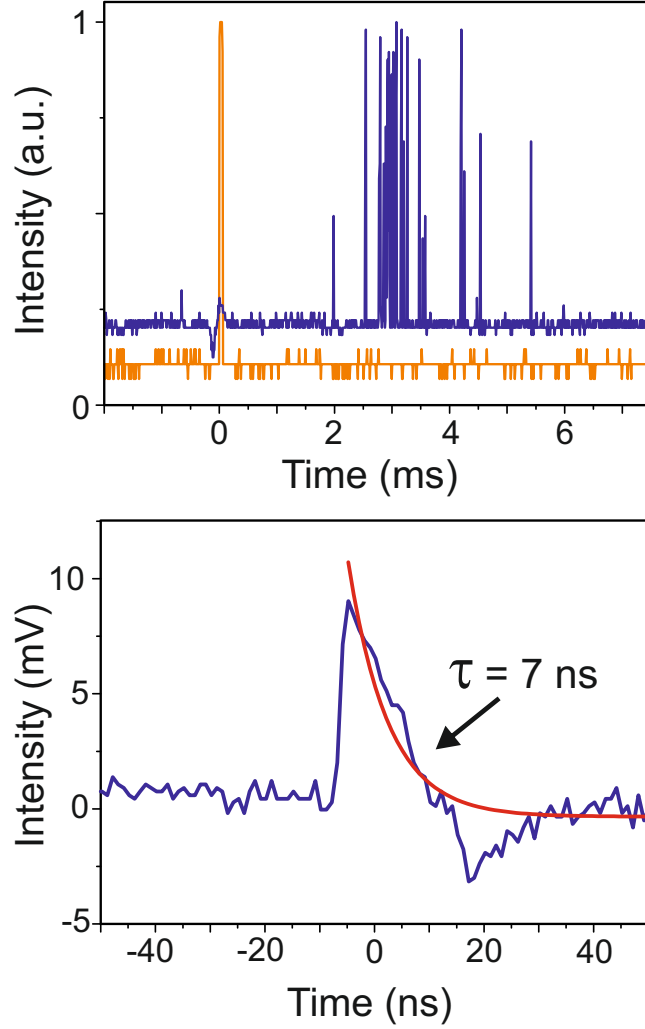


Figure 2.7: First experimental demonstration of neutral particles detection. Top: a "forest" of peaks (blue line) is observed roughly 2 ms after the laser desorption pulse (orange line). Bottom: A zoom into a single voltage peak reveals the time profile of a single detection event. A ps voltage rise is followed by an exponential decay with a characteristic time constant $\tau \simeq 7$ ns. Illustration adapted from [MDS⁺09].

<i>Molecule</i>	<i>Mass (u)</i>	<i>Amount (gr.)</i>
β -carotene	537	0.3
Insulin	$\sim 5,700$	0.3
Myoglobin	$\sim 17,000$	0.2
Bovine Serum Albumin	$\sim 66,000$	0.3
Cellulose	random	0.5

Table 2.2: Molecular test sample composition.

by simply switching off the desorption laser and letting a pure supersonic beam of noble gas reach the detector surface. The complete absence of any pulse indicates that the detector is not sensitive to single neutral helium atoms. The same statement holds for other noble gases such as neon, argon, krypton and xenon as well. Furthermore, this observation provides a first indication for the energy threshold of the detection process as the kinetic energy of the supersonic expanding gas produced by our source ranges from 25 meV for helium ($v \sim 800$ m/s) to 40 meV for the heaviest noble gas, namely xenon ($v \sim 250$ m/s).

Moreover, we can exclude any collective detection mechanism: in spite of the fact that the noble gas atoms are more abundant than the number of desorbed molecules, no signal was observed. The same conclusion holds for single massive particles: since their flux is even more dilute if compared to the jet gas, a collective effect is even less plausible.

Finally, we also exclude any background signal related to cellulose particles which are admixed to our molecular sample in order to improve its mechanical stabilization. Cellulose consists of linear chains $(C_6H_{10}O_5)_n$ in a random number n and its mass could therefore vary from few hundreds to thousands atomic mass units. Under the same experimental condition, laser desorption of a pure sample of cellulose was not able to provide any detectable effect.

2.6.4 Comparison with TOF-MS

In order to characterize the response of our superconducting device to beams of neutral particles, we collected the arrival time distributions of laser desorbed samples where only a single molecular species was present.

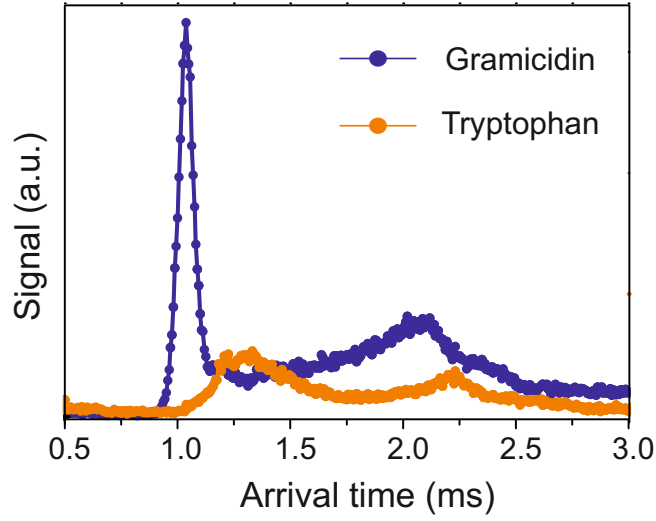


Figure 2.8: Arrival time distribution of laser desorbed tryptophan (orange) and gramicidin (blue) recorder with a SSPD ($I_b = 20 \mu\text{A}$). Illustration adapted from [MDS⁺09].

In particular, the choice of tryptophan and gramicidin allows a direct comparison with the results obtained with our conventional detection scheme, namely photo-ionization in combination with TOF-MS (see section 1.3.1.4). Similar measurements were also successfully performed with more complex and massive particles like insulin (5,700 u), myoglobin (17,000 u) and hemoglobin ($\sim 60,000$ u) for which the failure of photo-ionization does not allow the collection of any mass spectrum.

It is interesting to stress that all molecular sample showed the same arrival distribution profile: as shown in figures 2.8 and 2.9, a principal, intense peak can be easily identified around $t=1$ ms whereas a second broader peak arises around $t=2$ ms. It is important to state that all curves reported by the two figures were recorded under the same experimental conditions: the same $20 \times 20 \mu\text{m}^2$ detection area chip was used, the value for the bias current was fixed to $I_b = 20 \mu\text{A}$ and the level of the TTL discriminator was not modified.

At the same time, we may notice that the arrival time profile related to the tryptophan sample appears to be slightly delayed in comparison with the other curves. We attributed this difference to an accidental malfunctioning of the gas injection valve of the laser desorption source stage. A rather simple and convincing explanation is provided by the upper graph of figure 2.10: the arrival time of a gramicidin sample is here collected with

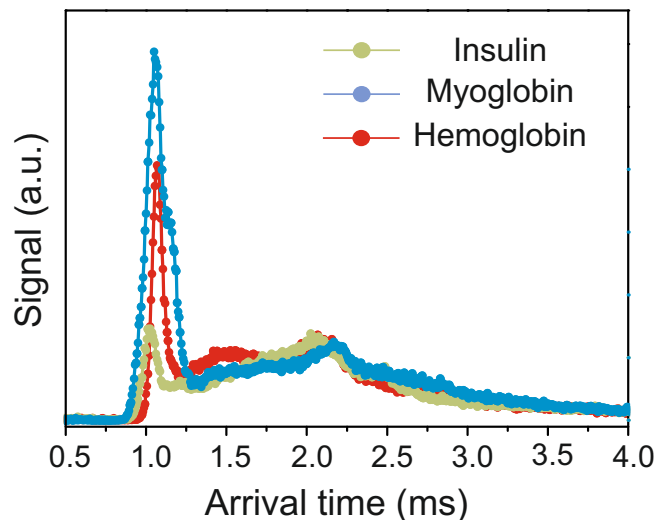


Figure 2.9: Arrival time distribution of laser desorbed insulin (green), myoglobin (blue) and hemoglobin (red) Recorded with a SSPD ($I_b = 20 \mu\text{A}$). Illustration adapted from [MDS⁺09].

a SSPD while varying the opening time of the injection valve of the laser desorption source. Data shown in figure 2.8 and 2.9 were both recorded with an opening time $t = 700 \mu\text{s}$, as the double peaks profile of the bottom graph of figure 2.10 (orange line) confirm. While for $600 \mu\text{sec}$ (red line) a single unshifted distribution is observed, a further reduction of the opening time down to $360 \mu\text{s}$ (blue line) results in a shifted double structure that is in good experimental agreement to the one reported for the tryptophan sample of figure 2.8 (orange circles). The double peak structure could be related to an undesired bouncing of the spring that regulate the valve opening.

Finally, figure 2.11 shows a typical arrival time distribution of a laser desorbed tryptophan sample collected with single photon ionization and a TOF-MS. The agreement of the experimental data collected with two different detection schemes strongly supports the idea that SSPDs could act as novel detectors for beams of neutral particles.

2.6.5 Open questions

After the first promising detection of neutral particles with SSPDs, a few questions were still left open. Due to the working principle of the su-

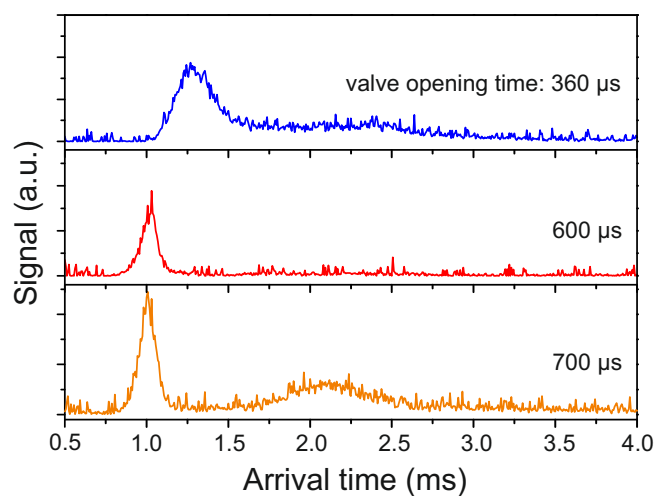


Figure 2.10: Influence of the injection valve opening time on the arrival time distribution profile. The double peaks profile of the bottom graph (orange line) can be related to a bouncing of the valve opening mechanism. Data refer to a gramicidin sample collected with an identical SSPD detector. Illustration adapted from [MDS⁺09].

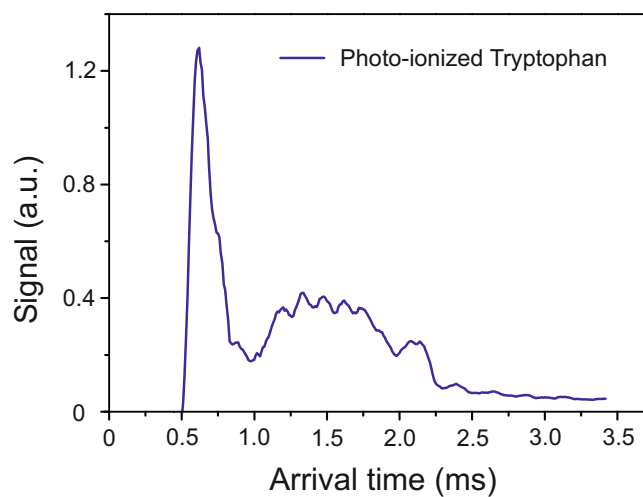


Figure 2.11: Arrival time distribution of a tryptophan beam produced by laser desorption and collected with single photon-ionization in combination with time-of-flight mass spectrometry (see figure 1.27). In comparison with figure 2.9, the peak of the arrival time distribution is centered on a shorter time. This is justified by the fact that the identical source was operated in combination with TOF-MS on a shorter experimental setup. Illustration adapted from [MDS⁺09].

perconducting nano-wire, no information about the mass of the incoming particles beam could be extracted. Therefore, while we can not be sure that the recorded signals were actually triggered by a single tryptophan or gramicidin molecule, we can not exclude that our laser desorption source is actually able to produce beams of large bio-molecules for which the photo-ionization process simply does not work.

According to this first experimental measurements, the energy threshold of the detection mechanism was cautiously placed above ≈ 300 meV, i.e. the kinetic energy associated to the slowest detected particle, namely a tryptophan molecule (204 u) reaching the detector ~ 2.2 ms after the desorption event, corresponding to the velocity $v = 345$ m/s.

The supersonic-oven described in section 1.3.2.1 has then been used for further characterizing the detection properties of SSPDS with neutral particles. As previously described, this molecular source matches some important experimental requirements like a reliable production of a beam of single molecules with a well defined mass, a tunable flux/intensity ratio and especially, the fact that by switching from the effusive to the supersonic mode we can vary the final velocity distribution over a wide energy range. In addition, the differential heating stage could, in principle, allow the control over the internal energy distribution of the molecule and the energy dependence of the detector sensitivity could be exploited for a first spectroscopy experiment.

Unfortunately, in spite of hard experimental work, no reliable, consistent results have been obtained. Although some data seemed to speak in favor of the detection of single fullerenes molecules, their interpretation still remains open as they were hardly reproducible. A potential hindering effect of the detector sensitivity, namely the condensation of gas adsorbates on the detector surface, will be described in the next section.

Instead, laser desorption experiments have been successfully reproduced, confirming the results published in [MHS⁺09]. The fact that the detector was not able to retrieve any data related to a beam of C₆₀ propagating with a velocity as high as 2,400 m/s suggested that the energy threshold is probably higher than previously proposed and may lay above ≈ 25 eV.

Finally, several experimental factors might have significantly hindered a successful detection. Perhaps, the most obvious one was represented by the fact that the lifetime of the detector was be strongly affected by the

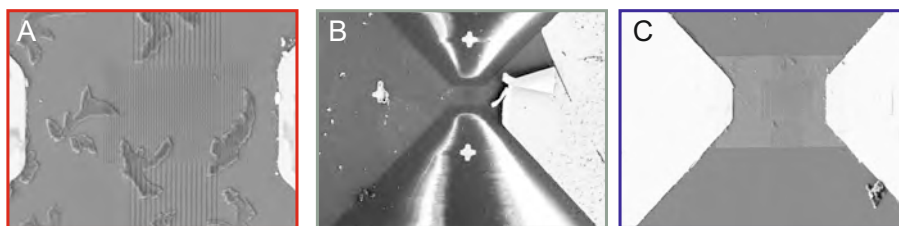


Figure 2.12: As the deposition of molecules on the detector surface (A) affects the lifetime of the detector, different cleaning schemes have been explored. While soft UV laser sputtering often results in a damage of the gold contacts (B), an acetone supersonic bath is able to restore the SSPD original conditions (C).

deposition of multiple layers of molecules on its surface, as shown in figure 2.12-A. Different tests have been performed focusing on the realization of a reliable *in situ* cleaning procedure in the attempt of minimizing the use of liquid helium and the experimental time related to the venting/pumping of the experimental apparatus. Local thermal heating of the wire through a dissipative Joule effect has shown to be inefficient due to the low resistance of the nano-wire. As illustrated by figure 2.12-B, soft UV laser sputtering was actually able to clean the detector surface but at the price of undesired desorption of the gold contacts. A simple sonic bath of acetone was the most effective experimental choice for the restoring of the initial surface conditions (figure 2.12-C).

2.7 Detection of single ions at low kinetic energy

2.7.1 Experimental setup

In order to better characterize the detection efficiency of SSPDs with particles, the experimental setup has been slightly modified as schematically illustrated in figure 2.13. The laser desorption source was replaced by a sputtering ion gun⁶ for the generation of single ionized single atoms produced by electrons bombardment. The beam flux can be tuned by controlling the current flowing through the hot filament, whereas the final kinetic energy can be selected by varying the extraction voltage of the source. We limited our investigation to the energy range between 0.2 and 1

⁶Specs - Ion source IQE 11/35.

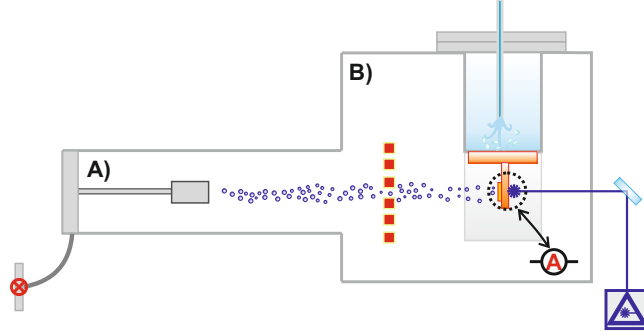


Figure 2.13: Schematic illustration of the experimental setup for the detection of low energetic ions. The ion beam is produced by a sputtering ion gun (A) and directed to the detection chamber (B) where the pressure is kept at 10^{-7} - 10^{-8} mbar. A wire mesh with a tuneable voltage V can be inserted in the beam direction for dark counts correction. The superconducting detector can be replaced by a Faraday-cup connected to an ammeter for calibration purpose. A 447 nm - 1W laser can be addressed on the back surface of the detector chip for the evaporation of helium adsorbates. Illustration adapted from [SMMK⁺12].

keV, i.e. the lowest energy interval for the source to guarantee good signal stability and reliability.

A wire mesh between the source and the detector allowed the discrimination of detection events related to particles and stray photons. By applying a voltage equal or larger than the extraction voltage of the ion gun, we observed a reduction of the signal and we were therefore able to correct the total number of collected events for the number of background counts, e.g. the number of events triggered by thermal photons emitted by the hot filament. Finally, the SSPD could be replaced by a simple Faraday cup⁷ for calibration purpose. By comparing the number of detected particles with the nominal value of gas particles reaching the detection area we could provide an absolute value for the detection efficiency.

Unless otherwise stated, all experimental data presented in this section have been corrected for background counts according to our definition of *absolute detection efficiency*

$$\eta = \frac{n_{SSPD} - n_{dark}}{f \times n_{FC}},$$

i.e. the ratio between the overall number of counts n_{SSPD} collected by the

⁷Kimball S66.

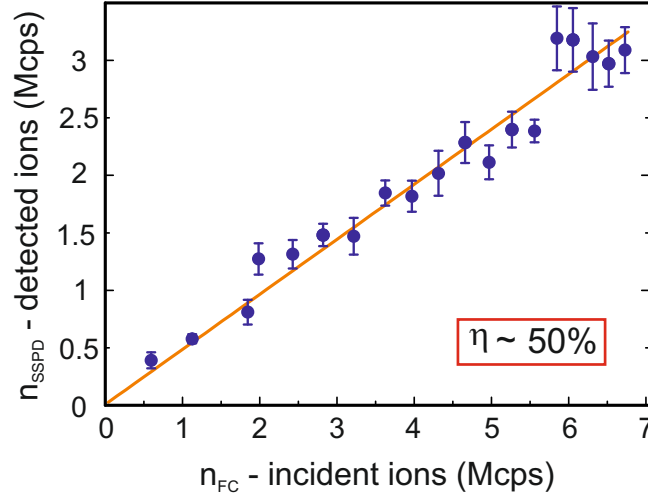


Figure 2.14: A linear relation between the number of detected events and the number of incoming particles confirms the SSPD sensitivity to single particles. Data (blue circles) refers to a 0.2 keV beam of helium. The linear fit (red line) confirms a $\sim 50\%$ detection within the selected experimental parameters ($I_b/I_c=0.5$).

SSPD corrected for the average number of dark counts n_{dark} and normalized with respect to the number of counts n_{FC} provided by the Faraday cup. The multiplication factor f is a simple geometric factor accounting for the filling factor of the SSPD and for the differences in the collection areas between the superconducting detector and the Faraday cup.

2.7.2 Single particle sensitivity

In order to confirm the sensitivity of SSPD to single particles and to exclude any collective effect, we measured the number of particles as a function of the nominal number of incoming ions. As previously showed, the recombination time of the nano-wire detector is $\simeq 7$ ns. On average, during the time window related to a single detection events (~ 10 ns) only 10^{-2} particles reach the detector and the incoming ion beam can be therefore considered as dilute. The linear fit (red line) of figure 2.14 can be interpreted as an experimental confirmation of the single particle sensitivity of the detector and the slope can be considered as an experimental measurement of the detection efficiency. The experimental data shown refer to a 0.2 keV helium beam and, under the experimental condition chosen ($I_b/I_c=0.5$), the detector shows a 50% detection efficiency.

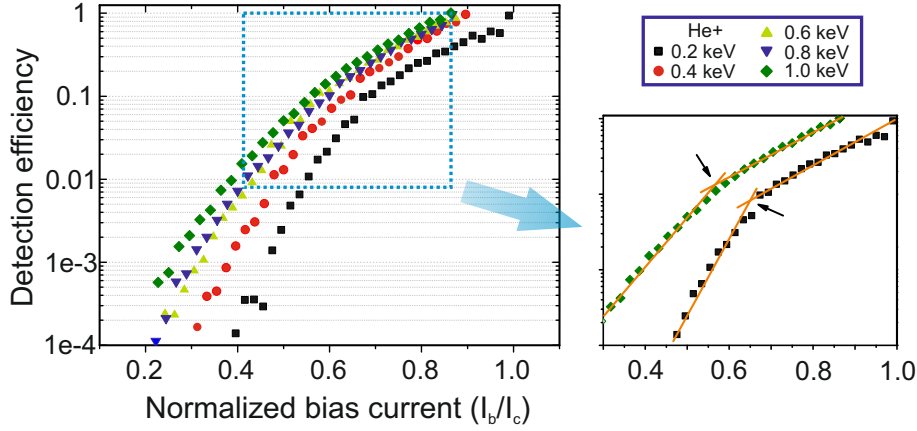


Figure 2.15: Detection efficiency vs. I_b/I_c . Data refer to a He^+ beam with different kinetic energies: 0.2 keV (black squares), 0.4 keV (red circles), 0.6 keV (yellow up-triangles), 0.8 keV (blue down-triangles), 1 keV (green diamonds). The identification of a kink bias current is highlighted in the small inset on the right side. Illustration adapted from [SMMK⁺12].

2.7.3 Energy sensitivity

The energy sensitivity of the superconducting nano-wire detector was investigated by monitoring the detection efficiency as a function of the kinetic energy of the incoming beam for different I_b/I_c ratios. In the following, I will limit the presentation of the experimental data to the detection of He^+ only, although measurements with heavier gases and the small molecule SF_6^+ have been performed as well. The energy dependence of the detection mechanism was confirmed by the fact that the same qualitative behavior was observed for all ionized species, independently of their mass.

Figure 2.15 shows the detection efficiency of the nano-wire superconducting detector in combination with He^+ beams when the kinetic energy was spanned over the range 0.2-1 keV while the bias current I_b was scanned up to the critical value I_c . All data were collected with the identical SSPD chip. The detector showed a sensitivity as low as 10^{-4} for small values of the bias current, whereas it reached a detection efficiency as high as $\eta \sim 100\%$ when the bias current was raised to the critical value ($I_b/I_c \sim 1$).

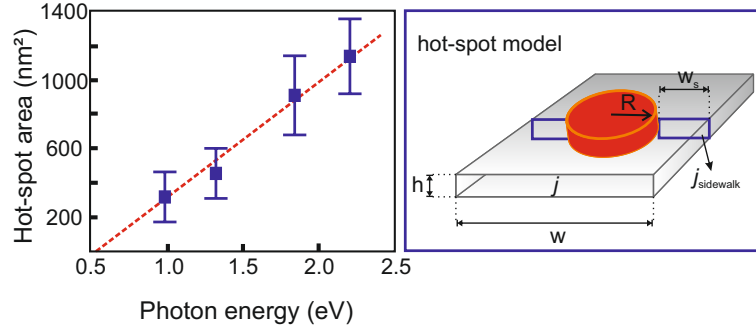


Figure 2.16: Left: Hot spot area vs. photon energy. Data are taken from [VZS⁺02]. Right: Illustration of the hot spot geometry for the physical interpretation of the kink bias current I_{kb} .

2.7.4 Hot-spot radius

A close inspection of the experimental data shown in figure 2.15 allows the identification of a turning-point behavior of the detection efficiency as a function of the normalized bias current. For a fixed value of the kinetic energy, the detection efficiency tends to increase in an exponential way up to a value of the ratio I_b/I_c where a different growing rate sets in. We will refer to this turning point as the *kink-bias current* I_{kb} . We notice that a lower value of I_{kb} is observed for higher values of the kinetic energy, in agreement with the hot-spot formation model.

The physical meaning of this turning point is still a matter of debate. In their work, Verevkin *et al.* suggested that the value I_{kb} could be associated with a change in the detector response mechanism [VZS⁺02]. While for relatively high bias currents it could be associated to the growth of a localized normal conducting region, in the low bias current regime the detection mechanism could be actually "assisted" by fluctuation-based mechanisms, such as phase slip centers or the formation and recombination of magnetic vortices formation and recombination. Therefore, they suggested that the value I_{kb} could be used for the estimation of the hot-spot radius R on the basis of a simple conservation model.

The model is illustrated on the right part of figure 2.16. Let us consider a superconducting stripe with thickness h , width w and cross section area $S = h \cdot w$. If the stripe is biased with a current I_b , the current density is given by

$$j_b = \frac{I_b}{S},$$

and the strip will persist in its superconducting state until

$$j_b < j_c = \frac{I_c}{S}.$$

Let us now consider a hot spot region with radius R , created by a detection event. The cross section area available for the superconducting current is now reduced to the value

$$S_{sw} = (w - 2R) \cdot h,$$

and the density of current is now accordingly given by

$$j_{sw} = \frac{I_b}{S_{sw}}.$$

The model assumes that the value I_{kb} represents the value of the bias current for which $j_c = j_{sw}$. Therefore, by equating these two quantities we get

$$R = \frac{w}{2} \left(1 - \frac{I_{kb}}{I_c} \right).$$

According to this model, our data would correspond to a hot spot radius varying between $R_{ion} = 18$ nm at 200 eV and $R_{ion} = 22$ nm at 1 keV. In spite of the large variation of the kinetic energy of the incoming beam, a relative increase of the associated hot spot radius as low as 20% is predicted. *Verevkin et al.* reported a variation of the hot spot radius as high as a factor 2 for a variation of the energy by 1 eV (see 2.17-left). Therefore, in comparison with the experimental data reported for the detection of photons, the energy transfer into the electronic system of the detector appears to be very inefficient for particles. In order to shed more light on this problem, we follow two different strategies.

Starting from equation 2.5, *Semenov et al.* calculate the theoretical values for the radius of the hot-spot [SGK01]:

$$R(t) = \sqrt{4Dt \ln \left(M(t) \frac{1}{4\pi D d (N_0 T_c - C_0)} \frac{e^{-t/\tau_e}}{t} \right)}. \quad (2.8)$$

Here, C_0 indicates the concentration of unpaired electrons when the system is kept at a temperature T_0 , whereas N_0 is the metal density of states at the Fermi level. Equation 2.8 is plotted in figure 2.17 where the theoretical

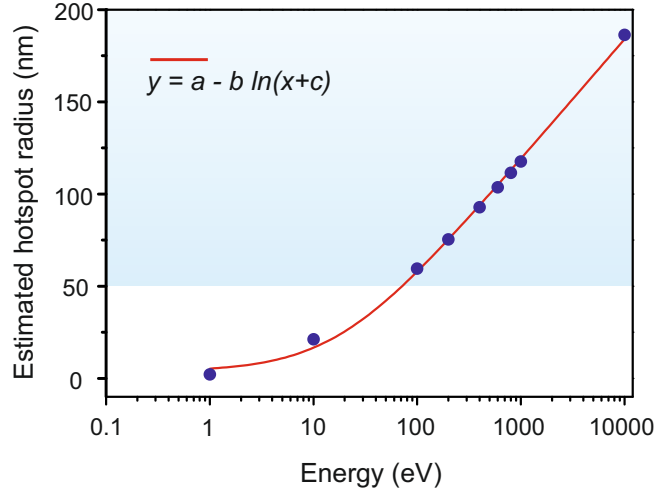


Figure 2.17: Hot spot radius vs. deposited energy. Data refer to a numerical simulation of equation 2.8. The blue area displays the range where the estimated hot-spot radius overcomes the width of our nano-wire (50 nm radius).

expectation of the hot spot radius is plotted as a function of the kinetic energy under the assumption that the whole energy is transferred into the electronic system of the detector. The parameters used for the simulation of the data are listed in table 2.3. A hot spot radius of ~ 75 nm is predicted for $E = 200$ eV whereas a radius $R > 100$ nm is expected for $E = 1$ keV.

Alternatively, we can push the analogy with the model proposed by Verevkin and co-workers: by fitting the experimental data reported for photons in [VZS⁺02] (figure 2.15-left), we can extrapolate the hot spot radius for a photon of energy $h\nu$ equal to the kinetic energy of our ions beam, $R_\gamma(h\nu = E_{ion})$. This extrapolation results in a radius $R_\gamma(0.2 \text{ keV}) = 210$ nm and $R_\gamma(1 \text{ keV}) = 470$ nm. Although both values exceed the physical dimensions of the nano-wire width, a large variation of the hot spot radius is predicted in both cases.

In order to quantify the different detector response to impacting particles and photons, we define the *conversion equivalence*

$$\chi = \frac{R_{ion}(E)}{R_{model}(E)}.$$

This parameter ranges between $\chi = 5\text{-}10\%$ when the experimental data of figure 2.15 are compared with those for photons, whereas it increases up to $\chi = 20\text{-}25\%$ when the hot spot radius is compared with the one predicted by

T_c (K)	D (cm^2s^{-1})	N_0 ($\text{m}^{-3}\text{K}^{-1}$)	τ_{th} (ps)	τ_e (ps)
11.7	0.45	5.2×10^{24}	7	17

Table 2.3: Physical parameters used for the simulation of equation 2.8 for the estimation of the hot-spot radius plotted in figure 2.17.

equation 2.8. In spite of these different values, both comparisons support the hypothesis that the transfer of kinetic energy of the impinging particle to the superconducting electronic system is rather inefficient.

2.7.5 Role of the surface adsorbates

The reasons for this incomplete energy transfer could be numerous. While photons directly couple to the detector electrons simply by absorption, complex particles might couple through different dissipation pathways. For instance, the impact of a massive particle onto the detector surface could lead to inelastic deformations through which the kinetic energy might be redistributed among the surface phonons.

A further dissipation channel could be related to the presence of rest gas adsorbates condensed on top of the detector surface. Even at a base pressure of 10^{-8} mbar, gas condensation could act as a "damping cushion" and provide undesired dissipation pathways⁸.

This idea is supported by the following observation. The data presented in figure 2.18 show how the sensitivity of our superconducting nano-wire is dramatically reduced when the surface conditions of the detector are varied by letting helium gradually condense on it. The residual helium pressure in the detector chamber was risen up to 10^{-5} mbar for a controlled amount of time while the ion gun was switched off. Once the pressure was restored to a base value of 10^{-7} mbar, the ion gun was switched on and the detection efficiency was monitored. The data refer to a 300 eV He^+ beam for a fixed value of I/I_c and show the relative detection efficiency as a function of the deposition time. We notice that the relative detection efficiency drops by almost three orders of magnitude with increasing values of the

⁸At room temperature and at a base pressure of 10^{-8} mbar, the monolayer formation time is of the order of $\simeq 6$ minutes for air [Jou08]

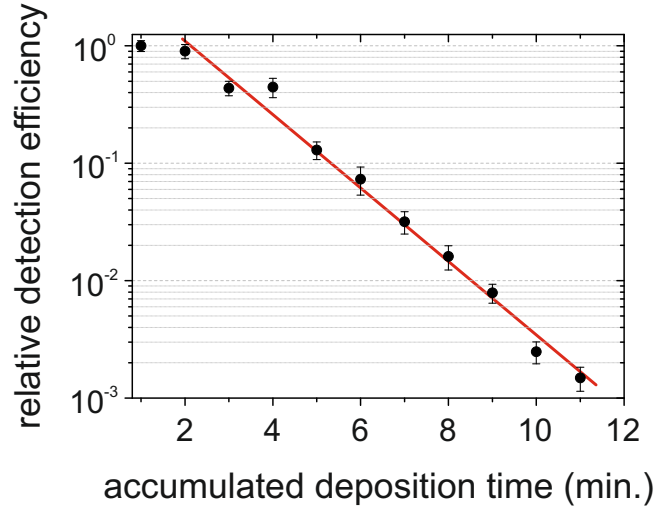


Figure 2.18: Detection efficiency vs. helium accumulation time. The condensation of helium onto the detector surface results in an exponential decrease (red line) of the detection efficiency. Illustration adapted from [SMMK⁺12].

accumulation time. The causal relation between the reduced sensitivity and the coverage of the detector surface was further corroborated by the fact that we were able to partially restore the original detection efficiency: by shining a laser (447 nm, 1W) onto the back-side of the sapphire SSPD substrate, we could evaporate the surface contaminations and regain up to a factor 100 in detection efficiency.

2.7.6 Future perspectives

Perhaps, the most appealing aspect for future applications of SSPDs to quantum and molecular physics is illustrated in figure 2.19, where the detection efficiency of the detector is plotted as a function of the extraction energy of the incoming helium beam for a fixed value of the ratio I_b/I_c . The inset shows how variations of the kinetic energy of the ion as low as a few eV can be lead to a relative increase of the detection efficiency by 50%. Therefore, we suggest that superconducting nano-wires might be able to retrieve energy variations in atomic or molecular beams.

If the internal energy of the impinging particle could be transferred to the electronic system of the device, the SSPD might be able to probe energy variations related to the internal degrees of freedom of a molecule. In that

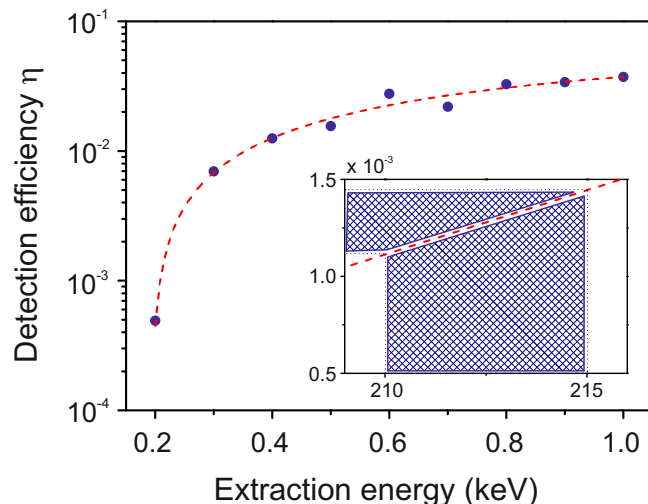


Figure 2.19: Detection efficiency vs. He^+ extraction energy. The small inset shows the variation of the detection efficiency in the region between 210 and 215 eV. Illustration adapted from [SMMK⁺12].

case, the detection efficiency profile could mimic the absorption spectra of a molecular beam.

At the same time, depletion spectroscopy would also be feasible. The embedding of organic molecules into helium nano-droplets has been described as a valuable tool for molecular spectroscopy, as the molecule can be cooled down to a temperature of a few hundred milli-kelvin. By triggering the evaporation of several hundreds helium atoms with photon absorption, we might be able to retrieve the variation of kinetic energy associated with the reduction of the mass of the flying molecule [TV04, PRD⁺09].

Further experimental tests of SSPDs with molecular beams are therefore not only highly desirable for a final, complete characterization of the energy threshold of the detection mechanism but they also represent promising investigation tools for molecular spectroscopy.

Part III

Molecular single-grating diffraction in the far-field

Chapter 3

Matter-wave fields

3.1 Introduction

From a conceptual point of view, far-field diffraction probably represents the most intuitive and simplest way of testing the quantum wave nature of massive particles. Since interference is a wave phenomenon, the appearance of interference fringes resulting from the propagation of a slow and collimated beam through a periodic structure can be considered as an unambiguous fingerprint of the spatial delocalization of the particle. For massive matter, the observation of diffraction fringes does not have any classical analog since it can not be explained by ray optics.

Because of its simplicity, far field interferometry has been exploited as a tool for testing coherent manipulation techniques with massive particles, e.g. holography [FMK⁺96, SF02] or microscopy [CSS⁺91, DGR⁺99, ERG⁺12]. At the same time, single-grating diffraction in the far-field has been used for the investigation of fundamental physics. For example, the wave behavior of complex molecules has been first demonstrated by recording the density distribution of the interference fringes of a collimated beam of C₆₀ propagating through a 100 nm SiN diffraction grating [ANVA⁺99]. Moreover, a far field setup allowed to report the existence of helium dimers and trimers as well as the investigation of the van der Waals interaction of atoms and diatomic molecules with material walls [GST⁺99, LKHC10, BFG⁺02].

Finally, far field interferometry in combination with single molecule fluorescence microscopy has recently served in visualizing the matter-wave dualism of phthalocyanine molecules in a beautiful and pedagogic

way, allowing the real-time observation of the build-up of the interference fringes [JMM⁺12].

In this chapter, I will shortly introduce the theoretical concepts which will be useful for the discussion of the results reported in the next chapter. A deeper insight on the introduced topics can be found in [Bor93, Rau00].

3.2 Theory

In quantum mechanics, the physical state of a particle in a potential $V(\mathbf{r}, t)$ is described by its wave-function $\psi(\mathbf{r}, t)$ whose time evolution is provided by the *Schrödinger equation*

$$\mathcal{H}\psi(\mathbf{r}, t) = \left(-\frac{\hbar^2}{2m} \nabla^2 + V(\mathbf{r}, t) \right) \psi(\mathbf{r}, t) = i\hbar \frac{\partial}{\partial t} \psi(\mathbf{r}, t). \quad (3.1)$$

According to classical optics, the propagation of an electromagnetic wave $\psi(\mathbf{r}, t)$ is provided by the *wave equation*

$$\nabla^2 \psi(\mathbf{r}, t) - \frac{1}{c^2} \frac{\partial^2}{\partial t^2} \psi(\mathbf{r}, t) = 0. \quad (3.2)$$

For a time independent potential $V(\mathbf{r}, t) = V(\mathbf{r})$ for all t , the plane wave *Ansatz*

$$\psi_k(\mathbf{r}, t) = \psi_k(\mathbf{r}) \cdot \exp(-i\omega t) \quad (3.3)$$

provides a solution for both equations. By combining the expression 3.3 with equations 3.1 and 3.2 we are left with the well known *Helmholtz equation*

$$\nabla^2 \psi_k(\mathbf{r}) + k^2 \psi_k(\mathbf{r}) = 0 \quad (3.4)$$

together with the following dispersion relations

$$k^2 = \frac{2m(E - V)}{\hbar^2} \quad \text{for matter-waves,} \quad (3.5)$$

$$k^2 = \frac{E^2}{\hbar^2 c^2} \quad \text{for e.m. waves.} \quad (3.6)$$

As the Helmholtz equation describes stationary solutions for *both* cases, electromagnetic waves and matter waves *have to* exhibit analogous physical phenomena in spite of the different nature of their interaction with the physical reality. The term *quantum optics* is therefore far from being a

metaphorical association and the strict analogy between quantum matter-waves and classical electro-magnetic fields can be further illustrated in a formal way by defining the index of refraction $n(x)$ for matter-waves fields.

If we consider a particle of mass m moving adiabatically through a region of space where it experiences a potential $V(\mathbf{r})$, stationary solutions can be derived from the time independent Schrödinger equation

$$-\frac{\hbar^2}{2m}\nabla^2\psi(\mathbf{r}) + V(\mathbf{r})\psi(\mathbf{r}) = E\psi(\mathbf{r}). \quad (3.7)$$

By making use of the plane wave Ansatz 3.3, we can derive the expression for the wave vector \mathbf{k} in the region of space where the molecule experiences the potential $V(\mathbf{r})$

$$k^2(\mathbf{r}) = \frac{2m}{\hbar^2} [E - V(\mathbf{r})]. \quad (3.8)$$

We define the index of refraction for matter-waves as the ratio of the spatially dependent wave-vector to the free space one [Rau00]:

$$n(\mathbf{r}) = \sqrt{1 - \frac{V(\mathbf{r})}{E}}. \quad (3.9)$$

Under a physical point of view, equation 3.9 tells us that the key for understanding the optical analog to matter-waves is related to the definition of the potential $V(\mathbf{r})$.

3.3 Kirchhoff's diffraction theory

Let us consider the problem illustrated in figure 3.1. We want to calculate the amplitude distribution of a scalar light field with amplitude A and wavelength λ propagating from a point source $P_0 = (x_0, y_0, z_0)$ to a point of the space $P = (x, y, z)$ placed behind a diffraction object \mathcal{A} . Let \mathbf{n} be the direction of the vector orthogonal to the plane of the diffraction object \mathcal{A} placed in the plane $z = 0$. We indicate with \mathbf{r} and \mathbf{s} the vectors of the points P and P_0 to a point $Q = (\xi, \eta)$ on the aperture plane \mathcal{A} , whereas we refer to their distances from the origin of the reference frame O_{xyz} respectively as r' and s' . We thus have

$$\left. \begin{aligned} r^2 &= (x_0 - \xi)^2 + (y_0 - \eta)^2 + z_0^2, \\ s^2 &= (x - \xi)^2 + (y - \eta)^2 + z^2, \end{aligned} \right\}$$

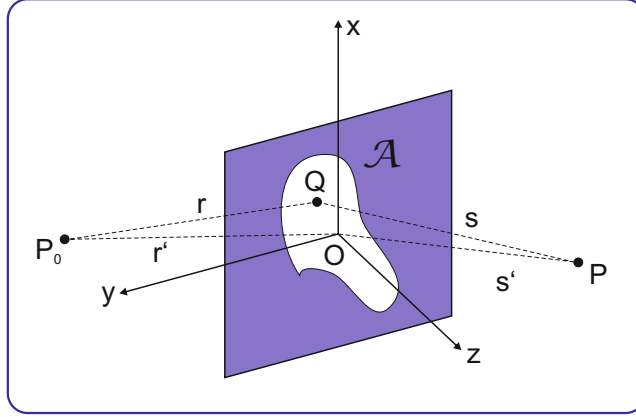


Figure 3.1: Light field propagating from a point source $P_0 = (x_0, y_0, z_0)$ to a point of the space $P = (x, y, z)$ through diffraction at an aperture \mathcal{A} . Illustration adapted from [Bor93].

and

$$\left. \begin{aligned} r'^2 &= x_0^2 + y_0^2 + z_0^2 \\ s'^2 &= x^2 + y^2 + z^2 \end{aligned} \right\}$$

According to the *Huygens-Fresnel principle*, the desired amplitude distribution is given by the *Fresnel-Kirchhoff diffraction integral* [Bor93]

$$U(P) = -\frac{Ai}{2\lambda} \iint_{\mathcal{A}} \frac{e^{i\mathbf{k}(\mathbf{r}+\mathbf{s})}}{rs} [\cos(\mathbf{n}, \mathbf{r}) - \cos(\mathbf{n}, \mathbf{s})] dS. \quad (3.10)$$

If the distances of the points P_0 and P from the screen are larger than the linear dimensions of the diffraction aperture \mathcal{A} , the factor

$$[\cos(\mathbf{n}, \mathbf{r}) - \cos(\mathbf{n}, \mathbf{s})]$$

can be approximated by a factor $2 \cos \delta$. Here, δ indicates the angle defined by the segment $\overline{PP_0}$ and the direction normal to the screen \mathbf{n} . At the same time, we can expand the distances r and s as a power series in ξ/r' , η/r' , ξ/s' and η/s' . The expression 3.10 then reduces to [Bor93]:

$$U(P) = -\frac{i \cos \delta A}{\lambda} \frac{e^{ik(r'+s')}}{r's'} \iint_{\mathcal{A}} e^{ikf(\xi, \eta)} d\xi d\eta \quad (3.11)$$

where

$$\begin{aligned} f(\xi, \eta) = & -\frac{x_0\xi + y_0\eta}{r'} - \frac{x\xi + y\eta}{s'} + \frac{\xi^2 + \eta^2}{2r'} + \\ & + \frac{\xi^2 + \eta^2}{2s'} - \frac{(x_0\xi + y_0\eta)^2}{r'^3} - \frac{(x\xi + y\eta)^2}{s'^3} \dots \end{aligned} \quad (3.12)$$

Neglecting the quadratic and higher terms in ξ and η in the relation 3.12 defines the *Fraunhofer* or *far-field approximation*. When this is not the case, we speak of *Fresnel* or *near-field diffraction*. From a physical point of view, the far field approximation consists in ignoring the curvature of the propagating front waves, i.e. the front waves reaching the observation point x are considered as *plane waves*.

3.3.1 Interference from a diffraction grating

Let us derive the intensity distribution arising from the illumination of a diffraction grating by a monochromatic wave ψ_0 emanated by a point source x_0 . As pictured in figure 3.2, the problem is simplified by the fact that we are dealing with a one-dimensional system.

A diffraction grating of periodicity d , opening width w and opening fraction $f = w/d$, can be described as a series of N single slits with a *transmission function*

$$t(x) = \sum_{n=0}^{N-1} t_s(x - nd), \quad (3.13)$$

where t_s represents the transmission function of a single slit and it is defined as

$$t_s(x - nd) = \theta(x) \cdot \theta(fd - x), \quad (3.14)$$

with $\theta(x)$ the Heaviside step function

$$\theta(x) = \begin{cases} 1 & \text{if } x \geq 0 \\ 0 & \text{if } x < 0. \end{cases}$$

According to equation , the diffraction amplitude observed at a point x on a screen can therefore be expressed as

$$\psi(x) \propto \int_{-Nd/2}^{Nd/2} t(\xi) \psi_0(\xi) d\xi \quad (3.15)$$

and the final intensity distribution is given by the very well known expression

$$I(x) = |\psi(x)|^2 \propto \left(\text{sinc} \frac{k_0 f dx}{2L_2} \right)^2 \left[\frac{\sin(Nk_0 dx/2L_2)}{\sin(k_0 dx/2L_2)} \right]^2, \quad (3.16)$$

where the *sinc* function is defined as $\text{sinc}(x) = (\sin x)/x$.

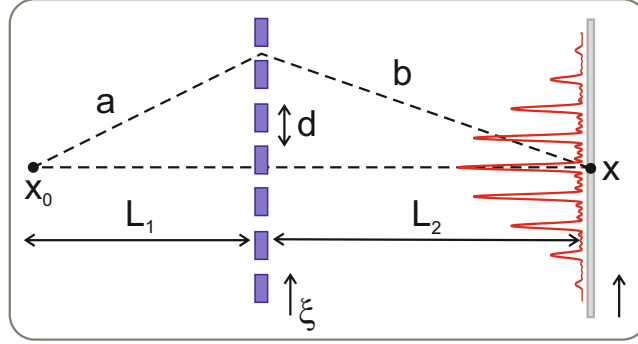


Figure 3.2: Interference pattern arising from the monochromatic illumination of a diffraction grating. The point source x_0 is placed at a distance L_1 from a grating with periodicity d . Diffracted intensities are collected at a distance L_2 behind the diffraction object.

If $\lambda = 2\pi/k_0$ denotes the wavelength of the diffracted wave, the maxima of the interference function 3.16 can be found according to the relation

$$\vartheta_n = n \frac{\lambda}{d} \quad \text{with } n \in \mathbb{Z}. \quad (3.17)$$

However, in real experiments we hardly handle point-like sources and monochromatic waves. Therefore, when we calculate the final intensity distribution, we may want to correct the expression 3.16 for the finite dimensions of the source \mathcal{S} and consider a propagating wave that is not strictly monochromatic. From a mathematical point of view, these considerations are equivalent to averaging the final intensity over the dimensions of the source and the momentum distribution $f(k_0)$ of the propagating wave:

$$I(x) \propto \int_{\mathcal{S}} dx_0 \cdot \int_{k_{\min}}^{k_{\max}} dk_0 \cdot f(k_0) |\psi(x_0, k_0)|^2. \quad (3.18)$$

Within the Fraunhofer approximation, the Fresnel-Kirchhoff diffraction integral 3.10 yields:

$$\psi(x) = \sum_n e^{-ik_0 \left[nd \left(\frac{x}{L_2} + \frac{x_0}{L_1} \right) - \frac{(nd)^2}{2L} \right]} \int d\xi t_s(\xi) e^{ik_0 \left[\frac{\xi}{2L} + \frac{nd}{L} \xi - \xi \left(\frac{x}{L_2} + \frac{x_0}{L_1} \right) \right]}, \quad (3.19)$$

where $L = L_1 L_2 / (L_1 + L_2)$ indicates the reduced distance.

We notice that the integral expression 3.19 depends only through the quantity

$$\left(\frac{x}{L_2} + \frac{x_0}{L_1} \right).$$

The effect of the real sizes of the source can be thus taken into account by considering the contribution of a point-like source at $x_0 = 0$ and by averaging $I(x)$ over each point x of the observation plane included in the interval $x \pm (L_2/L_1)\Delta x_0$, where Δx_0 indicates the linear dimensions of the source

$$I(x) \propto \int_{-\Delta x_0/2}^{\Delta x_0/2} dx_0 I\left(x + \frac{L_2}{L_1}\Delta x_0\right) \Big|_{x_0=0}. \quad (3.20)$$

Both the effects of extended and non-monochromatic source are illustrated in figures 3.3 and 3.4.

Figure 3.3 shows the influence of the dimensions of the source on the profile of the final interference pattern. Data refer to the simulation of an interference pattern arising from the diffraction of phthalocyanine (PcH_2) molecules (514 u) propagating with a velocity $v = 200$ m/s ($\lambda_{dB} \simeq 4$ pm) at a grating with periodicity $d = 100$ nm and opening fraction $f=0.5$. The simulated diffracted intensity is collected on a screen placed $\simeq 0.5$ m behind the diffracting object. The number of slits illuminated is here limited to $N = 5$.

In a similar way, figure 3.4 refers to the diffraction of the same wave through a grating whose opening fraction is reduced to $f=0.2$. For the sake of simplicity, we approximate the velocity distribution profile by a Gaussian function centered around the value $v = 200$ m/s. The role of different velocity selections $\Delta v/v$ is illustrated, where Δv refers to the standard deviation of the distribution function.

We notice that the effect of the finite size of the source results in a smearing of the interference peaks, whereas the width of the velocity class contributing to the diffraction pattern defines the number of distinguishable high order maxima. A velocity selection as low as 30% (red line - figure 3.4) results in a smeared amplitude and in a significant reduction of the visibility of the second and third order interference peaks.

These properties can be expressed in a more elegant mathematical way using the idea of *coherence* which will be the topic of the next section.

3.4 Some considerations about coherence

In a very elementary way, we could define the degree of coherence as "the capacity of two waves to interfere". The coherence length and the coher-

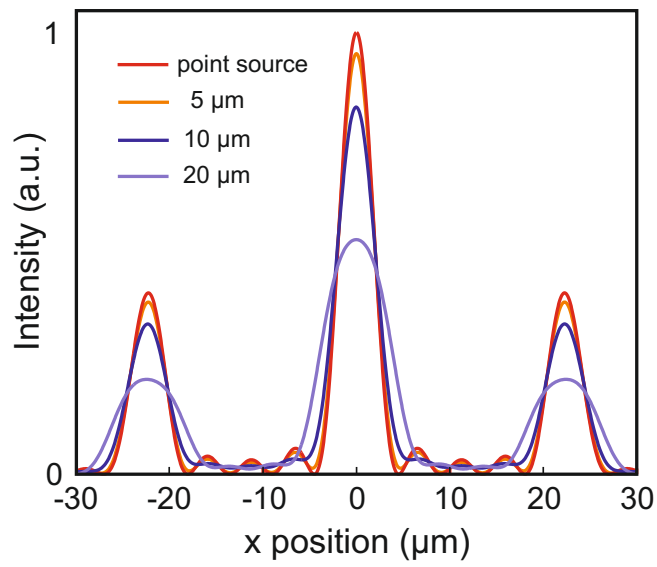


Figure 3.3: Effect of a finite source. Data refer to the simulation of the interference pattern of PcH_2 (514 u) with velocity $v=200$ m/s ($\lambda_{\text{dB}} \simeq 4$ pm) at a grating with periodicity $d=100$ nm and opening fraction $f=0.5$. The number of slits illuminated is limited to $N=5$, whereas the interference pattern is collected on a screen placed 0.5 m downstream. The simulation confirms that an increase of the source size results in a smearing of the interference peaks.

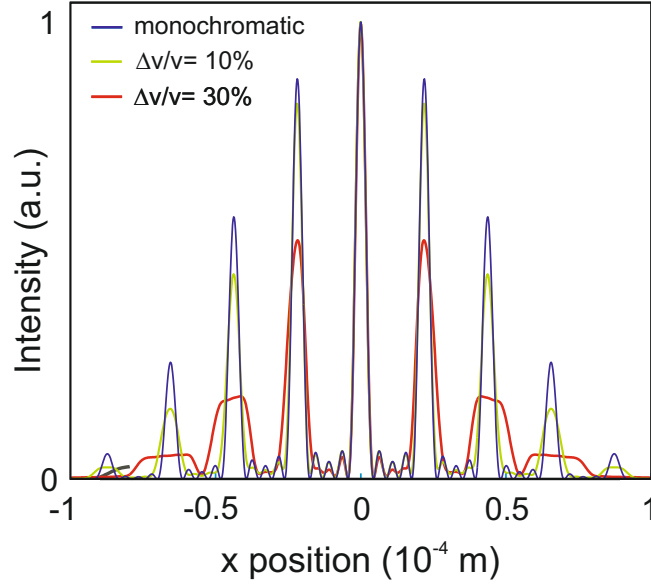


Figure 3.4: Effect of a non-monochromatic source. The simulation is performed with the same parameters used for figure 3.3. For the sake of argument, the opening fraction of the diffraction grating is here reduced to $f=0.2$. The width of the velocity class $\Delta v/v$ defines the number of distinguishable high order maxima.

ence time reflect the “degree of correlation” of both phase and amplitude oscillations of a wave-function within a certain space-time domain.

Since we are dealing with a molecular beam propagating along a specified direction, i.e. $v_{\parallel} \gg v_{\perp}$, we can naturally distinguish between a *longitudinal* and a *transversal* coherence.

The *longitudinal coherence length* identifies the spatial dimension of a well defined correlation for the phase and the amplitude of a propagating wave. If $\bar{\lambda}$ indicates the average wavelength, i.e. the wavelength associated to a particle propagating with an average velocity \bar{v} and a velocity spread Δv , the coherence length along the direction of motion is defined by the relation [Bor93]

$$\Delta l = \bar{\lambda} \frac{\bar{v}}{\Delta v} = \frac{(\bar{\lambda})^2}{\Delta \lambda} \quad (3.21)$$

and it expresses the degree of monochromaticity of the wave source.

The *transversal coherence length* describes the correlation of phase and amplitude oscillations between two points P_1 and P_2 of a screen illuminated by an extended quasi-monochromatic source. According to the *van Cittert-Zernike theorem*, in the limit of the Fraunhofer approximation (far-field), the

degree of coherence is given by the normalized Fourier transform of the spatial profile of the source.

For example, if we consider a circular source with radius R , the degree of coherence is expressed by an *Airy disk diffraction pattern*. Since almost 80% of the diffracted intensity fall into the first Fresnel zone, we can assume the diffraction angle between the first two consecutive intensity fringes [Bor93]

$$\sin \vartheta = 1.22 \frac{\lambda}{R} \quad (3.22)$$

to be a good approximation for the transversal coherence angle.

Chapter 4

Far field interferometry

4.1 Introduction

The quantum wave nature of a massive particle can be illustrated with a matter-wave interferometer, i.e. an experimental apparatus where the coherent manipulation of the translational degrees of freedom of a molecular beam leads to the final recording of a diffraction pattern.

A successful interferometry experiment has to satisfy three basic requirements [CSP09]:

- *transversal coherent preparation*: the diffraction element has to be coherently illuminated by the wave associated to each incoming massive particle, i.e. a well-defined relative phase has to be imposed over the different position states of the molecule along the linear dimensions of the diffraction object.
- *coherent evolution*: the relative phase between the different position states of a particle has to be preserved until the molecule reaches the detection stage or, in other words, decoherence processes have to be prevented.
- *detection*: the information of the relative phase differences has to be retrieved in order to detect an interference pattern.

The experimental realization of our single-grating far-field diffraction setup is schematically sketched in figure 4.1. In order to prevent collisional decoherence, the whole apparatus is included in a set of chambers

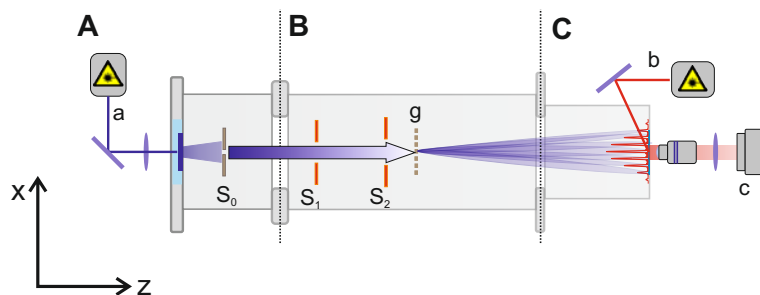


Figure 4.1: Single-grating diffraction in the far-field setup. A: isolated molecules are introduced into the gas phase by laser evaporation (a). The beam is collimated by a micrometer size vertical slit S_0 . B: The molecular beam enters the interferometer chamber where two slits S_1 and S_2 are used for the alignment of the system. Molecules are diffracted at a grating g and the interference pattern is finally deposited on a quartz plate ≈ 0.57 m downstream. C: Interference fringes are detected with epi-fluorescence microscopy. Molecules are excited by a laser beam (b) and fluorescence light is collected with a EMCCD camera (c).

where high vacuum conditions are reached. Three different stages can be identified.

The molecular beam is produced in the source chamber where molecules are laser evaporated into a vacuum of 2×10^{-8} mbar. A laser beam is focused onto a window which is coated with phthalocyanine (PcH_2 , 514 u). The beam can be collimated by a micrometer sized slit S_0 .

The molecules enter the interferometer chamber whose pressure is kept at 4×10^{-8} mbar. Two piezo slits S_1 and S_2 can be set with micrometer precision for the alignment of the molecular beam direction. A translational stage allows to shift the diffraction element g into the beam. The diffracted molecules are collected on a quartz plate 0.57 m downstream in the detection chamber at a pressure of 5×10^{-8} mbar. The interference fringes are finally imaged by a self-built epi-fluorescence microscope. In the following sections, a detailed description of each individual stage will be provided.

4.2 Molecular source

4.2.1 Laser evaporation

A detailed illustration of the source is provided in figure 4.2. The intensity of a 421 nm laser (100 mW, cw) is set by a rotatable polarizer and spatially filtered to a Gaussian beam profile. The mode cleaning stage consists of a 15 μm pinhole placed at the confocal point of two lenses with focal lengths $f_1=50$ mm and $f_2=30$ mm. The collimated beam is then guided to a 50x objective¹ whose role is twofold.

On the one hand, it tightly focuses the laser beam onto the window whose vacuum side has earlier been coated with the molecules. On the other hand, it collects the fluorescence light emitted by these molecules. This light is filtered by a dichroic mirror and focused by a tube lens onto a CMOS camera².

By fine-tuning the position of the second lens f_2 , the divergence of the evaporation laser can be altered giving us the possibility to tune the width of the desorption spot without changing the distance between the objective and the substrate. This is important to maintain optimum imaging conditions and to control the size of the laser spot, i.e. the width of the molecular source.

The coated window is sealed onto a bellows. The inclination of the window is aligned with respect to the direction of the laser beam so that the focus of the evaporation spot does not change over the whole region of interest. The bellows is mounted onto a motorized translation stage and scanned along the xy-direction in order to expose fresh molecules to the evaporation laser, whose position remains fixed.

A picture of the desorption process is provided in figure 4.2-A. The desorption laser (bright spot) is exposed over a molecular substrate (light grey zones) that is evaporated as a consequence of the local heating (dark grey lines).

In spite of its conceptual simplicity, the micro-evaporation laser source has many advantages in comparison to a conventional Knudsen cell:

- it can be switched on/off by blocking the laser beam with a mechanical shutter or even faster by controlling the laser diode current.

¹Zeiss LD EC "Epiplan-Neofluar" 50x/0,55 HD DIC M27.

²DCC1545M - High Resolution USB2.0 CMOS Camera, 1280 x 1024, Monochrome.

- the operation time can be effectively optimized and a single coated window guarantees up to 24 hours non-stop beam production.
- distinct portions of a single window can be coated with different molecular samples. We are therefore free to switch between beams of different molecular species by simply shifting the source position.
- by monitoring the evaporation process, we can reduce the size of the emission source down to the width of the laser waist. This improves the transversal coherence of the molecular beam (see section 4.2.2).
- the heating can be regulated by varying both the intensity and the exposure time of the laser. Our experiments were typically performed with a laser intensity of 1 MW/cm^2 , a source size of $4 \text{ }\mu\text{m}^2$ and a scanning speed of 1 mm/sec .

4.2.2 Coherence preparation

As the transversal coherence is given by the Fourier transform of the spatial profile of the source (see equation 3.22), in many quantum optics experiments with matter waves, a simple mechanical slit with a width of few micrometer is typically used for the coherent illumination of a diffraction object. In our experimental setup, we can choose between three different vertical slits which can be moved into the beam $\simeq 0.7 \text{ m}$ away from the diffraction object. The slits are mounted onto a linear translation stage and we can choose between the nominal width values $w = 1, 3 \text{ and } 5 \text{ }\mu\text{m}$.

A possible alternative is offered by directly reducing the dimension of the molecular source [PDEK06], i.e. down to sub-micron sizes. The insets B-C of figure 4.2 show how this can be implemented in our experimental setup. The evaporation profile of the desorbed molecular layers is here pictured by an optical microscope in figure 4.2-B and it can be fitted by a Gaussian function (4.2-C) with a $1.5 \text{ }\mu\text{m}$ waist resulting in a molecular source with an intrinsic $3 \text{ }\mu\text{rad}$ coherent illumination angle at the position of the diffraction object.

The spot size may be susceptible to fluctuations related to the instability of the laser intensity, misalignment of the system or irregularities of the coated surface. Therefore, for experiments where different diffraction objects are compared and high source uniformity is required, it is more

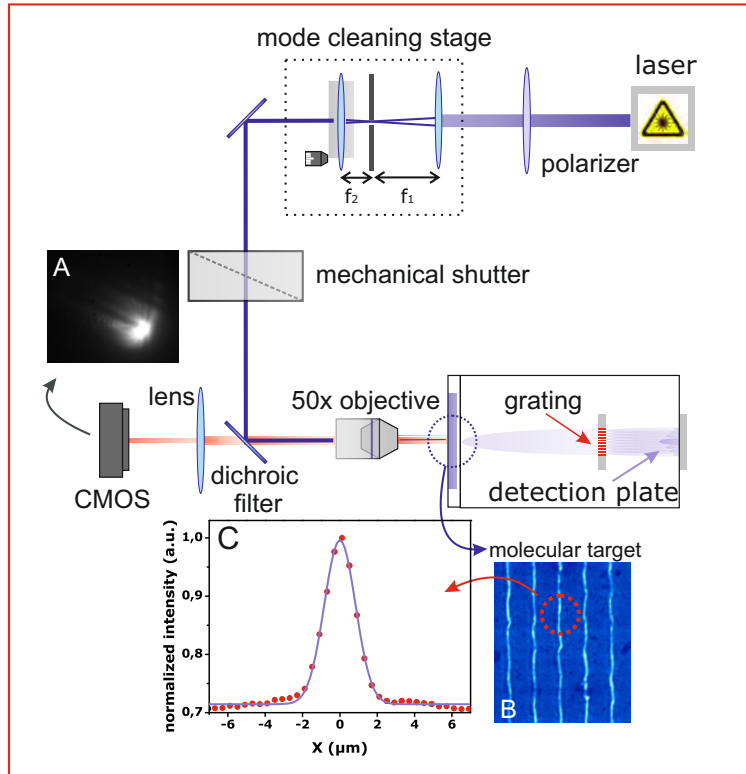


Figure 4.2: Illustration of the source stage. A laser beam (421 nm, 100 mW) is first shaped to a Gaussian profile within a mode cleaning stage ($f_1=50$ mm, $f_2=30$ mm) and further focused onto the molecular target (B) by a 50x objective. By tightly focusing the laser spot we can reduce the molecular source width to 1.5 μ (C) and produce a coherent beam of neutral particles with a velocity in the range $v=120$ - 350 m/s ($\lambda_{dB} = 2.2$ - 6.5 pm). Back-collection of fluorescence light allows the monitoring of the evaporation process on a CMOS camera (A). Illustration adapted from [SJK13].

reliable to operate the system with an additional collimation slit. The reduction of the beam flux can be counter-balanced by arbitrarily increasing the size of the evaporation spot.

4.3 Interferometer stage

The interferometer chamber hosts the diffraction object, two vertical alignment slits S_1 and S_2 and an horizontal velocity selection slit.

The alignment slits are realized by connecting two razor blades on a piezo-translation stage³ so that their width can be continuously varied from a maximum opening of 200 μm down to few micrometers.

A 10 μm horizontal slit is mounted onto a translation stage and it is placed in front of the diffraction grating. By regulating its position along the y-axis, we can control the velocity distribution contributing to the interference pattern.

4.3.1 Diffraction gratings

The diffraction gratings were made in the group of Prof. O. Cheshnovsky at the nano-fabrication center of the Tel Aviv University. They were written into SiN or carbon membranes by focused ions beam milling using 35 keV Gallium ions. All gratings have a nominal periodicity of $d=100$ nm. They are produced with different opening widths w and thickness t to explore the van der Waals interaction between the diffracted molecules and the grating wall (see 4.5.1). In addition, we used a SiN grating that had been fabricated by T. Savas at MIT, using photolithography and wet etching, more than 10 years ago.

The gratings are carefully aligned to gravity with milliradians precision. All grating properties⁴ are listed in table 4.1 and their geometry is sketched in figure 4.3.

³PiezosystemJena PZS1.

⁴the values of the wedge angle α were measured by scanning tunneling electron microscopy (STEM).

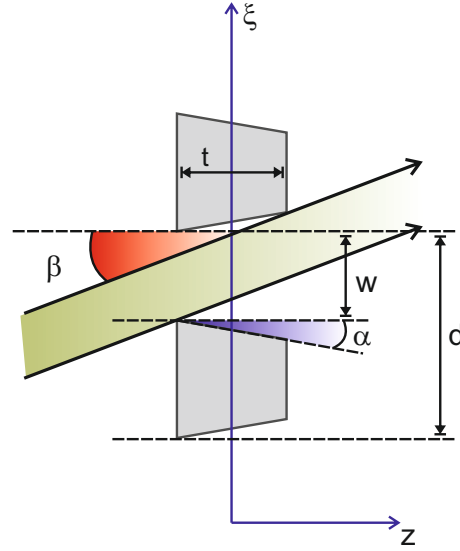


Figure 4.3: Illustration of the geometry of a grating with periodicity d and opening width w . Grating bars are characterized by their thickness t and wedge angle α . The relative orientation between the beam propagation and the grating surface is indicated with β . Illustration adapted from [CP04].

Name	Material	t (nm)	w (nm)	# of slits	α
G1	SiN	10	46	50	50
G2	SiN	46 ± 5	46	50	17
G3	SiN	10	79	30	33
G4	SiN	87 ± 9	57	$\sim 10^4$	10
G5	C	20	58	50	19

Table 4.1: Specification of the grating parameters used in our far-field interference experiments.

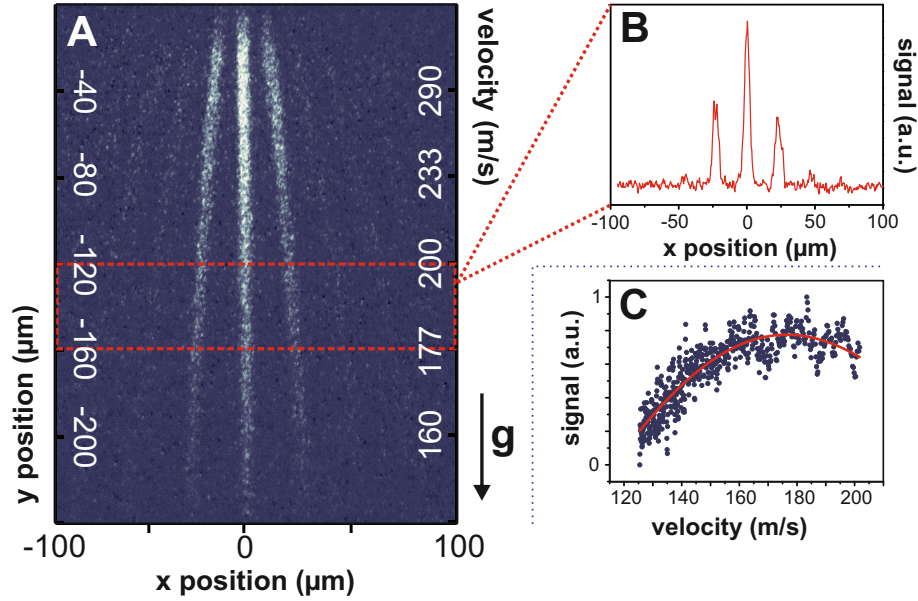


Figure 4.4: A: Far-field diffraction of PcH_2 with a 100 nm SiN grating, 79% opening fraction (G3). By evaluating the diffraction intensity profile at different deposition heights (B), we can retrieve the velocity distribution of the molecular beam (C).

4.3.2 Velocity selection

The molecules are promoted into the gas phase with a thermal velocity distribution, ranging from 120 to 350 m/s and they land on the detection quartz plate approximately after a 2 m flight while they fall in the earth's gravitational field. As a consequence, slow molecules will be deposited at the bottom of the quartz plate. This becomes apparent by looking at figure 4.4 and noting that the separation between the zero-th and the first order maxima increases for lower heights.

The average velocity of molecules at any given height y can be deduced by evaluating the distance between two consecutive maxima. In such a way we are left with a velocity distribution as a function of the height $v(y)$ whose exact behavior can be theoretically predicted from ballistic free flight:

$$v = \sqrt{\frac{g/2 \cdot (LL_1 - L^2)}{y_3 - y_0 - (y_1 - y_0) \cdot L/L_1}} = \sqrt{\frac{A}{y_3 - B'}} \quad (4.1)$$

where g represent the gravitational acceleration, L_1 is the distance between the source and the diffraction grating while L indicate the distance between

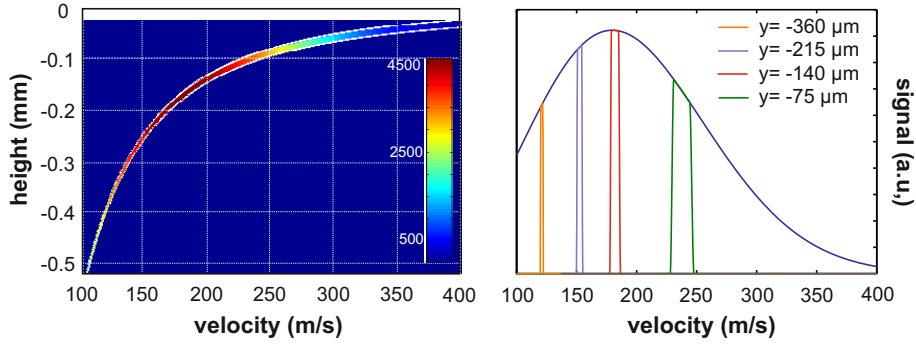


Figure 4.5: Left: numerical simulation of the velocity selection achieved with a 10 μm mechanical slit. Right: different heights relate to different velocity spreads $\Delta v/v$.

the source and the detection stage. The parameter A is thus defined by the geometry of the experiment, whereas the parameter B represents the height at which a molecule propagating along a straight line from the source to the detector would land on the quartz plate.

From the interference scan we can also extract the intensity distribution as a function of the height $I(y)$. $I(y)$ and $v(y)$ can be combined to derive the velocity distribution $I(v)$:

$$\int I(y)dy = \int I(v(y))\frac{dy}{dv}dv \propto \frac{I(v(y))}{v(y)^3}. \quad (4.2)$$

The diffraction grating are written on a 100 μm vertical structure. A 10 μm horizontal slit is inserted in the molecular beam direction shortly before the diffraction grating in order to select the velocity. This idea is simulated in figure 4.5 where equation 4.1 is calculated for a 10 μm wide velocity selection slit and a vertical source dimension of 1.5 μm .

4.4 Detection stage

In this section I will shortly review the theoretical principles of single molecule fluorescence spectroscopy. A wide literature dealing with the topic is available and we are mainly going to follow the framework suggested in [MF03, Gel06]. Finally, a detailed description of the experimental setup will be provided.

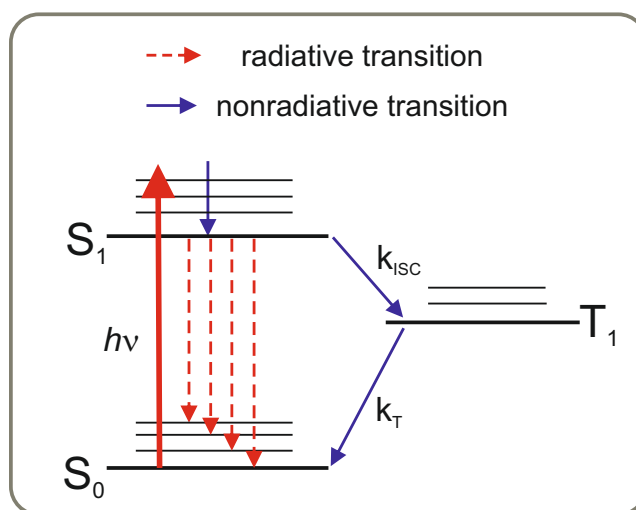


Figure 4.6: Illustration of a Jablonski diagram. A simplified energy level structure of a molecule is shown. Red arrows represent radiative processes whereas blue dashed arrows indicate non-radiative mechanisms.

4.4.1 Single molecule fluorescence microscopy

4.4.1.1 Jablonsky diagram

The physics of fluorescence is often graphically illustrated by a *Jablonski diagram*, an energetic level scheme picturing all the possible transition pathways of an excited electron among its electronic states and their vibrational substructures. For the sake of simplicity, let us refer to the system pictured in figure 4.6, where a simplified energy level structure of a molecule is shown [MF03]. In this graph, a red arrows represents a radiative process whereas a blue arrow indicates a non-radiative one.

By absorption of a photon with energy $h\nu$, the electric-dipole allowed singlet-singlet transition $S_0 \rightarrow S_1$ is pumped and the molecule is brought to a vibrational level of the electronic excited state. By *intra-molecular vibrational relaxation* or by phonon coupling with its surrounding, the molecule can relax to a lower vibrational level of the electronic excited state on a time of the order of 10^{-11} - 10^{-9} s. *Fluorescence* is defined as the emission of a photon from the excited state S_1 to a vibrational state of the lower electronic state S_0 . After the emission of a fluorescence photon, the molecule is brought back to its initial ground state by further vibrational and phonon processes.

The exact profile of the emission spectrum is governed by the Franck-Condon coupling, expressing the overlap between the different vibrational wave functions of the two electronic states S_0 and S_1 , and by the Debye-Waller factor, expressing the amplitude of the coupling of the molecular electronic structure with the phonon system of its surrounding. In general, as a relaxation step results in an energy loss, the emission spectrum will be red-shifted with respect to the profile of the absorption band.

Alternatively, the electron can undergo a non radiative transition $S_1 \rightarrow T_1$ with a production rate k_{ISC} and the molecule is left in a state with a different multiplicity. This process is often referred as *inter-system crossing*. The lifetime of the triplet state T_1 defines the transition rate k_T of the non radiative process $T_1 \rightarrow S_0$ which brings the molecule back to its lower electronic level.

4.4.1.2 Absorption related parameters

The probability associated to the absorption of a single photon is expressed by the *absorption cross section* σ_{abs} of the molecule according to the relation

$$\mathcal{P}_a = \frac{\sigma_{abs}}{A}, \quad (4.3)$$

where A indicates the cross-sectional area of the excitation laser. The maximum value of the absorption cross section is defined by the strength of the transition dipole moment and depends on the details of the electronic transition. For a two-level system like the one illustrated in figure 4.6, the (peak) σ_{abs} can be expressed in a convenient experimental way as [MF03]

$$\sigma_{abs} = 2.303 \frac{\epsilon}{N_A}, \quad (4.4)$$

where ϵ [$L mol^{-1} cm^{-1}$] is the molecular extinction coefficient as defined by the Beer-Lambert law [Har89] and N_A is the Avogadro number. Typical values for σ_{abs} are of the order of $\simeq 4 \text{ \AA}^2$.

4.4.1.3 Emission related parameters

The *fluorescence quantum yield* ϕ_F is defined as the probability of photon emission per absorption event and it is expressed by the radiative rate

k_{rad} normalized over the sum of all decay rates (both radiative and non-radiative) according to the relation [MF03]

$$\phi_F = \frac{k_{rad}}{k_{nonrad} + k_{rad}} = \frac{\tau_F}{\tau_{rad}}. \quad (4.5)$$

Equivalently, ϕ_F can be defined as the ratio between the lifetime τ_F of the excited electronic state and the radiative lifetime τ_{rad} . For a strong emitter like Rhodamine 6G, the fluorescence quantum yield is as high as $\phi_F \simeq 0.45$ while the lifetime of the first excited singlet is of the order of $\tau_F \sim 4 \text{ ns}$ ⁵[SNK⁺93].

The emission rate from a molecule is limited by the optical saturation of the dipole-dipole transition $S_0 \rightarrow S_1$. From an experimental point of view, an increase of the emission rate is observed by increasing the pumping laser intensity I up to a saturation threshold I_S . This effect often yields to the observation of an enhancement of the background photons. The limitation of the emission rate can be pictured as a lowering of the absorption cross section as [MF03]

$$\sigma = \frac{\sigma_{abs}}{1 + I/I_S}. \quad (4.6)$$

For a molecule with a three level system as the one sketched in figure 4.6, the saturation threshold is defined as [dVW80]

$$I_S = \frac{h\nu}{2\sigma\tau_F} \left[\frac{1 + (k_{ISC}/k_{10})}{1 + (k_{ISC}/2k_T)} \right]. \quad (4.7)$$

The peak on-resonance emission rate can be expressed as [PDW97]

$$R_I = R_\infty \left[\frac{I/I_S}{1 + I/I_S} \right] \quad \text{with} \quad R_\infty = \frac{(k_{10} + k_{ISC})\phi_F}{2 + (k_{ISC}/k_T)}, \quad (4.8)$$

and suggests that a further ingredient for the optimization of the fluorescing mechanism lies in the minimization of the inter-system crossing bottleneck. This minimization is a characteristic of many rigid planar aromatic dye molecules.

The average radiation lifetime of a chromophore can be further reduced by photo-chemical processes like *bleaching*, an irreversible mechanism which inhibits both the absorption and the emission of photons from

⁵by approximating the molecule to a two-level system this time results in a maximum emission rate of the order of $\simeq 10^8 \text{ s}^{-1}$ [MF03].

the molecule. This process is often related to a photo-oxidation of the fluorophore or more generally to a change of the chemical structure of the molecule [KW02, WMO94].

4.4.1.4 Single molecule sensitivity

The successful imaging of fluorescence at the single molecule level relies on several experimental parameters. An ideal setup should display both high *collection* and *detection efficiency* for the emitted photons, a small counting fluctuation (*noise*) and a minimized number of undesirable photons emitted from any source other than the molecule of interest through, for example, Rayleigh or Raman scattering processes (*background*).

Experimentally one aims for high levels of the signal-to-noise ratio (SNR), defined⁶ as [BAM92]

$$SNR = \frac{D\phi_F \left(\frac{\sigma_P}{A}\right) \left(\frac{P_0}{h\nu}\right) T}{\sqrt{\left(\frac{D\phi_F\sigma_P P_0 T}{A h\nu}\right) + C_b P_0 T + N_d T}}. \quad (4.9)$$

Here, C_b and N_d indicate the background counts per excitation power and the dark counts rate respectively, whereas the numerator is the fluorescence signal collected during the time T , where D denotes the detector efficiency and $P_0/h\nu$ the number of incident photons per second.

The choice of a suitable objective focuses first of all on the *numerical aperture* (NA) since it determines both the collection efficiency and also the resolution of the imaging process [Gel06]. If we indicate with n the refraction index of the medium between the observation sample and the objective and let ϑ be the half angle of the maximum light collection cone, the NA is expressed by the relation

$$NA = n \sin \vartheta. \quad (4.10)$$

The diffraction limit of the microscope, i.e. the minimal distance at which two different emitting sources are still distinguishable, is expressed by *Abbe's formula* [Gel06]

$$d_s = 0.5 \frac{\lambda}{NA}. \quad (4.11)$$

⁶this definition holds only for shot noise fluctuations, i.e. if the all intensities undergo Poisson fluctuations.

While the resolution of a microscope is limited by the choice of the objective, the position of a single emitter can be identified with arbitrary accuracy Δx by localizing the center of its point spread function (PSF), i.e. the intensity profile of a point-like emitter as seen by the optical system. If we approximate the PSF by a Gaussian profile, the accuracy of the spatial localization of the fluorescence emitter can be expressed by the relation [TLW02]

$$(\Delta x)^2 = \frac{s^2}{N} + \frac{a^2}{12N} + \frac{8\pi s^4 b^2}{a^2 N^2}, \quad (4.12)$$

where s is the standard deviation of the PSF, N is the number of collected photons, a is the pixel size of the detector and b represents the background counts.

4.4.2 Phthalocyanine

The term phthalocyanine often refers to a class of organic dyes whose colors range from reddish blue to yellowish green [Lř2]. All experimental results in this chapter were obtained using phthalocyanine $C_{32}H_{18}N_8$ with a mass of 514 u.

Phthalocyanine represents the ideal candidate molecule for our experiment since it combines high thermal stability, strong absorption in the visible range and high fluorescence yield. Its absorption and emission spectra have been widely investigated under different physical conditions, ranging from solutions [Pra], thin films [SG69] and supersonic jets [FWL79]. Spectroscopic data performed in chloronaphthalene solution are illustrated in figure 4.7 and provide a fluorescence yield $\phi_F = 0.6$ and an absorption cross section $\sigma_{abs} = 4.9 \cdot 10^{-16} cm^2$ at the excitation wavelength used in our setup $\lambda_{exc} = 661$ nm.

4.4.3 Single molecule epi-fluorescence microscopy

The realization of our detector is illustrated in figure 4.8. Interference fringes are deposited on a $170 \mu m$ thick quartz plate and imaged at the vacuum-air interface.

The laser excitation wavelength is chosen according to the absorption/fluorescence properties of the target molecule. A 661 nm diode laser (100 mW) is selected for the detection of phthalocyanine. The wavelength

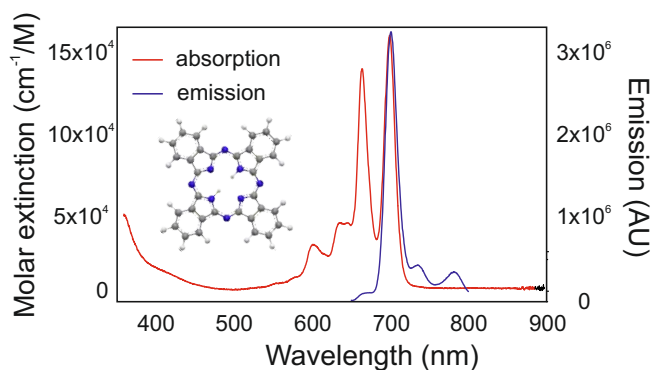


Figure 4.7: Absorption and emission spectra of phthalocyanine in chloronaphtalene solution [Pra].

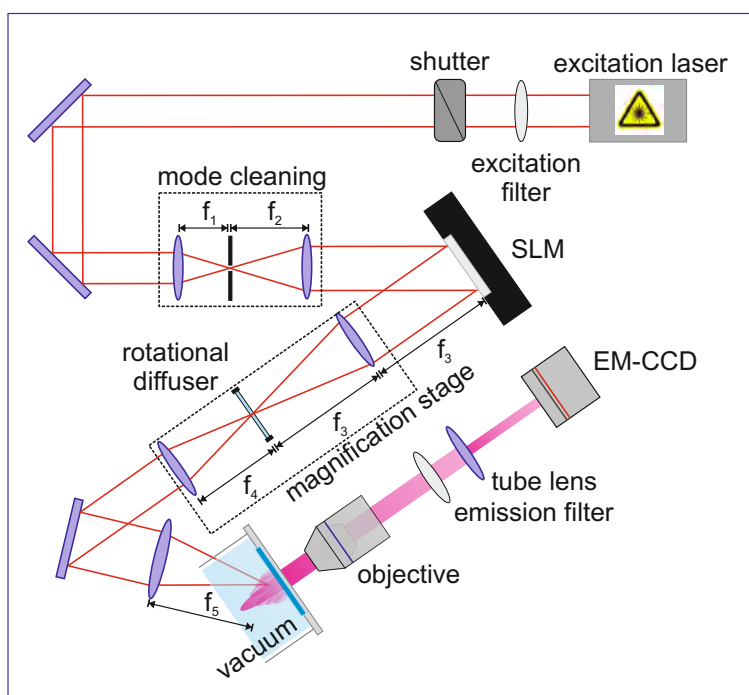


Figure 4.8: Schematic illustration of the epi-fluorescence microscopy setup. The excitation laser (661 nm, 100 mW) is guided through a mode cleaning stage ($f_1=50$ mm, $f_2=150$ mm) and beam shaped by a spatial light modulator (SLM). A flat-top shaped beam is magnified within a two lenses telescope ($f_3=400$ mm $f_4=500$ mm) and focused ($f_5=164$ mm) on the molecules collection plate at the vacuum-air interface (12 W/cm²). Fluorescence is collected by an objective and single molecules are imaged by an EM-CCD camera.

of the excitation laser is additionally selected by an excitation filter (655 ± 15 nm) and spatially filtered by a two lenses mode cleaning stage ($f_1 = 50$ mm, $f_2 = 150$ mm). A $30 \mu\text{m}$ opening pinhole is placed at the respective focal lengths of the lenses providing a Gaussian spatial mode.

For a quantitative analysis of our experimental data, we want to probe the relative population differences between high order interference maxima. For this purpose, we would have to correct the fluorescence intensity for the excitation beam profile. On the other hand, a homogeneous illumination of the quartz plate guarantees the correct interpretation of the fluorescence emission intensity.

In order to convert the Gaussian profile of the excitation laser into a squared flat-top illumination, the beam is reflected by the external surface of a spatial light modulator⁷ (SLM). The SLM consist of a matrix of liquid crystals on silicon (LCOS) technology where each pixel can be thought of as a single reflecting mirror. The application of an appropriate voltage at a pixel results in a certain degree of order in the orientation of the liquid crystals and thereby in a certain refractive index of this pixel. A phase difference is thus imposed over different spatial regions of the incident beam resulting in a shaped reflected beam. The voltage mask is supplied to the LCOS matrix in the form of a 256 gray-scale levels image mask like the one showed in figure 4.9-A. The phase mask is obtained starting from an image of the desired final shape (in our case a simple square) through an iterative *Gerchberg-Saxton algorithm* [Jes07, GS72]. A diffraction grating is superimposed to the phase mask so that the fraction of the incoming beam that is reflected from the SLM surface does not overlap with the phase modified beam.

A collection of 60 different phase masks all associated to the same desired beam shape is applied to the SLM with a frequency of 60 Hz in order to reduce the effect of light speckles on the quartz plate. In order to further improve the homogeneity of the excitation spot, the lens f_3 (400 mm) creates a real image of the flattop in the plane of a rotating diffusor, which scrambles the phase of the image. This intensity distribution is then demagnified and imaged onto the quartz plate by the lenses f_4 (500 mm) and f_5 (164 mm).

The flat top shaped beam (figure 4.9-B) is focused onto the quartz plate with an intensity of approximately 12 W/cm^2 . Figure 4.9-C shows

⁷Hamamatsu X10468-01 LCOS-SLM.

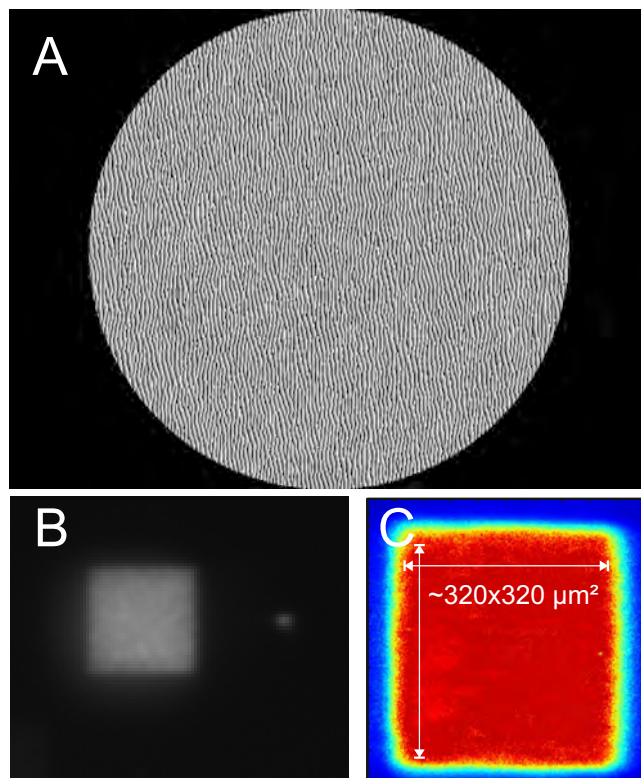


Figure 4.9: A: Gerard and Saxton phase mask for a flat top illumination - B-C: intensity modulation of the excitation beam imaged by a CMOS camera (B) and by fluorescence microscopy (C). A uniform illumination over an area of approximately $320 \times 320 \mu\text{m}^2$ is observed.

the fluorescence light emitted by a quartz plate homogenously coated with PcH_2 with the squared-shape illumination beam: an homogenous illumination area of approximately $320 \times 320 \mu\text{m}^2$ can be identified.

Single molecule sensitivity is achieved by optimizing the signal to noise ratio as suggested by equation 4.10. The emitted fluorescence light is collected by high numerical aperture objectives⁸. In order to minimize the amount of background light, the vacuum exposed surface of the quartz plate is regularly cleaned by a self-built plasma cleaner. A 10 kHz AC 1.5 kV voltage is applied to a movable sharp electrode. By approaching the electrode close to the air exposed surface of the quartz plate while a 1 mbar atmosphere of nitrogen is created in the detection chamber, a plasma is locally ignited on the vacuum side of the quartz plate. By moving the

⁸Zeiss EC Plan-Neofluar (40x/0.9 Pol - 20x/0.5).

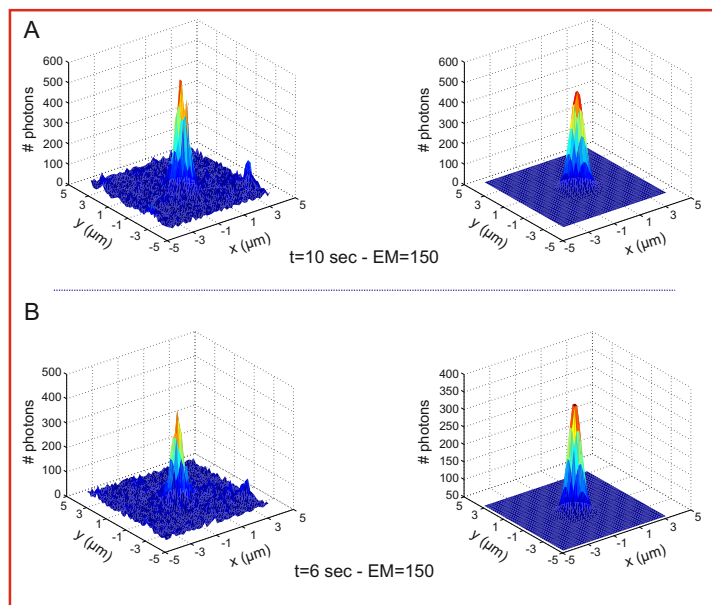


Figure 4.10: Single molecule fluorescence imaging. The intensity profile (left panels) of two emitters imaged with the same electron multiplying factor but different exposure times is shown. The intensity profiles are fitted by a Gaussian point spread function (right panels) for the estimation of the signal-to-noise ratio and the single particle location. The associated SNRs vary from SNR=30 (A) to SNR=28 (B), whereas the position of the single emitter can be localized with an accuracy $\Delta x \approx 10$ nm.

position of the plate, we can remove all molecules and dirts accumulated with time after previous depositions.

The fluorescence light is filtered by a band-pass emission filter (711 ± 25 nm) and imaged onto an electron-multiplying CCD camera⁹. The number of dark counts is further reduced by shielding the whole system from daylight whereas the number of thermal photons is reduced by operating the camera at -85°C .

Figure 4.10 shows the imaging of a single molecule for different acquisition times. The signal to noise ratio varies from 30 (figure 4.10-A) to 27 (figure 4.10-B) when the acquisition time is reduced from $t = 10$ s to $t = 6$ sec whereas the location of a single particle can be estimated with an accuracy of ≈ 10 nm.

⁹ Andor iXon EMCCD - DV885.

4.5 Evaluation of van der Waals interactions

4.5.1 Interaction with a material grating

In section 3.3.1, we calculated the interference pattern resulting from the coherent illumination of an ideal diffraction grating, i.e. we tacitly neglected the interaction with the grating bars. However, for matter-wave interference we have to account for the finite thickness t of the grating and correct the final intensity distribution for the interaction between the particle and the grating surface. A neutral particle with mass m_p propagating along the z -direction with a momentum p_z will experience an attractive potential $V(x)$ while flying at a distance x from the grating wall.

Let us first assume parallel grating walls, neglect any geometry of the periodic structure and ignore the microscopic roughness of the grating bar.

The interaction of the particle with the grating can be described as a phase imposed to the quantum wave-function and within the *eikonal approximation* it is expressed by the line integral of the action along the classical trajectory of the particle through the grating bar [HSA04].

The binary function 3.14 is thus modified according to the relation

$$\tilde{t}(x) = t(x) \cdot \exp\left(-\frac{i}{\hbar} \int_0^t V(x) \frac{dz}{v}\right) = t(x) \cdot \exp\left(-\frac{i}{\hbar} \frac{m_p t}{p_z} V(x)\right). \quad (4.13)$$

A neutral polarizable particle placed in the proximity of an infinite conducting surface will in general experience an attractive *van der Waals* (*vdW*) interaction

$$V(x) = -\frac{C_3}{x^3} \quad \text{with } C_3 > 0, \quad (4.14)$$

whose origin lies in the fluctuations of the electronic cloud of the particle and in the induction of an image dipole in the polarizable substrate.

The *van der Waals constant* C_3 is expressed by the Lifshitz formula as [DLP61]

$$C_3 = \frac{\hbar}{4\pi} \int_0^\infty \alpha(i\omega) g(i\omega) d\omega \quad [\text{nm}^3 \text{ meV}], \quad (4.15)$$

where $\alpha(i\omega)$ is the *dynamic polarizability* of the particle and

$$g(i\omega) = \frac{\epsilon(i\omega) - 1}{\epsilon(i\omega) + 1} \quad (4.16)$$

expresses the reflection coefficient of the polarizable surface. The integral 4.15 runs over all possible frequencies $\omega = k_B T / \hbar$ of the virtual photons mediating the interaction between the particle and the surface at temperature T . When $x \simeq \lambda = ch/k_B T$ the separation of the particle from the grating wall is of the same order of the wavelength associated to the virtual transition. In this situation the expression 4.14 has to be substituted by the *Casimir-Polder interaction* [BSE⁺12]

$$V(x) = -\frac{C_4}{x^4} \quad \text{with} \quad C_4 = \frac{3\hbar c}{8\pi} \alpha(0) \quad [\text{nm}^4 \text{ meV}] \quad (4.17)$$

where $\alpha(0)$ denotes the *static polarizability*.

Alternatively, the same effect can be visualized by considering the momentum kick experienced by a single particle while flying through the grating,

$$\Delta p_x = -\frac{d}{dx} V(x) \cdot \frac{b}{v_z}. \quad (4.18)$$

The van der Waals interaction constant has been measured for rare gas atoms [GST⁺99] and alkali metals [LKHC10]. As the effect of the vdW potential can be mimicked by an effective reduction of the grating opening fraction, by comparing the relative intensities of the single-grating diffraction in the far-field interference maxima

$$R_m = \frac{I_{\max}(m)}{I_{\max}(m=0)} = \left[\frac{\sin(m\pi a/d)}{m\pi a/d} \right]^2, \quad (4.19)$$

a linear dependence of the potential strength C_3 as a function of the particle polarizability α was observed.

Here, we focus on the evaluation of the vdW parameter C_3 for a thermal beam of PcH_2 interacting with SiN and Ca surfaces. We compare gratings with different opening widths and we explore the role of the thickness of the grating bars. At the same time, we discuss the limit of the theoretical approach used for the evaluation of our experimental data.

4.5.2 Experimental specifications

The role of van der Waals (vdW) interactions between the conducting wall of a material grating and a diffracted polarizable molecule has been investigated by comparing the interference patterns collected with the

five different gratings introduced in section 4.3.1 and whose specifications are listed in table 4.1. The five different interference patterns are shown in figure 4.11. Each interferogram results from the sum over four independent runs. All patterns have been previously corrected for the background, normalized for the electron multiplication factor of the CCD camera and aligned with respect to the position of the zeroth-order interference peak as well as for their velocity distribution along the height of the deposition plate.

All data have been collected under the same experimental conditions: a collimation slit with a $1\text{ }\mu\text{m}$ vertical width has been used for the preparation of the transversal coherence while the same velocity selection has been achieved by introducing a slit with a $10\text{ }\mu\text{m}$ horizontal width into the beam direction.

4.5.3 Data analysis

A direct comparison of the five fringe systems provide qualitative but clear information about the role of the vdW interaction in matter-waves interferometry.

As the vdW phase scales in a linear way with the thickness of the grating bar (equation 4.13), high order interference fringes are more easily identified for thicker gratings (G_2 and G_4) in comparison to thin ones (G_1 and G_3). For example, a more intense population density of the higher interference peaks can be identified to data related to the grating G_2 . This is even more evident when this data are compared with those related to G_1 , i.e. a grating with the same opening fraction, the same number of illuminated slits but a different thickness.

At the same time, a comparison between the experimental data related to the gratings G_1 and G_3 allows the observation of the role of the opening fraction for gratings with the same thickness. While interference maxima up to the 6-th order can be distinguished for a grating with a 79% opening fraction, a 50% opening fraction allows the identification of interference maxima up to the 9-th diffraction order. At the same time, the profile of the interference fringes related to G_3 appears to be more pronounced in comparison with the other diffraction pattern. This is in agreement with a better collimation of the beam at the interference position (lower number of overall slits).

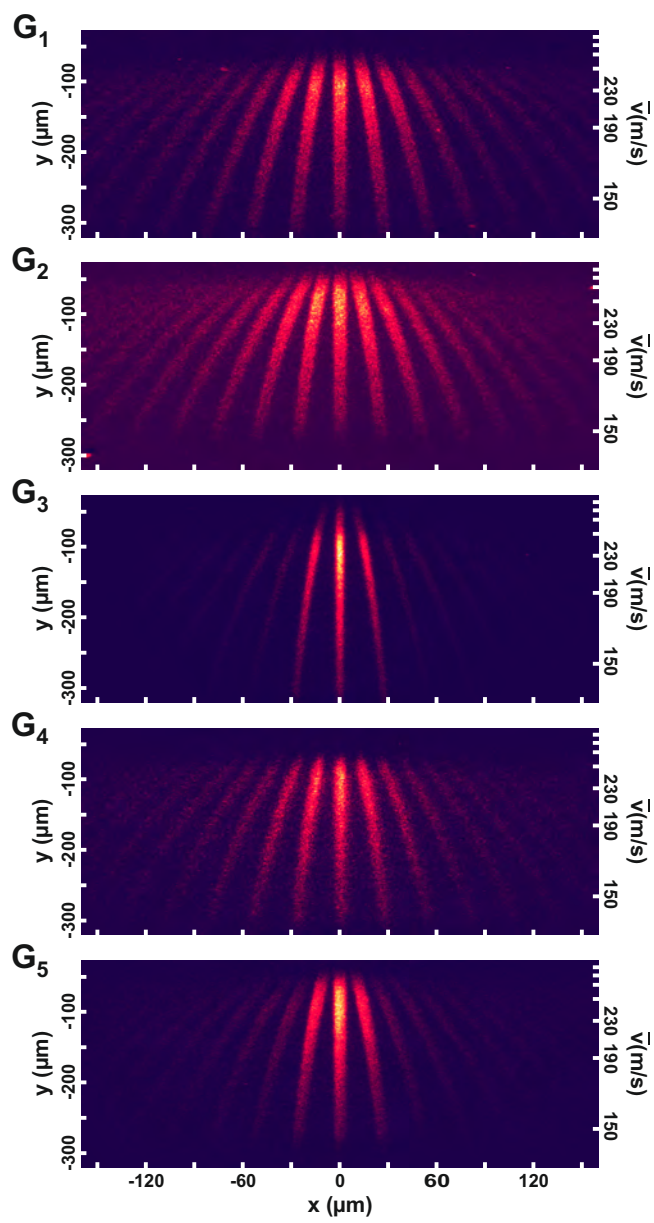


Figure 4.11: PcH_2 diffraction patterns collected with the grating set (G1-G5, see table 4.1) for the evaluation of the vdW interaction between a molecule and a grating bar.

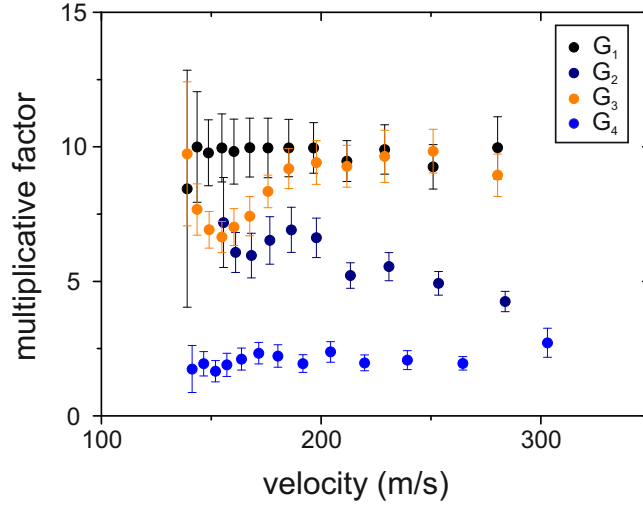


Figure 4.12: Phase multiplicative factor vs. PcH_2 velocity. Data result from the numerical evaluation of the diffraction patterns shown in figure 4.11 obtained with the grating set (G1-G4).

A quantitative analysis of the data presented in figure 4.11 has been performed with the goal of an accurate evaluation of the vdW constant C_3 for PcH_2 interacting with SiN gratings. The evaluation process can be shortly summarized as follows. Each single interferogram is divided into equally spaced intensity regions along the y-axis. The vertical sum of the diffracted intensities is numerically fitted according to equations 3.19 and 4.13. As different heights on the deposition plate correspond to different velocities as described in section 4.3.2, each data set is fitted according to the related velocity distribution profile and the finite sizes of the source are considered as well.

The analytical shape of the vdW potential has been calculated by J. Fiedler and Prof. S. Scheel at the University of Rostock, taking into account the exact geometry of each single grating and predicting the value $C_3 = 22.107 \text{ nm}^3 \text{ meV}$ for the vdW interaction constant of PcH_2 with SiN.

The numerical routine returns the overall phase multiplicative factor associated to the best fit of each diffraction intensity profile. The results of our numerical fits are shown in figure 4.12, where the multiplicative factor is here reported for the four different SiN gratings as a function of the beam velocity.

In spite of the "constant nature" of the parameter C_3 , our evaluation pro-

vides a discrepancy between the experimental data and theoretical model as high as a factor of twelve for the thinner grating (G_1 and G_3). Furthermore, while the multiplicative factor can be assumed to be constant within the error bars for G_1 and G_4 , a clear modulation of the data associated to G_2 and G_3 can be observed in the velocity range around $v=150$ m/s.

The reasons for the inconsistency between the theoretical model and the experimental data are still being explored with an eye on:

- **Influence of the polarizability anisotropy:** as expressed by equation 4.15, the vdW constant C_3 is defined as a function of the polarizability α of the molecule. In our theoretical model, the interacting molecule is approximated to be a point-like particle and a scalar polarizability is considered. A significant role may be played by spatial anisotropy, i.e. the tensor nature of α should be considered.
- **Influence of molecular rotations:** the velocity dependence of the overall multiplication phase could be related to some specific properties of the molecules. For example, when compared to an atom, a molecule is naturally characterized by a large number of vibrational and rotational degrees of freedom. For PcH_2 , the predicted moment of inertia along the main rotation axis is $I_{xx}=I_{yy}=8.3 \cdot 10^{-44}$ kg m² with $I_{zz} = 2 \times I_{xx}$. If we assume an average temperature 600 K, a simple energy conservation consideration allows the estimation of the rotation time scale of the molecule:

$$\frac{k_B T}{2} = \frac{1}{2} I_{ii} \omega_{ii}^2$$

resulting in

$$\omega_{xx} = \omega_{yy} = 3.2 \times 10^{11} \text{s}^{-1} \rightarrow T = \frac{2\pi}{\omega} = 2 \times 10^{-11} \text{s}$$

and

$$\omega_{zz} = 2.2 \times 10^{11} \text{s}^{-1} \rightarrow T = \frac{2\pi}{\omega} = 2.8 \times 10^{-11} \text{s}.$$

The transit time of a molecule propagating through a 10 nm grating at $v=200$ m/s is $\Delta t = 5 \times 10^{-11}$ s, while the same molecule flying through a 50 nm grating would take $\Delta t = 2.5 \times 10^{-10}$ s. One can therefore speculate about the influence of the molecule rotation over the flight time for thin gratings. The potential role of this effect could

be ideally tested in future experiments with gratings as thin as few atomic layers (graphene).

- **Influence of the grating bulk properties:** the vdW effect related to ultra thin membranes could differ from those associated to a thick wall. Therefore, not only the polarizability α of the molecule may change, but also variations in the bulk properties of the grating material related to its dielectric constant ϵ may play a role.
- **Influence of the finite size of the molecules:** In our theoretical model, molecules are treated as polarizable point particles. This approximation may not hold anymore for molecules whose linear dimensions are comparable to the grating thickness. The lateral extension of PcH₂ is as high as 2 nm and the grating thickness is as thin as 10 nm.
- **Influence of trapped charges:** it is very likely that during the fabrication or after investigations under the SEM microscopy charged particles may have been trapped in the bulk of the gratings or simply deposited on their surface. The random distribution of charges may actually be influential.

4.6 Coherent propagation through a biological sample

In the last decades, experimental techniques exploiting the coherent control of matter-waves have achieved tremendous improvements. For example, the equivalent of classical optical elements such as focusing lenses [CSS⁺91, DGR⁺99, ERG⁺12], mirrors [Shi01, ZMS11] or holography masks [FMK⁺96, SF02] have been realized for atoms and small molecules, paving the way for new concepts in imaging techniques and nano-scale lithography. The coherent manipulation of atoms and molecules offers the potential advantage of combining high spatial resolution (small de Broglie wavelengths) with soft surface investigation (low impact energies).

Above all, molecular diffraction can be regarded as a minimally invasive tool for the analysis of nano-structures since at a given wavelength, the kinetic energy of a particle scales inversely with its mass. While it may reach up to hundreds keV in high-resolution electron microscopy, it can

be reduced by six orders of magnitude, to as little as 100 meV for thermal dye molecules. Furthermore, the phase-sensitive nature of matter-waves makes complex molecules an interesting nano-probe, since its internal properties can be functionalized to modulate their electric, magnetic, or optical properties.

Here, we illustrate a proof-of-principle experimental test towards matter-wave coherent holography: our micro-evaporation laser source is used for the coherent illumination of a biologically grown sample, namely the skeleton (*frustule*) of the diatom *Amphipleura pellucida*, a unicellular alga occurring in natural freshwater.

4.6.1 Marine *diatoms*

Diatoms are well known objects among the microscopy society, since their variety in conformation and shape has long represented the ideal work bench for testing the resolving power of advanced imaging techniques [Nie47, HF70]. Moreover, diatoms have recently tickled the curiosity of the nano-technology community because of their potential applications in the biomimetics field. More than 100,000 different types of diatoms are known to exist and they can be easily bio-cultivated in mass amounts. Their nano-scale frustule offers some unique properties that could be exploited for the realization of novel silicon-based optical and mechanical devices. The photonic band gap of living diatoms has been investigated for the development of original light harvesting techniques whereas their skeleton nano-architecture has been often suggested as an alternative scheme for molecular separation, sensing or drug delivery [LMV09].

At the same time, the properties of the internal structure of the frustule are still poorly understood, since even modern imaging techniques - like scanning electron microscopy - can barely provide useful information. Additional investigations about the relevance and strength of the van der Waals interaction between a particle and the nano-pores are desirable, as electrostatic interactions may play a role in rheological applications where diatoms are used as a "natural" nano-filtering scheme for particles sorting [MM03].

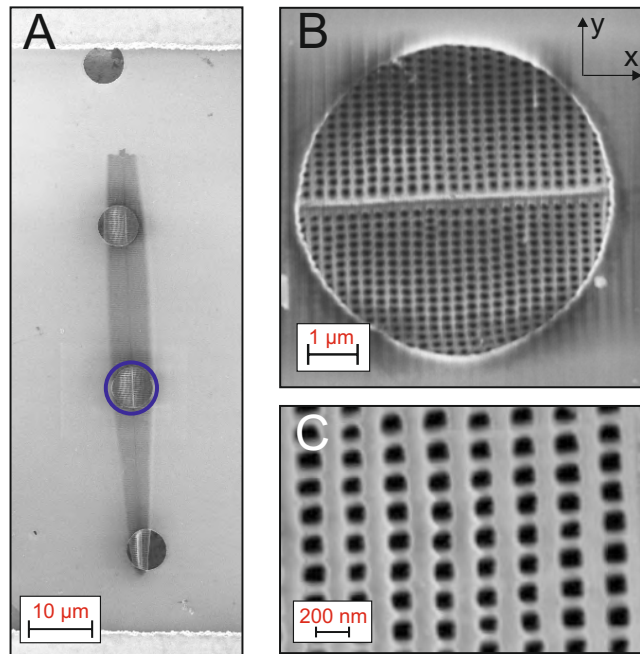


Figure 4.13: Scanning electron micrographs of the diatom *Amphipleura pellucida*. The boat-shape of the alga can be appreciated in panel (A), where the elongated shadow of the diatom can be observed behind the surface of a carbon grid. A magnified picture of the blue circled hole is shown in panel (B), illustrating the 2D periodic architecture of the SiO_2 skeleton (205 nm periodicity - 122 nm pore opening along the x-axis). The periodic structure can be further appreciated in panel C. The cell wall is ≈ 90 nm thick and it is suspended over a ≈ 110 nm thick support structure. Illustration taken from [SJK13].

4.6.2 Sample preparation

The experimental setup is essentially the one illustrated in figure 4.1, but the diffraction grating is now substituted by a sample of the diatom *Amphipleura pellucida*. The characteristic "boat-shape" structure of the alga is illustrated in figure 4.13, where three different magnification scanning electron microscope (SEM) images of the same alga are shown. The regular two dimensional architecture of the frustule can be easily appreciated. In particular, the sample presents an average periodicity of 205 nm and a typical pore opening of 122 nm along the x-axis. According to electron energy loss spectroscopy, the cell wall is roughly 90 nm thick and suspended between rod-like support structure of 110 nm thickness (see figure 4.13 - C).

The sample was prepared by gently dropping an aqueous solution of diatoms on the surface of a carbon grid as commonly used for transmission electron microscopy (TEM). After the evaporation of the solution, we were left with a random distribution of frustules electrostatically bonded to the carbon mesh. Once we had identified a diatom whose periodic structure fully covered one of the 5 μm holes of the membrane, we blocked all remaining holes by carefully gluing the TEM grid onto a 50 μm thick mylar foil such that the diatom was placed on top a 20 μm wide, laser drilled hole in the mylar foil. The sample was finally mounted in the grating holder and aligned within 5 mrad with respect to the axis of gravity.

4.6.3 Results

Figure 4.14-A shows the false-color fluorescence image of the diffraction pattern resulting from the coherent propagation of PcH_2 through the nano-structured frustule of the diatom *Amphipleura pellucida*. The interference fringes were collected over a 20 hours scan exploiting the coherence properties of our laser evaporation source.

We notice that in this case the effect of the gravitational field determines the spread of the interference fringes along the y-direction, and it reduces the expected 2D diffraction pattern to the 1D fringe system shown in figure 4.14-B, where the theoretical diffraction pattern expected for the coherent illumination of the alga nano-structure is shown.

For the sake of simplicity, let us limit our analysis to the set of data

related to the velocity band $v=142-168$ m/s, where the high order interference peaks can be appreciated in a clearer way. Starting from the SEM picture of the sampled alga (figure 4.13-B), a transmission binary mask was created and used for the calculation of the interference pattern expected in absence of gravity. The 2D diffraction pattern shown in figure 4.14-B thus represents the solution of the Kirchhoff-Fresnel diffraction integral (equation 3.3.1) where the diffraction aperture \mathcal{A} is here represented by the frustule's transmission function. The final intensities are further corrected both for the probability distribution of the considered velocity band and for the finite size of the molecular source. The vertical sum of the simulated data is plotted as the blue line in figure 4.14-C. From the comparison with the vertical sum of the experimental data (red dots), some first important conclusions can be drawn.

First, our data represent the first quantum diffraction of a complex molecule through a biologically grown nano-structure. High fringes visibility shows in an unambiguous way that we are able to coherently delocalize a single PcH_2 molecule through several pores of the alga. In spite of the "simplicity" of our setup - a tiny focused laser evaporation source and an alga - the wave nature of a complex molecule is confirmed.

By evaluating the distance between the zeroth and the first interference orders, we can reconstruct the 205 nm periodicity of the frustule along the x-axis with an accuracy of 5%.

At the same time, the populations of the higher interference orders differ significantly from those predicted by the simulation (blue line). We interpret this discrepancy as a clear demonstration of the induced phase modulation related to the van der Waals interactions between the polarizable molecules and the inner surface of the diatom skeleton. As discussed in section 4.5.1, the most prominent effect of van der Waals interactions consists in a virtual reduction of the individual pore opening size. This interpretation is further corroborated by the simulated diffraction pattern shown in figure 4.14-D, where the the Kirchhoff-Fresnel diffraction integral is now calculated while iteratively reducing the opening size of the pores of the binary mask. An increased population of the high interference orders is clearly shown by the vertical sum of the simulated intensity in figure 4.14-C (green line). The experimental high order interference peaks can be qualitatively reproduced by assuming an 83 nm effective radial reduction of the pore opening or alternatively, by assuming an electrostatic

de-phasing with an interaction constant $C_3 = 66 \text{ nm}^3 \text{ meV}$ (black line).

In spite of the "roughness" of our theoretical approach, our simulations clearly show the role of van der Waals forces in quantum diffraction through material structures. In the next section, we will show that a more refined theoretical model is far from being a trivial task even for a one dimensional nano-fabricated regular material grating. At the same time, our results suggest how molecular diffraction might actually provide some useful insights with respect to the internal material properties of our bio-mechanical mask. For example, while natural diatoms present a silica frustule, it has been shown that is also possible to systematically exchange the diatom's base material [DG03]. It would therefore be intriguing to explore topologically equivalent shapes with different atomic composition like Si, Ge or Mg, to shed more light on van der Waals interactions in real-world geometries.

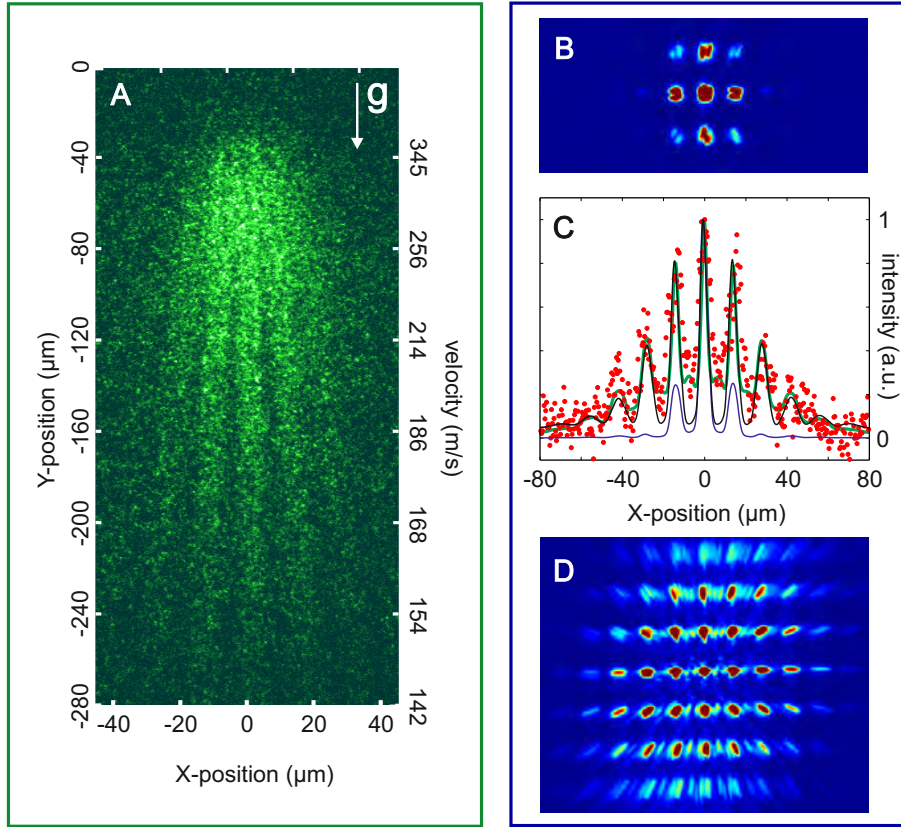


Figure 4.14: A: Coherent diffraction of PcH_2 molecules at the frustule of the diatom *Amphipleura pellucida*. B: 2D diffraction intensities simulated according to the Kirchhoff's integral (equ. 3.10). A binary transmission mask of figure 4.13-C is used as diffraction aperture. The simulation refers to the velocity range 142-168 m/s and neglects any gravity or additional phase shifts. C: The vertical sum (red dots) of the experimental intensities in the identical velocity range documents the coherent propagation of phthalocyanine through the pores of the alga. The role of van der Waals interactions is confirmed by the fact that the vertical sum (blue line) of the simulated data of panel (B) can not reproduce the experimental high order interference peaks. The visibility of the high orders can be mimicked by a 83 nm effective radial reduction of the pore opening as shown by the simulated intensities of panel (D), whose vertical sum is plotted as the green line. Alternatively, the experimental data can be reproduced by including in the numerical simulations an effective van der Waals dephasing with $C_3 = 66 \text{ nm}^3 \text{ meV}$ (black line). Illustration taken from [SJK13].

Conclusions

The main experimental results achieved during my PhD work and reported in this thesis are here shortly summarized. As the manuscript is basically divided into two distinct parts, the main conclusions will be reviewed accordingly.

Superconducting single particle detector

In the first part of this thesis, I presented a proof of concept study of the detection of beams of neutral nano-particles with a novel superconducting nano-wire detector. The arrival time distributions of the detection events related to laser desorbed molecules have been collected for different biological samples. The good consistency between the intensity profiles recorded with the new detector and the ones typically observed with a conventional photo-ionization time-of-flight mass spectrometer supports the idea that SSPDs might represent a valuable alternative detector for neutral single nano-particles. In the light of our experimental tests, we cautiously fixed the energy threshold of the detection mechanism above ≈ 20 eV.

A comprehensive characterization of the detection mechanism of SSPDs has been performed by registering the absolute detection efficiency from a beam of ionized helium extracted with a kinetic energy in the range 0.2-1 keV. We demonstrated that our devices can operate with a detection efficiency up to 100%. By investigating the detection efficiency as a function of the kinetic energy of the impinging beam, we provided a comparison of the hot-spot model between photons and massive particles. We discussed potential dissipation pathways affecting the energy deposition process in the electronic substrate of the detector, evidencing how the sensitivity of the detector is affected by the condensation of noble gases on its surface.

Finally, we suggested how the intrinsic nature of the detection mech-

anism could be exploited for future applications to atomic and molecular absorption spectroscopy.

Matter-wave interferometry

In the second part of this thesis, I explained how the quantum wave-like behavior of a massive particle (PcH_2 - 514 u) can be displayed in an unambiguous way with a single-grating diffraction in the far-field. The diffracted intensity populations are collected on an observation plate at the vacuum-air interface and imaged with an epi-fluorescence microscope with single particle sensitivity.

My investigations were mainly focused on the role of van der Waals forces in matter-wave diffraction with material gratings.

The role of van der Waals forces has been investigated by collecting the interference pattern of PcH_2 molecules with different diffraction gratings probing the role of their geometrical parameters. We focused our investigation on SiN periodic nano-structures as thin as 10 nm. The numerical evaluation of the experimental data has confirmed a significant inconsistency between the experimental observations and the theoretical predictions, paving the way to a fruitful discussion about the validity of the existing theoretical models used so far. In this regards, the present far-field setup might allow the exploration of unprecedented molecular vdW-related effects as graphene periodic structures as thin as few angstrom could be realized and implemented in near-future experiments.

I have reported the first experimental demonstration of the coherent propagation of a complex molecule through the nano-architecture of a biologically grown sample, namely the SiO_2 skeleton of the diatomic alga *Amphipleura pellucida*. A comparison with theory revealed the role of van der Waals interactions between the molecules and the inner surface of the alga's pore. This experiment can be regarded as a first promising step towards complex coherent control schemes with molecules, such as holography. As a tomographic reconstruction of the biological sample is feasible, our setup could represent a valuable supporting tool to microscopy.

Acknowledgements

This work would have not been possible without the help and the support of several people which I will try to thank in the following lines.

My first and most natural thank goes to Prof. Dr. M. Arndt, for the opportunity of working on such a fascinating and stimulating research field. For his constant guidance, his precious helps and suggestions, his unfathomable (I swear this word really exists) patience and dedication.

I would like to thank the group of Prof. G. Goltsmann from the Pedagogical University of Moscow for the realization of the superconducting nano-wire detectors.

I am grateful to Prof. O. Cheshnovsky from the Tel Aviv University for the realization of the SiN diffraction gratings.

I acknowledge Prof. S. Scheel and J. Fiedler from the University of Rostock for their theoretical support to the evaluation of the van der Waals interactions in single-grating diffraction experiments with matter-waves.

I would like to thank all the administrative stuff of the group, the guys from the workshop and S. Puchegger for his help with the scanning electron microscope.

During these 4 years, I had the unique opportunity of sharing my day (and night) life with a group of people that I like to consider as friends, rather than colleagues. Together with them I managed to go through numerous experimental challenges and faced everyday life difficulties. Therefore, my biggest acknowledgement goes to Markus Marksteiner, Philipp Haslinger, Philipp Schmid and Thomas Juffmann.

A special thank is reserved to Stefan Nimmrichter for being a daily theoretical guiding light in dark experimental times.

Finally, I would like to thank all the members of the group of Quantum

Nanophysics and Molecular Quantum Optics of the University of Vienna for the pleasant working environment and acknowledge J. Whitfield, P. Schmid and T. Juffmann for correcting my thesis. I owe S. Kuhn and M. Tillman a drink for their help in translating my abstract in a honest German.

I am grateful to my family for their absolute love and support, in spite of the 2,024 km separating us.

I have been able to get by these 4 years with a little help of my friends (yes, it is a quote). Although they are scattered almost all around the continent, I will always feel at home by them. A greater thank goes to Spillo, Alessandro, Antonio, Stefania, Marco e Sofia for their constant support along this personal sentimental resistance.

Bibliography

- [AMB94] C.R. Ayre, L. Moro, and C.H. Becker. Effects of desorption methods and photoionizing laser characteristics on molecular fragmentation. *Anal. Chem.*, 66:1610–1619, 1994.
- [ANVA⁺99] M. Arndt, O. Nairz, J. Vos-Andreae, C. Keller, G. van der Zouw, and A. Zeilinger. Wave-particle duality of C₆₀ molecules. *Nature*, 401:680–682, 1999.
- [AWG95] K.P. Aicher, U. Wilhelm, and J. Grotemeyer. Multiphoton ionization of molecules: a comparison between femtosecond and nanosecond laser pulse ionization efficiency. *J. Am. Soc. Mass Spectrom.*, 6:1059–1068, 1995.
- [BAM92] Th. Basché, W.P. Ambrose, and W.E. Moerner. Optical spectra and kinetics of single impurity molecules in a polymer: spectral diffusion and persistent spectral hole burning. *J. Opt. Soc. Am. B*, 9:829, 1992.
- [BAVL⁺81] Ch.J. Bordé, S. Avrillier, A. Van Lerberghe, Ch. Salomon, D. Bassi, and G. Scoles. Observation of optical ramsey fringes in the 10 μ m spectral region using a supersonic beam of SF₆. *J. Phys. Colloques*, 42:C8–15–C8–19, 1981.
- [BBSZ81] D. Bassi, A. Boschetti, M. Scotoni, and M. Zen. Molecular beam diagnostics by means of fast superconducting bolometer and pulsed infrared-laser. *Appl. Phys. B - Lasers O.*, 26:99–103, 1981.
- [BCDN⁺97] A. Brunelle, P. Chaurand, S. Della Negra, Y. Le Beyec, and E. Parillis. Secondary electron emission yields from a CsI

surface under impacts of large molecules at low velocities 5×10^{-3} – 7×10^{-4} ms⁻¹. *Rap. Comm. Mass Sp.*, 11:353–362, 1997.

- [BFG⁺02] R. Brühl, P. Fouquet, R.E. Grisenti, J.P. Toennies, G.C. Hegerfeldt, T. Köhler, M. Stoll, and C. Walter. The van der Waals potential between metastable atoms and solid surfaces: novel diffraction experiment vs. theory. *Europhys. Lett.*, 59:357–363, 2002.
- [BK95] C.H. Becker and Wu K.J. On the photoionization of large molecules. *J. Am. Soc. Mass Spectrom.*, 6:883–888, 1995.
- [Blu92] N. Bluzer. Temporal relaxation measurements of photoinduced nonequilibrium in superconductors. *J. Appl. Phys.*, 71:1336–1348, 1992.
- [BMKH97] S. Berkenkamp, C. Menzel, M. Karas, and F. Hillenkamp. Performance of infrared matrix-assisted laser desorption/ionization mass spectrometry with lasers emitting in the 3 μ m wavelength range. *Rapid Comm. Mass Sp.*, 11:1399–1406, 1997.
- [Bor93] Born, M. and Wolf, E. *Principles of optics*. Pergamon Press, 1993.
- [BSDA07] M. Berninger, A. Stefanov, S. Deachapunya, and M. Arndt. Polarizability measurements in a molecular near-field interferometer. *Phys. Rev. A*, 76:013607, 2007.
- [BSE⁺12] S.Y. Buhmann, S. Scheel, S.A Ellingsen, K. Hornberger, and A. Jacob. Casimir-Polder interaction of fullerene molecules with surfaces. *Phys. Rev. A*, 85:042513, 2012.
- [BTK95] A. Budrevich, B. Tsipinyuk, and E. Kolodney. Generation and energy analysis of neutral C₆₀ seeded molecular beam up to 60 eV with electrostatic energy analyzer. *Chem. Phys. Lett.*, 234:253–259, 1995.
- [CEE⁺12] A. Casaburi, E. Esposito, M. Ejrnaes, K. Suzuki, M. Ohkubo, S. Pagano, and R. Cristiano. A 2 x 2 mm² superconducting

- strip-line detector for high-performance time-of-flight mass spectrometry. *Supercond. Sci. Technol.*, 25:115004, 2012.
- [CEM⁺12] J. Chaste, A. Eichler, J. Moser, G. Ceballos, R. Rurali, and A. Bachtold. A nanomechanical mass sensor with yoctogram resolution. *Nat. Nanotechnol.*, 7:301–304, 2012.
- [CEZ⁺11] A. Casaburi, M. Ejrnaes, N. Zen, M. Ohkubo, S. Pagano, and R. Cristiano. Thicker, more efficient superconducting strip-line detectors for high throughput macromolecules analysis. *Appl. Phys. Lett.*, 98, 2011.
- [CMSY71] M. Cavallini, L. Meneghetti, G. Scoles, and M. Yealland. Molecular beam scattering apparatus with a low temperature bolometer detector. *Rev. Sci. Instrum.*, 42:1759, 1971.
- [CP04] A. D. Cronin and J.D. Perrault. Phasor analysis of atom diffraction from a rotated material grating. *Phys. Rev. A*, 70:043607, 2004.
- [CSP09] A.D. Cronin, J. Schmiedmayer, and D.E. Pritchard. Optics and interferometry with atoms and molecules. *Rev. Mod. Phys.*, 81:1051–1129, 2009.
- [CSS⁺91] O. Carnal, M. Sigel, T. Sleator, H. Takuma, and J. Mlynek. Imaging and focusing of atoms by a Fresnel zone plate. *Phys. Rev. Lett.*, 67:3231–3234, 1991.
- [CWP] A.D. Cronin, L. Wang, and J.D. Perrault. Limitation of nanotechnology for atom interferometry. *arXiv:physics/0508032 [physics.atom-ph]*.
- [dB23] L. de Broglie. Waves and Quanta. *Nature*, 112:540, 1923.
- [DG27] C. Davisson and L.H. Germer. The scattering of electrons by a single crystal of nickel. *Nature*, 119:558–560, 1927.
- [DG03] R.W. Drum and R. Gordon. Star Trek replicators and diatom nanotechnology. *Trends Biotechnol.*, 21:325–328, 2003.

- [DGR⁺99] R.B. Doak, R.E. Grisenti, S. Rehbein, G. Schmal, J.P. Toennies, and Ch. Wöll. Towards realization of an atomic de Broglie microscope: helium atom focusing using Fresnel zone plates. *Phys. Rev. Lett.*, 83:4229–4232, 1999.
- [DHC⁺94] D. Ding, J. Huang, R.N. Compton, E. Klotz, and R.E. Haufler. cw laser ionization of C₆₀ and C₇₀. *Phys. Rev. Lett.*, 73:1084–1087, 1994.
- [DLP61] I.E. Dzyaloshinskii, E.M. Lifshitz, and L.P. Pitaevskii. General theory of van der Waals forces. *Soviet Physics Uspekhi*, 73:153–176, 1961.
- [Dre03] K. Dreisewerd. The desorption process in MALDI. *Chem. Rev.*, 103:395, 2003.
- [dVW80] H. de Vries and D.A. Wiersma. Photophysical and photochemical molecular hole burning theory. *J. Chem. Phys.*, 72:1851–1863, 1980.
- [EBH⁺09] B.V. Estey, J.A. Beall, G.C. Hilton, K.D. Irwin, D.R. Schmidt, J.N. Ullom, and R.E. Schwall. Time-of-flight mass spectrometry with latching Nb meanders detectors. *IEEE T. Appl. Supercon.*, 19:382–385, 2009.
- [EGA⁺13] S. Eibenberger, S. Gerlich, M. Arndt, M. Mayor, and J. Tüxen. Matter-wave interference with particles selected from a molecular library with masses exceeding 10,000 amu. *Phys. Chem. Chem. Phys.*, accepted for publication, 2013.
- [EMC⁺06] P.D. Edirisinghe, J.F. Moore, W.F. Calaway, I.V. Veryovkin, M.J. Pellin, and L. Hanley. Vacuum ultraviolet postionization of aromatic groups covalently bound to peptides. *Anal. Chem.*, 78:5876–5883, 2006.
- [ERG⁺12] S.D. Eder, T. Reisinger, M.M. Greve, G. Bracco, and B. Holst. Focusing of a neutral helium beam below one micron. *New J. Phys.*, 14:073014, 2012.
- [ES30] I. Estermann and O. Stern. Beugung von Molekularstrahlen. *Z. Phys.*, 1930:95–125, 1930.

- [Fey65] Feynmann, R. *The Feynmann lectures on physics - Volume III: Quantum mechanics*. Addison-Wesley, 1965.
- [FLWB99] M. Frank, S.E. Labov, G. Westmacott, and W.H. Benner. Energy-sensitive cryogenic detectors for high-mass biomolecule mass spectrometry. *Mass Spectrom. Rev.*, 18:155–186, 1999.
- [FMK⁺96] J. Fujita, M. Morinaga, T. Kishimoto, M. Yasuda, S. Matsui, and Shimi. Manipulation of an atomic beam by a computer-generated hologram. *Nature*, 380:691–694, 1996.
- [FMM⁺89] J.B. Fenn, M. Mann, C.K. Meng, S.F. Wong, and C.M. Whitehouse. Electrospray ionization for mass-spectrometry of large biomolecules. *Science*, 246:64–71, 1989.
- [FWL79] P.S.H. Fitch, L. Wharton, and D.H. Levy. The fluorescence spectrum of free base phthalocyanine cooled in a supersonic free jet. *J. Chem. Phys.*, 70:2018, 1979.
- [Gel06] Gell, C. and Brockwell, D. and Smith, A. *Handbook of single molecule fluorescence spectroscopy*. Oxford University Press, 2006.
- [GET⁺11] S. Gerlich, S. Eibenberger, M. Tomandl, S. Nimmrichter, K. Hornberger, P.J. Fagan, J. Tüxen, M. Mayor, and M. Arndt. Quantum interference of large organic molecules. *Nat. Commun.*, 2:263, 2011.
- [GGU⁺08] S. Gerlich, M. Gring, H. Ulbricht, K. Hornberger, J. Tüxen, M. Mayor, and M. Arndt. Matter-wave metrology as a complementary tool for mass spectrometry. *Angew. Chem. Int. Ed.*, 47:6195–6198, 2008.
- [GHH⁺07] S. Gerlich, L. Hackermüller, K. Hornberger, A. Stibor, H. Ulbricht, T. Savas, M. Muri, M. Mayor, and M. Arndt. A Kapitza-Dirac-Talbot-Lau interferometer for highly polarizable molecules. *Nat. Phys.*, 3:711, 2007.

- [GRT78] G. Gallinaro, G. Roba, and R. Tatarek. Molecular beam detection by fast superconducting bolometers. *J. Phys. E: Sci. Instrum.*, 11:628–630, 1978.
- [GS22] W. Gerlach and O. Stern. The experimental evidence of direction quantization in the magnetic field. *Z. Phys.*, 9:349–352, 1922.
- [GS72] R.W Gerchberg and W.O. Saxton. A practical algorithm for the determination of phase from image and diffraction plane pictures . *Optik*, 35:237–246, 1972.
- [GS00] I.S. Gilmore and M.P. Seah. Ion detection efficiency in SIMS: Dependencies on energy, mass and composition for microchannel plates used in mass spectrometry. *Int. J. Mass Spectrom.*, 202:217–229, 2000.
- [GSK⁺03] G.N. Goltsman, K. Smirnov, P. Kouminov, B. Voronov, N. Kaurova, V. Drakinsky, J. Zhang, A. Verevkin, and R. Sobolewski. Fabrication of nanostructured superconducting single-photon detectors. *IEEE T. Appl. Supercon.*, 13:192–195, 2003.
- [GST⁺99] R.E. Grisenti, W. Schöllkopf, J.P. Toennies, G.C. Hegerfeldt, and T. Köhler. Determination of atom-surface van der Waals potentials from transmission-grating diffraction intensities. *Phys. Rev. Lett.*, 9:1755–1758, 1999.
- [Har89] Harris, D.C. and Bertolucci, M.D. *Simmetry and spectroscopy - An introduction to vibrational and electronic spectroscopy*. Dover Publication, Inc., New York, 1989.
- [HDG⁺13] P. Haslinger, N. Dörre, P. Geyer, J. Rodewald, S. Nimmrichter, and M. Arndt. A universal matter-wave interferometer with optical ionization gratings in the time domain. *Nat. Phys.*, 9:144–148, 2013.
- [HDL⁺99] V. Horneffer, K. Dreisewerd, H.-C. Lüdemann, F. Hillenkamp, M. Läge, and K. Strupat. Is the incorporation

of analytes into matrix crystals a prerequisite for matrix-assisted laser desorption/ionization mass spectrometry? A study of five positional isomers of dihydroxybenzoic acid. *Int. J. Mass Spectrom.*, 185/186/187:859–870, 1999.

- [HE97] K. Hansen and O. Echt. Thermionic emission and fragmentation of C_{60} . *Phys. Rev. Lett.*, 78:2337–2340, 1997.
- [HEC⁺06] L. Hanley, P.D. Edirisinghe, W.F. Calaway, I.V. Veryovkin, M.J. Pellin, and J.F. Moore. 7.87 eV postionization of peptides containing tryptophan or derivatized with fluorescein. *Appl. Surf. Sci.*, 252:6723–6726, 2006.
- [HF70] G.R. Hasle and A. Fryxell. Diatoms: cleaning and mounting for light and electron microscopy. *T. Am. Microsc. Soc.*, 89:469–474, 1970.
- [HGH⁺12] K. Hornberger, S. Gerlich, P. Haslinger, S. Nimmrichter, and M. Arndt. Colloquium: Quantum interference of clusters and molecules. *Rev. Mod. Phys.*, 84:157–173, 2012.
- [HHB⁺04] L. Hackermüller, K. Hornberger, B. Brezger, A. Zeilinger, and M. Arndt. Decoherence of matter waves by thermal emission of radiation. *Nature*, 427:711–714, 2004.
- [HKA⁺99] L. Hanley, O. Kornienko, E.T. Ada, E. Fuoco, and J.L. Trevor. Surface mass spectrometry of molecular species. *J. Mass Spectrom.*, 34:705–723, 1999.
- [HP36] H. v. Jr Halban and P. Preiswerk. Preuve expérimentale de la diffraction des neutrons. *C. R. Acad. Sci.*, 203:73–75, 1936.
- [HSA04] K. Hornberger, J.E. Sipe, and M. Arndt. Theory of decoherence in a matter wave Talbot-Lau interferometer. *Phys. Rev. A*, 70:053608, 2004.
- [HUB⁺03] K. Hornberger, S. Uttenthaler, B. Brezger, L. Hackermüller, M. Arndt, and A. Zeilinger. Collisional decoherence observed in matter wave interferometry. *Phys. Rev. Lett.*, 90:160401, 2003.

- [HZ09] L. Hanley and R. Zimmermann. Light and molecular ions: the emergence of vacuum UV single-photon ionization in MS. *Anal. Chem.*, 81:4174–4182, 2009.
- [Jes07] M. Jesacher. *Application of spatial light modulators for optical trapping and image processing*. PhD thesis, Leopold-Franzens University, Innsbruck, 2007.
- [JMM⁺12] T. Juffmann, A. Milic, M. Müllneritsch, P. Asenbaum, A. Tsukernik, J. Tüxen, M. Mayor, O. Cheshnovsky, and M. Arndt. Real-time single-molecule imaging of quantum interference. *Nat. Nanotechnol.*, 7:297–300, 2012.
- [Jou08] Jousten, K., editor. *Handbook of vacuum technology*. John Wiley and Sons, 2008.
- [JTG⁺09] T. Juffmann, S. Truppe, P. Geyer, A.G. Major, S. Deachapunya, H. Ulbricht, and M. Arndt. Wave and particle in molecular interference lithography. *Phys. Rev. Lett.*, 103:263601, 2009.
- [KBH85] M. Karas, D. Backmann, and F. Hillenkamp. Influence of the wavelength in high-irradiance ultraviolet laser desorption mass spectrometry of organic molecules. *Anal. Chem.*, 57:2935–2939, 1985.
- [KG51] A. Kantrowitz and J. Grey. A high intensity source for the molecular beam. 1. Theretical. *Rev. Sci. Instrum.*, 22:328–332, 1951.
- [KH88] M. Karas and F. Hillenkamp. Laser desorption ionization of proteins with molecular masses exceeding 10,000 daltons. *Anal. Chem.*, 60:2299–2301, 1988.
- [KJ96] A.M. Kadin and M.W. Johnson. Nonequilibrium photon-induced hotspot: A new mechanism for photodetection in ultrathin metallic films. *Appl. Phys. Lett.*, 69(25):3938–3940, DEC 16 1996.

- [KLS91] G.R. Kinsel, J. Lindner, J. Grotemeyer, and E.W. Schlag. Absorption effects in laser desorption of neutral organic molecules. *J. Phys. Chem.*, 95:7824–7830, 1991.
- [KTB94] E. Kolodney, B. Tsipinyuk, and A. Budrevich. The thermal stability and fragmentation of C_{60} molecule up to 2000 K on the milliseconds time scale. *J. Chem. Phys.*, 100:8542–8545, 1994.
- [KW02] A.N. Kapadinis and S. Weiss. Fluorescent probes and bioconjugation chemistries for single-molecule fluorescence analysis of biomolecules. *J. Chem. Phys.*, 117:10953, 2002.
- [L12] G. Löbbert. Phthalocyanines. *Ullmanns encyclopedia of industrial chemistry*, 27:181–213, 2012.
- [Lev94] R.J. Levis. Laser desorption and ejection of biomolecules from the condensed phase into the gas phase. *Annu. Rev. Phys. Chem.*, 45:483–518, 1994.
- [LKH10] V.P.A. Lonij, C.E. Klauss, W.F. Holmgren, and A.D. Cronin. Atom diffraction reveals the impact of atomic core electrons on atom-surface potentials. *Phys. Rev. Lett.*, 105:233202, 2010.
- [LMV09] D. Losic, J.G. Mitchell, and N.H. Voelcker. Diatomaceous lessons in nanotechnology and advanced materials. *Adv. Mater.*, 21:2947–2958, 2009.
- [Mar10] M. Marksteiner. *Production and detection of neutral molecular beams: from single amino acids to biomolecular complexes*. PhD thesis, University of Vienna, 2010.
- [MDS⁺09] M. Marksteiner, A. Divochiy, M. Sclafani, P. Haslinger, H. Ulbricht, A. Korneev, A. Semenov, G. Gol’tsman, and M. Arndt. A superconducting NbN detector for neutral nanoparticles. *Nanotechnology*, 20:455501, 2009.
- [MdVHW90] G. Meijer, M.S. de Vries, H.E. Hunziker, and H.R. Wendt. Laser desorption jet-cooling of organic molecules. *Appl. Phys. B*, 51:395–403, 1990.

- [MF03] W.E. Moerner and D.P. Fromm. Methods of single-molecule fluorescence spectroscopy and microscopy. *Rev. Sci. Instrum.*, 74:35973619, 2003.
- [MHS⁺09] M. Marksteiner, P. Haslinger, M. Sclafani, H. Ulbricht, and M. Arndt. UV and VUV ionization of organic molecules, clusters and complexes. *J. Phys. Chem. A*, 113:9952–9957, 2009.
- [MHU⁺08] M. Marksteiner, P. Haslinger, H. Ulbricht, M. Sclafani, H. Oberhofer, C. Dellago, and M. Arndt. Gas-phase formation of large neutral alkaline-earth metal tryptophan complexes. *J. Am. Soc. Mass Spectrom.*, 19:1021–1026, 2008.
- [MM03] S. Matthias and F. Müller. Asymmetric pores in a silicon membrane acting as massively parallel brownian ratchets. *Nature*, 424:53–57, 2003.
- [NHH⁺09] A.Z. Naik, M.S. Hanay, W.K. Hiebert, X.L. Feng, and M.L. Roukes. Towards single-molecule nanomechanical mass spectrometry. *Nat. Nanotechnol.*, 4:445–450, 2009.
- [NHHA11] S. Nimmrichter, K. Hornberger, P. Haslinger, and M. Arndt. Testing spontaneous localization theories with matter-wave interferometry. *Phys. Rev. A*, 83:043621, 2011.
- [Nie47] J.E. Nielsen. Electron microscope reveals a possible valve structure of *Amphipleura pellucida*. *T. Am. Microsc. Soc.*, 66:140–143, 1947.
- [NKUA08] S. Nimmrichter, Hornberger K., H. Ulbricht, and M. Arndt. Absolute absorption spectroscopy based on molecule interferometry. *Phys. Rev. A*, 78:063607, 2008.
- [NTH12] C.M. Natarajan, M.G. Tanner, and R.H. Hadfield. Superconducting nanowire single-photon detectors: physics and applications. *Supercond. Sci. Tech.*, 25:063001, 2012.
- [Pau00] Pauly, H. *Atom, Molecule and Cluster Beams I*. Springer, 2000.

- [PDEK06] F.S. Patton, D.P. Deponete, G.S. Elliot, and S.D Kevan. Speckle patterns with atomic and molecular de Broglie waves. *Phys. Rev. Lett.*, 97:013202, 2006.
- [PDW97] T. Plakhotnik, E.A. Donley, and U.P. Wild. Single-molecule spectroscopy. *Annu. Rev. Phys. Chem.*, 48:181–212, 1997.
- [Poo07] Poole, C.P. *Superconductivity*. Oxford : Academic, 2007.
- [Pra] S. Prahl. Phatlocyanine, Pc. *Oregon medical laser center* - <http://omlc.ogi.edu/spectra/PhotochemCAD/html/074.html>.
- [PRD⁺09] D. Pentlehner, R. Riechers, B. Dick, A. Slenczka, U. Even, N. Lavie, R. Brown, and L. Kfir. Rapidly pulsed helium droplets source. *Rev. Sci. Instrum.*, 80:043302, 2009.
- [Rau00] Rauch, H. and Werner, S.A. *Neutron interferometry - Lessons in experimental qunatum mechanics*. Oxford Science Publications, 2000.
- [RLM⁺10] M. Rosticher, F.R. Ladan, J.P. Maneval, S.N. Dorenbroos, T. Zijlstra, and et al. A high efficiency superconducting nanowire single electron detector. *Appl. Phys. Lett.*, 97:183106, 2010.
- [Scl09] M. Sclafani. Tecniche sperimentali per interferenza quantistica con cluster organici e molecole. Master’s thesis, Università degli studi di Palermo, Facoltà di scienze, Laurea in Fisica, A.A. 2008/2009.
- [Sco88] Scoles, G. *Atomic and molecular beam methods - Volume 1*. Oxford University Press, 1988.
- [SF02] F. Shimizu and J. Fujita. Reflection-type hologram for atoms. *Phys. Rev. Lett.*, 88:123201, 2002.
- [SG69] P.G. Seybold and M. Gouterman. XIII: fluorescence spectra and quantum yields. *J. Mol. Spectrosc.*, 31:1–13, 1969.
- [SGK01] A.D. Semenov, G.N. Gol’tsman, and A.A. Korneev. Quantum detection by current carrying superconducting film. *Physica C*, 351:349–356, 2001.

- [SGL92] E.W. Schlag, J. Grotemeyer, and R.D. Levine. Do large molecules ionize? *Chem. Phys. Lett.*, 190:521–527, 1992.
- [Shi01] F. Shimizu. Specular reflection of very slow metastable Neon atoms from a solid surface. *Phys. Rev. Lett.*, 86:987–990, 2001.
- [SJKA13] M. Sclafani, T. Juffmann, C. Knobloch, and M. Arndt. Quantum coherent propagation of complex molecules through the frustule of the alga *Amphipleura pellucida*. *New J. Phys.*, Accepted for publication, 2013.
- [SL92] E.W. Schlag and R.D. Levine. Ionization, charge separation, charge recombination and electron transfer in large systems. *J. Phys. Chem.*, 96:10608–10616, 1992.
- [SMMK⁺12] M. Sclafani, M. Marksteiner, F. McLennan Keir, A. Divochiy, A. Korneev, A. Semenov, G. Gol’tsman, and M. Arndt. Sensitivity of a superconducting nanowire detector for single ions at low energy. *Nanotechnology*, 23:065501, 2012.
- [SMS⁺08] K. Suzuki, S. Miki, S. Shiki, Z. Wang, and M. Ohkubo. Time resolution improvement of superconducting NbN stripline detectors for Time-of-flight mass spectrometry. *Appl. Phys. Express*, 1, 2008.
- [SNG⁺95] A.D. Semenov, R.S. Nebosis, Y.P. Gousev, M.A. Heusinger, and K.F. Renk. Analysis of the nonequilibrium photoreponse of superconducting films to pulsed radiation by use of a two-temperature model. *Phys. Rev. B*, 52(1):581–590, JUL 1 1995.
- [SNK⁺93] S.A. Soper, H.L. Nutter, R.A. Keller, L.M. Davis, and E.B. Shera. The photophysical constants of several fluorescent dyes pertaining to ultrasensitive fluorescence spectroscopy. *Photochem. Photobiol.*, 57:972–977, 1993.
- [SSA⁺13] P. Schmid, F. Stöhr, M. Arndt, J. Tüxen, and M. Mayor. Single-photon ionization of organic molecules beyond 10 kDa. *J. Am. Soc. Mass Spectrom.*, 24:602–608, 2013.

- [ST96] W. Schöllkopf and J. Toennies. The non destructive detection of the helium dimer and trimer. *J. Chem. Phys.*, 104:1155, 1996.
- [Ste20] O. Stern. A direct measurement of thermal molecular speed. *Z. Phys.*, 2:49, 1920.
- [STSS98] W. Schöllkopf, J.P. Toennies, T.A. Savas, and H.I. Smith. A cluster size nanofilter with variable openings between 2 and 50 nm. *J. Chem. Phys.*, 109:9252, 1998.
- [Tes71] L.R. Testardi. Destruction of superconductivity by laser light. *Phys. Rev. B*, 4(7):2189, 1971.
- [TLW02] R.E. Thompson, D.R. Larson, and W.W. Webb. Precise nanometer localization analysis for individual fluorescent probes. *Biophys. J.*, 82:2775–2783, 2002.
- [TV04] J.P. Toennies and A.F. Vilesov. Superfluid helium droplets: a uniquely cold nanomatrix for molecules and molecular complexes. *Angew. Chem. Int. Ed.*, 43:2622–2648, 2004.
- [TVG⁺96] D. Twerenbold, J.L. Vuilleumier, D. Gerber, A. Tadsen, B. van den Brandt, and P.M. Gillevet. Detection of single macromolecules using a cryogenic particle detector coupled to a biopolymer mass spectrometer. *Appl. Phys. Lett.*, 68:375–384, 1996.
- [TWI⁺88] K. Tanaka, H. Waki, Y. Ido, S. Akita, Y. Yoshita, T. Yoshida, and T. Matsuo. Protein and polymer analyses up to m/z 100000 by laser ionization time-of-flight mass spectrometry. *Rapid Comm. Mass Sp.*, 2-8:151–153, 1988.
- [VZS⁺02] A. Verevkin, J. Zhang, R Sobolewski, A Lipatov, O Okunev, G Chulkova, A. Korneev, K Smirnov, G. Gol'tsman, and A Semenov. Detection efficiency of large-active-area NbN single-photon superconducting detectors in the ultraviolet to near-infrared range. *Appl. Phys. Lett.*, 80:4687–89, 2002.

- [WAW⁺94] R. Weinkauf, P. Aicher, G Wesley, J Grotemeyer, and E.W. Schlag. Femtosecond versus nanosecond multiphoton ionization and dissociation of large molecules. *J. Phys. Chem.*, 98:8381–8391, 1994.
- [WDA03] C. Weickhardt, L. Draack, and A. Amirav. Laser desorption combined with hyperthermal surface ionization time-of-flight mass spectrometry. *Anal. Chem.*, 73:5602–5607, 2003.
- [WJCN⁺06] K.R Wilson, M. Jimenez-Cruz, C. Nicolas, L. Belau, S.R. Leone, and M. Ahmed. Thermal vaporization of biological nanoparticles: fragment-free vacuum ultraviolet photoionization mass spectra of tryptophan, phenylalanine-glycine-glycine, and β -carotene. *J. Phys. Chem. A*, 110:2106–2113, 2006.
- [WMO94] F. Wilkinson, D.J. McGarvey, and A.F. Olea. Excited triplet state interactions with molecular oxygen: influence on charge transfer on the bimolecular quenching rate constants and the yields of singlet oxygen for substituted naphthalenes in various solvent. *J. Phys. Chem.*, 98:3762–3769, 1994.
- [YKD⁺07] J.K.W. Yang, A.J. Kerman, E.A. Dauler, V. Anant, K.M. Rosfjord, and K.K. Berggren. Modeling the electrical and thermal response of superconducting nanowire single-photon detectors. *IEEE T. Appl. Supercon.*, 17:581–585, 2007.
- [ZKG97] L.V. Zhigilei, P.B.S. Kodali, and B.J. Garrison. Molecular dynamics model for laser ablation and desorption of organic solids. *J. Phys. Chem. B*, 101:2028–2037, 1997.
- [ZMS11] B.S. Zhao, G. Meijer, and W. Schöllkopf. Quantum reflection of He₂ several nanometers above a grating surface. *Science*, 331:892–894, 2011.

Curriculum Vitae

Michele Sclafani

Personal information

Date of birth: 21 July 1982

Place of birth: Termini Imerese (Palermo)

Nationality: Italian

Education

Since 05/2009: PhD student in the group of Prof. Dr. M. Arndt at the University of Vienna, Faculty of Physics

09/2005-03/2009: Laurea specialistica: Università degli Studi di Palermo, Facoltà di Scienze MM.FF.NN., Corso di laurea in Fisica

09/2011-07/2005: Laurea triennale : Università degli Studi di Palermo, Facoltà di Scienze MM.FF.NN., Corso di laurea in Fisica

09/1996-06/2001: Maturità scientifica: Liceo Scientifico Statale "S. Cannizzaro" - Palermo, Italy

List of publications

1. M. Sclafani, T. Juffmann, C. Knobloch and M. Arndt, Quantum coherent propagation of complex molecules through the frustule of

the alga *Amphipleura pellucida*, *New. J. Phys.* (2013) - accepted for publication

2. M. Sclafani, M. Marksteiner, F. McLennar Keir, A. Divochiy, A. Korneev, A. Semenov, G. Goltsman and M. Arndt, Sensitivity of a superconducting nanowire detector for single ions at low energy. *Nanotechnology*, 23 (2012)
3. M. Marksteiner, A. Divochiy, M. Sclafani, P. Haslinger, H. Ulbricht, A. Korneev, A. Semenov, G. Goltsman and M. Arndt, A superconducting NbN detector for neutral nanoparticles, *Nanotechnology* 20 (2009)
4. M. Marksteiner, P. Haslinger, M. Sclafani, H. Ulbricht and M. Arndt, UV and VUV ionization of organic molecules, clusters and complexes, *J. Phys. Chem. A* 113 (2009)
5. M. Marksteiner, P. Haslinger, H. Ulbricht, M. Sclafani, H. Oberhofer, C. Dellago and M. Arndt, Gas-phase formation of large neutral alkaline-earth metal tryptophan complexes, *J. Am. Soc. Mass Spectrom.* 19 (2008)
6. G. Schiro', M. Sclafani, F. Natali, A. Cupane, Hydration dependent dynamics in sol-gel encapsulated myoglobin, *Eur. Biophys. J.* (2008)
7. G. Schiro', M. Sclafani, C. Caronna, F. Natali, M. Plazanet, A. Cupane, Dynamics of myoglobin in confinement: an elastic and quasi-elastic neutron scattering study, *Chem. Phys.* 345 (2008)